

OPTICAL, COMPOSITIONAL, AND STRUCTURAL IDENTIFICATION  
AND CHARACTERIZATION OF FIBROUS ZEOLITES

A Dissertation

Presented in Partial Fulfillment of the Requirements for the  
Degree of Doctorate of Philosophy

with a

Major in Geology

in the

College of Graduate Studies

University of Idaho

by

Kristina P. Pourtabib

Major Professor: Mickey E. Gunter, Ph.D.

Committee Members: Tom Williams, Ph.D.; Owen Neill, Ph.D.; Philip Neuhoff, Ph.D.

Department Administrator: Leslie Baker, Ph.D.

May 2017

### Authorization to Submit Dissertation

This dissertation of Kristina P. Pourtabib, submitted for the degree of Doctor of Philosophy with a Major in Geology and titled “Optical, Compositional, and Structural Identification and Characterization of Fibrous Zeolites,” has been reviewed in final form. Permission, as indicated by the signatures and dates below, is now granted to submit final copies to the College of Graduate Studies for approval.

Major Professor: \_\_\_\_\_ Date: \_\_\_\_\_  
Mickey E. Gunter, Ph.D.

Committee Members: \_\_\_\_\_ Date: \_\_\_\_\_  
Tom Williams, Ph.D.

\_\_\_\_\_ Date: \_\_\_\_\_  
Owen Neill, Ph.D.

\_\_\_\_\_ Date: \_\_\_\_\_  
Philip Neuhoff, Ph.D.

Department  
Administrator: \_\_\_\_\_ Date: \_\_\_\_\_  
Leslie Baker, Ph.D.

## Abstract

Zeolites are a group of aluminosilicate minerals containing various channel and cage structures that allow for the exchange of cations and H<sub>2</sub>O. Many of fibrous and/or acicular zeolite samples share similar hand sample characteristics making identification by more detailed means essential. Most of the zeolite minerals can be distinguished based on differences in composition, structure and optics. The two zeolite minerals erionite and offretite contain many overlapping properties that make differentiation problematic at times. Erionite is listed as a Group I carcinogen meaning that it is known to cause cancer in humans and animals alike, although the mechanisms by which erionite induces cancer are still unclear. Conversely, offretite does not possess these carcinogenetic properties. Being able to accurately distinguish erionite from other zeolite species will allow for analytical testing laboratories to develop more accurate means of recognizing erionite in an unknown sample.

The zeolites in this study were analyzed using Electron Probe Microanalysis (EPMA) for composition, Selected Area Electron Diffraction on the Transmission Electron Microscope (SAED, TEM) and Single Crystal X-Ray Diffraction (SCXRD) for structure, and the Spindle Stage for optics. Erionite and offretite both are hexagonal minerals with differing unit cell sizes and space groups. The unique space group symmetry of erionite, *P6<sub>3</sub>/mmc*, causes diffraction constraints (i.e. systematic absences) when using SAED on the TEM, while the diffraction pattern of offretite does not show diffraction constraints. Compositionally erionite is more Ca-rich than offretite, which is more Mg-rich, and optically, erionite and offretite have overlapping refractive indices.

Zeolite minerals are prone to dehydration due to the abundant H<sub>2</sub>O in their structure. Dehydration greatly affects the migration of extraframework cations into and out of certain cage and channel structures. Cation migration and the reorientation of H<sub>2</sub>O molecules can have large influences on the compositional, structural, and optical changes observed in these minerals. Prominent intergrowths, overgrowths, and stacking offsets in erionite and offretite, along with other zeolite minerals, will also directly reflect changes in mineral properties. This study aims to use multiple means of identification to differentiate the fibrous and acicular zeolite species, especially that of erionite and offretite.

## Acknowledgements

I would like to thank my dissertation committee members, Tom Williams, Owen Neill and Philip Neuhoff for agreeing to be a part of this experience with me. You have all provided much guidance and help with both analytical analysis and fieldwork. To Tom Williams in particular, I would like to thank you for allowing me open access to using the TEM. You have introduced me to an analytical instrument, that although has been in and out of commission throughout my time as a graduate student, is nevertheless an instrument that I really enjoy using and want to continue to use in my career. I would also like to acknowledge my advisor Mickey E. Gunter who brought me on as his graduate student. When we first met, I had reached out to you as an enthusiastic undergraduate student from a small state school in central Illinois with an interest in optical mineralogy, and you immediately made me feel welcome. Although lawyer and department chair obligations took up much of your time, I am appreciative for all of the freedom and resources (mostly provided from the time you spent with the lawyers) you have allowed me to use for my research, as well as the opportunities for travel.

I am thankful for Alan Segrave at Bureau Veritas for allowing me to intern at his company during the summer of 2015. I had always wanted the chance to experience working in an analytical lab and he helped to make that happen. I am forever grateful for the hospitality provided by Alan and his wife, Jeannie during that time. Finally I would like to thank my fellow graduate student Cody Steven. Your enthusiasm for learning has made me want to be a better student, and you have been the biggest help to me in everything, from figuring out things like the best sample preparation methods, to explaining optical analyses. You've consistently been there to talk with me about any research confusion or new ideas that I have, and I am so appreciative.

## **Dedication**

I would like to dedicate this dissertation to all of the family and friends that have supported me in my decision to pursue graduate school. To my parents, I would like to thank you for supporting me in my decision to move all the way from Illinois to Idaho for school. I know it has been tough having both your daughters out of state but I've appreciated the weekly Skype sessions. I would also like to thank my grandparents for their unwavering support despite their own personal health battles, and the rest of my family. I would especially like to thank my boyfriend, Everett, for his constant support and willingness to let me explain my research to him for sometimes hours on end. Lastly I would like to dedicate this dissertation to Fritz who was always my constant source of joy.

## Table of Contents

|   |     |
|---|-----|
| Authorization to Submit .....   | ii  |
| Abstract .....  | iii |
| Acknowledgements .....  | iv  |
| Dedication .....  | v   |
| Table of Contents .....   | vi  |
| List of Figures .....   | ix  |
| List of Tables .....  | xv  |
| List of Abbreviations .....   | xvi |
| <br>  |     |
| CHAPTER 1: Analytical Approach for Identification of the Zeolite Erionite ..... | 1   |
| Abstract .....  | 1   |
| Introduction .....  | 2   |
| General Information .....   | 2   |
| Occurrences in Nature .....   | 3   |
| Classification Schemes .....  | 3   |
| Materials and Methods .....   | 4   |
| Transmission Electron Microscopy .....  | 5   |
| Polarized Light Microscopy .....  | 6   |
| Powder X-Ray Diffraction .....  | 8   |
| Results .....   | 8   |
| TEM Analysis Results .....  | 8   |
| Hand Calculations .....   | 9   |
| PLM Analysis Results .....  | 9   |
| Powder XRD Analysis Results .....   | 10  |
| Discussion .....  | 10  |
| Future Work .....   | 11  |
| Acknowledgements .....  | 11  |
| References Cited .....  | 12  |
| Tables and Figures .....  | 15  |

|  |    |
|--|----|
| CHAPTER 2: Optical Analysis of the Fibrous/Acicular Zeolites: A Spindle Stage Approach ...                   | 27 |
| .....  | 27 |
| Abstract .....   | 27 |
| Introduction .....   | 28 |
| Materials and Methods .....  | 31 |
| Instrumentation .....  | 31 |
| Sample Preparation .....   | 32 |
| Methods .....  | 32 |
| Results .....  | 36 |
| Sign of Elongation .....   | 37 |
| Refractive Index Values .....  | 37 |
| Birefringence and Retardation .....  | 38 |
| Discussion .....   | 38 |
| Future Work .....  | 39 |
| Acknowledgements .....   | 39 |
| References Cited .....   | 41 |
| Tables and Figures .....   | 44 |
| CHAPTER 3: Relationship between Chemistry, Structure and Optics of the Zeolites Erionite and Offretite ..... | 58 |
| Abstract .....   | 58 |
| Introduction .....   | 58 |
| Structure and Composition .....  | 59 |
| Erionite and Offretite Optics .....  | 60 |
| Intergrowths, Overgrowths, and Stacking Sequences .....  | 62 |
| Materials and Methods .....  | 63 |
| Instrumentation .....  | 64 |
| Sample Preparation .....   | 65 |
| Methods .....  | 66 |
| Results .....  | 67 |
| EMPA .....   | 68 |

|  |     |
|--|-----|
| Discussion .....                                     | 72  |
| Future Work .....                                    | 74  |
| Acknowledgements .....                               | 75  |
| References Cited .....                               | 76  |
| Tables and Figures .....                             | 79  |
| Appendix A: Refractive Index Literature Review ..... | 103 |
| Appendix B: Additional Zeolite EPMA Data .....       | 107 |
| Appendix C: Additional Zeolite PLM Images .....      | 116 |
| Appendix D: Letter of Permission for Chapter 1 ..... | 132 |



## List of Figures

|   |    |
|---|----|
| Figure 1.1: Diagram looking down the c axis of erionite. Si (dark blue), H <sub>2</sub> O (black), Ca (light blue), O (red), and K (purple), (Gualtieri et al, 1998) .....  | 16 |
| Figure 1.2: Stereoscope images (A), altered volcanic tuff from Killdeer, North Dakota containing erionite and other minerals (B), and offretite and chabazite in a basalt vesicle from Adamello, Italy .....  | 17 |
| Figure 1.3: PLM image of woolly erionite from Durkee, Oregon. (B) Refractive index values of epsilon and omega of erionite and offretite (Tschernich, 1992; Deer et al, 1967). Red dotted line indicates region of no refractive index overlap .....  | 18 |
| Figure 1.4: TEM results of [150] zone axis orientation of erionite from the Killdeer Mountains in North Dakota (A), simulated diffraction pattern from CrystalMaker (yellow), overlain on top of the real SAED diffraction pattern (black dots), note the systematic absences along c* (Gualtieri et al, 1998). (B) EDS of erionite particle showing major cation content along with (C), TEM image of oriented erionite grain, and (D) CrystalMaker oriented structure diagram of erionite ..... | 19 |
| Figure 1.5: TEM results of [140] zone axis orientation of offretite from Adamello, Italy (A), simulated diffraction pattern from CrystalMaker (yellow), overlain on top of the real SAED diffraction pattern (black dots) (Gualtieri et al, 1998). (B) EDS of offretite particle showing major cation content along with (C), TEM image of oriented offretite grain, and (D) CrystalMaker oriented structure diagram of offretite .....   | 20 |
| Figure 1.6: TEM results of [110] zone axis orientation of mordenite from Challis, Idaho (A), simulated diffraction pattern from CrystalMaker (yellow), overlain on top of the real SAED diffraction pattern (black dots) (Simoncic and Armbruster, 2004). (B) EDS of mordenite particle showing major cation content along with (C), TEM image of oriented mordenite grain, and (D) CrystalMaker oriented structure diagram of mordenite .....  | 21 |
| Figure 1.7: TEM results of [100] zone axis orientation of scolecite from Poona, India (A), simulated diffraction pattern from CrystalMaker (yellow), overlain on top of the real SAED diffraction pattern (black dots) (Kuntzinger et al, 1998). (B) EDS of scolecite particle showing major cation content along with (C), TEM image of oriented scolecite grain, and (D) CrystalMaker oriented structure diagram of scolecite .....   | 22 |

|  |    |
|--|----|
| Figure 1.8: Zone axis hand calculations (A), thallium chloride standard at 40cm, and (B) locations of measurements taken from Killdeer Mountain, North Dakota erionite sample .....  | 23 |
| Figure 1.9: PLM images of sign of elongation test (A), Killdeer Mountain erionite in 1.484 liquid showing addition (B), Poona, India scolecite in 1.510 liquid showing subtraction (C) Adamello, Italy offretite in 1.484 liquid showing subtraction, and (C), Challis, Idaho mordenite in 1.474 liquid showing subtraction upon insertion of the wave plate ..... | 24 |
| Figure 1.10: Powder XRD 3 hour scan 2-52 $\theta$ of Rome, Oregon altered volcanic tuff containing erionite, and inset picture showing hand sample with pocket knife for scale .....   | 25 |
| Figure 1.11: Modified diagram showing isolated erionite (open squares) and offretite (solid diamonds) in relation to divalent vs. monovalent cation content and Gladstone Dale values calculated using major elemental data provided by Passaglia et al. (1998) .....  | 26 |
| Figure 2.1: Refractive index values found in literature for erionite and offretite. Illustrating a lack of refractive index overlap around 1.485 – 1.486 for $\epsilon$ in erionite and $\epsilon$ in offretite (Tschernich, 1992; Gottardi and Galli, 1985; Deer et al, 1967) .....   | 45 |
| Figure 2.2: Google Map of zeolite sample locations used in this study .....  | 46 |
| Figure 2.3: Stereoscopic images of elongate zeolite samples (A) erionite sample 1 (Pima Co., AZ, USA), and (B) offretite and erionite sample 28 (Rock Island Dam, Douglas Co, WA, USA) .....   | 47 |
| Figure 2.4: (A) Leitz microscope, fitted with a Supper spindle stage, spindle stage goniometer, Vickers A.E.I. Image Splitting Eyepiece (not shown in this image), camera, and monochromator and (B) Abbe Refractometer used in this study .....   | 48 |
| Figure 2.5: 10x magnification of erionite sample number 1 (Pima Co., AZ, USA), (A) Plane Polarized Light (PPL) image, (B) Cross Polarized Light (XPL) image, C) XPL image with 530 nm accessory plate inserted. Note: tip of grain and base of grain show different changes in retardation .....   | 49 |
| Figure 2.6: 10x magnification of erionite sample number 1 using the Sénarmont Compensator. (A) PPL image of sample with monochromator inserted to about 540 nm (green). (B) Same PPL image of sample with analyzer rotated to reverse the colors .....   | 50 |
| Figure 2.7: Sign of elongation of erionite, offretite, erionite/offretite intergrowth, and offretite intergrowth samples. For this study the zeolite species determination comes directly from the labeled sample names .....  | 51 |

|   |    |
|---|----|
| Figure 2.8: Chart displaying refractive index values for each fibrous/acicular zeolite from this study, using a combination of measured values via spindle stage analysis, and calculated values from precise oil calibrations using the Abbe Refractometer both fast and slow refractive index values were determined .....  | 52 |
| Figure 2.9: Measured and calculated refractive index values for erionite, offretite, erionite/offretite intergrowths, offretite intergrowths (or overgrowths), and mordenite .....  | 53 |
| Figure 2.10: (A) Measured and calculated refractive index values for mazzite, mesolite and natrolite, and measured and (B) calculated refractive index values for okenite and scolecite ....  | 54 |
| Figure 2.11: Measured and calculated refractive index values for tetranatrolite, tetranatrolite/paranatrolite and thomsonite .....  | 55 |
| Figure 2.12: Chart displaying birefringence ( $\delta$ ) and retardation ( $\Delta$ ) for each zeolite sample. Birefringence was calculated using the Sénarmont Compensator and Vickers Image Splitting Eyepiece, while retardation was calculated using the Abbe Refractometer and the Sénarmont Compensator .....   | 56 |
| Figure 2.13: Sample 1, erionite-Ca, Phelps Dodge Co., Well no. 1, Little Ajo Mountains, Ajo District, Pima Co., AZ, USA. Sample shows a distinctive difference in sign of elongation on the tip of the grain (A) image in XPL with accessory plate inserted, (B) image in XPL .....   | 57 |
| Figure 3.1: Indexed diffraction patterns of (A) erionite 170 zone axis and (C) offretite 150 zone axis from sample location #1, Phelps Dodge Co. Well No. 1, Little Ajo Mtns, Ajo District, Pima County, AZ, USA. Yellow dots indicate the simulated pattern while black dots indicate the actual diffraction pattern. Images (B) and (D) show the original diffraction pattern. Simulated diffraction pattern (yellow dots) data from Gualtieri et al., 1998.....  | 84 |
| Figure 3.2: (A) shows a backscattered electron (BSE) images of a sample of erionite from Phelps Dodge Co. Well No. 1, Little Ajo Mtns, Ajo District, Pima County, AZ, USA. A1 and B1 show PLM images, A2 and B2 are XPL images where extinction on the grain tip is visible. A3 and B3 are XPL images with the $\lambda$ accessory plate inserted clearly showing different signs of elongation on each grain. (B) BSE image of erionite sample from Phelps Dodge Co. Well No. 1, Little Ajo Mtns, Ajo District, Pima County, AZ, USA along with associated APFU data ..... | 85 |

- Figure 3.3: (A) shows a backscattered electron (BSE) images of a sample of erionite from Phelps Dodge Co. Well No. 1, Little Ajo Mtns, Ajo District, Pima County, AZ, USA. A1 and B1 show PLM images, A2 and B2 are XPL images where extinction on the grain tip is visible. A3 and B3 are XPL images with the  $\lambda$  accessory plate inserted clearly showing different signs of elongation on each grain. (B) BSE image of erionite sample from Phelps Dodge Co. Well No. 1, Little Ajo Mtns, Ajo District, Pima County, AZ, USA along with associated APFU data .....86
- Figure 3.4: Ternary diagram of individual APFU and sign of elongation points from erionite sample 45\_extra .....87
- Figure 3.5: (A) scatter diagram of erionite sample number 45\_extra with Mg vs. Ca along with sign of elongation and R-value. Graphs show line of best fit along with confidence intervals in the shaded regions. (B) XPL image with accessory plate inserted of sample 45\_extra.....88
- Figure 3.6: (A) shows a backscattered electron (BSE) images of a sample of erionite from Clifton, Greenlee Co, AZ, USA. A1 and B1 show PLM images, A2 and B2 are XPL images where extinction on the grain tip is visible. A3 and B3 are XPL images with the  $\lambda$  accessory plate inserted clearly showing different signs of elongation on each grain. (B) BSE image of erionite sample along with associated APFU data.....89
- Figure 3.7: (A) shows a backscattered electron (BSE) images of a sample of erionite from Herbstein, Vogelsberg, Hesse, Germany. A1 and B1 show PLM images, A2 and B2 are XPL images where extinction on the grain tip is visible. A3 and B3 are XPL images with the  $\lambda$  accessory plate inserted clearly showing different signs of elongation on each grain. (B) BSE image of erionite sample along with associated APFU data.....90
- Figure 3.8: (A) shows a backscattered electron (BSE) images of a sample of erionite from Eureka Valley, Del Norte Co, California, USA. A1 and B1 show PLM images, A2 and B2 are XPL images where extinction on the grain tip is visible. A3 and B3 are XPL images with the  $\lambda$  accessory plate inserted clearly showing different signs of elongation on each grain. (B) BSE image of erionite sample along with associated APFU data .....91
- Figure 3.9: (A) shows a backscattered electron (BSE) images of a sample of offretite from Mt. Simiose Semiol, Chatelneuf, Loire, Rhone Alpes, France. A1 and B1 show PLM images, A2 and B2 are XPL images where extinction on the grain tip is visible. A3 and B3 are XPL

images with the  $\lambda$  accessory plate inserted clearly showing different signs of elongation on each grain. (B) BSE image of offretite sample along with associated APFU data.....92

Figure 3.10: (A) shows a backscattered electron (BSE) images of a sample of offretite from Adamella, Italy. A1 and B1 show PLM images, A2 and B2 are XPL images where extinction on the grain tip is visible. A3 and B3 are XPL images with the  $\lambda$  accessory plate inserted clearly showing different signs of elongation on each grain. (B) BSE image of offretite sample along with associated EPMA APFU data .....93

Figure 3.11: (A) shows a backscattered electron (BSE) images of a sample of offretite from Mount Semiol, Chatelneuf, Loire, Rhone Alpes, France. A1 and B1 show PLM images, A2 and B2 are XPL images where extinction on the grain tip is visible. A3 and B3 are XPL images with the  $\lambda$  accessory plate inserted clearly showing different signs of elongation on each grain. (B) BSE image of offretite sample along with associated APFU data.....94

Figure 3.12: Erionite correlation coefficients between APFU. Yellow boxes = strong correlation while orange boxes = moderate correlations between variables.....95

Figure 3.13: Offretite correlation coefficients between APFU. Yellow boxes = strong correlation while orange boxes = moderate correlations between variables.....96

Figure 3.14: Ternary diagram of erionite (circles), offretite (arrow), and erionite/offretite (star) APFU, and sign of elongation. Yellow circle indicates mislabeled erionite samples (actually offretite) 9, 13a, 14, and 14b. Orange circle indicates mislabeled offretite (actually erionite) samples 29 and 29a.....97

Figure 3.15: Scatter diagram of erionite (circle), offretite (arrow), and erionite/offretite (star) samples used in this study of R-value vs. Mg/Ca. Values based off of APFU calculations. Blue line marks the division between the majority of the erionite and offretite samples with respect to the R-value. Samples in the orange circle are mislabeled offretite samples (actually erionite) 29a. Yellow circle indicates offretite overgrown on levyne 5a. Purple circles are mislabeled erionite samples (actually offretite) 9, 13a and 14b.....98

Figure 3.16: Scatter diagram of erionite (circle), offretite (arrow), and erionite/offretite (star) samples used in this study of R-value vs. K. Values based off of APFU calculations. Blue line marks the division between the majority of the erionite and offretite samples with respect to the R-value. Sample in the orange circles are mislabeled offretite samples (actually erionite)

- 29a. Yellow circle is offretite overgrown on levyne (5a). Purple circles are mislabeled erionites (actually offretites) 9, 13a, and 14b.....99
- Figure 3.17: Scatter diagram of (A) erionite and (B) offretite samples used in this study showing fast (+) and slow (circle) rays vs. R-value. R-value in AFPU. Shaded regions show confidence intervals .....100
- Figure 3.18: Scatter diagram of erionite (circle), offretite (arrow), erionite/offretite (star) samples used in this study of (A) length fast (red) and length slow (blue) vs. R-value and (B) length fast (red) and length slow (blue) vs. Mg/Ca. R-value in APFU. Lines of best fit along with confidence intervals (shaded region) can be seen. Outliers (orange circles).....101
- Figure 3.19: (A) scatter diagram of erionite samples used in this study showing Mg vs Ca. Shaded regions show confidence intervals. (B) scatter diagram of offretite samples used in this study showing Mg vs Ca. Shaded regions show confidence intervals (orange) points and length slow (blue) points. Erionite (circles), offretite (arrow), erionite/offretite (star) .....102

## List of Tables

|   |    |
|---|----|
| Table 1.1: Zeolite samples and locations used in this study, noting the geologic environment ..   | 15 |
| Table 2.1: Primary zeolites found in each sample used in this study .....   | 44 |
| Table 3.1: Sample numbers and locations of erionites and offretites used in this study .....  | 79 |
| Table 3.2: EPMA parameters used in this study .....   | 80 |
| Table 3.3: Final mineral identification chart using initial sample names, TEM, and SCXRD results .....  | 81 |
| Table 3.4: Erionite samples used in this study showing average chemistry per grain. H <sub>2</sub> O* was calculated by difference with EPMA. E% = Balance Error Calculation, R-value = Si/(Si+Al) (Passaglia, 1970; Passaglia et al, 1998. L.S. = length slow, L.F. = length fast. Values in red indicate Mg contents > 0.80 (Gualtieri et al, 1998; Dogan and Dogan, 2008, Dogan, 2011) ..... | 82 |
| Table 3.5: Offretite samples used in this study showing average chemistry per grain. H <sub>2</sub> O* was calculated by difference with EPMA. E% = Balance Error Calculation, R-value = Si/(Si+Al) (Passaglia, 1970; Passaglia et al, 1998. L.S. = length slow, L.F. = length fast .....   | 83 |

## List of Abbreviations

|  |    |
|--|----|
| 1. SAED: Selected Area Electron Diffraction .....          | 1  |
| 2. TEM: Transmission Electron Microscope .....             | 1  |
| 3. PLM: Polarized Light Microscope .....                   | 1  |
| 4. XRD: Powder X-Ray Diffraction .....                     | 1  |
| 5. EDS: Energy Dispersive Spectroscopy .....               | 2  |
| 6. IARC: International Agency for Research on Cancer ..... | 2  |
| 7. EPA: Environmental Protection Agency .....              | 2  |
| 8. SBU: Structural Building Unit .....                     | 3  |
| 9. R.I.: Refractive Index .....                            | 27 |
| 10. EPMA: Electron Probe Microanalysis .....               | 27 |
| 11. SCXRD: Single Crystal X-Ray Diffraction .....          | 28 |
| 12. PPL: Plane Polarized Light .....                       | 32 |
| 13. XPL: Crossed Polarized Light .....                     | 33 |
| 14. WDS: Wavelength Dispersive Spectroscopy .....          | 39 |



## Chapter 1:

### Analytical Approach for Identification of the Zeolite Erionite

Pourtabib, K. P. and Gunter, M.E. (2015) Analytical approach for identification of the zeolite erionite, *The Microscope*, vol. 63:4, 161-171.

#### ABSTRACT

The need for precise identification of the fibrous/acicular zeolite mineral erionite has become increasingly important due to erionite's ties to mesothelioma in Turkey and the western North America. The regulatory community struggles to unambiguously identify asbestiform minerals when they occur in natural rather than built environments. Zeolites present an even more unique set of problems due to the similar cation content and crystal structure observed between different zeolite species, such as erionite and offretite. Currently, there is a lack of regulatory methods for accurately identifying erionite particles in nature. We test a variety of techniques that can be applied for the identification of erionite, including the use of selected area electron diffraction (SAED) on a transmission electron microscope (TEM), indirect zeolite identification through a polarized light microscope (PLM), and powder x-ray diffraction (XRD) for analysis of bulk composition. We found that smaller TEM-scale data provides paramount structural information in the form of diffraction patterns because erionite shows systematic absences (i.e., diffraction constraints) along  $uv0$  of  $00l = 2n$  due to its space group symmetry, while the other zeolites in this study will show different diffraction constraints along  $c^*$ , and different repeats in  $c$ . We have shown that by using a combination of scale dependent identification methods such as TEM, PLM, and XRD these zeolites can be accurately distinguished from one another given sufficient care.

Keywords: Zeolites, erionite, offretite, transmission electron microscopy, selected area electron diffraction, energy dispersive X-ray spectroscopy, polarized light microscopy

## INTRODUCTION

Certain minerals with fibrous and/or elongate morphologies have been shown to have significant carcinogenic potential. Although the mechanisms by which these particles cause cancer are still poorly understood (i.e., surface area, surface chemistry etc.), it is critical that these particles are identified correctly. Litigation associated with negative health effects related to mineral exposure has largely focused on the five regulated amphiboles and one regulated serpentine group mineral. However, the zeolite group mineral erionite also has carcinogenic potential (Lefond, 1983). Previously, erionite was mined for use in industry due to its cation-exchange capacity (Pabalan and Bertetti, 2001). Mining of erionite largely ceased after the World Health Organization and the International Agency for Research on Cancer identified it as a Group I carcinogen, causing both pleural and peritoneal mesothelioma to humans and animals (IARC, 1987a-b). Other common zeolites such as chabazite, phillipsite and clinoptilolite are still used in industry (Kalló, 2001), and it is important that analytical laboratories are able to identify the presence of even trace amounts of erionite for quality assurance purposes. Currently, methods such as central stop dispersion staining using the PLM or cation content ratios using EDS on the TEM are used in analytical laboratories for erionite identification, but these methods will not work (ASTM, 2012). Although the Environmental Protection Agency (EPA) does not regulate erionite people are still facing exposure to this mineral due to its natural geologic occurrences both in the United States and abroad (Dogan et al, 2008).

### *General Information*

Erionite ( $K_2(Na,Ca_{0.5})_8[Al_{10}Si_{26}O_{72}] \cdot 28H_2O$ ) is an aluminosilicate mineral whose structure is comprised of various channels and cages which house both extraframework cations and  $H_2O$ . The two main cage structures in erionite include (1) a six-membered double ring that is usually empty, (2) the cancrinite cage, that mainly houses K, and (3) the erionite cage, that contains various amounts of Ca, Na, and Mg (Armbruster and Gunter, 2001). This mineral belongs to the hexagonal crystal system with crystallographic cell parameters approximately  $a = 13.26$  and  $c = 15.12 \text{ \AA}$ , and space group of  $P6_3/mmc$  (Figure 1.1). On the other hand, offretite ( $KCaMg[Al_5Si_{13}O_{36}] \cdot 15H_2O$ ) is also a hexagonal zeolite with

crystallographic cell parameters approximately  $a = 13.29$  and  $c = 7.58$  Å, and space group of  $P\bar{6}m2$ . The four main cage structures in offretite include (1) the six-membered double rings which are usually empty or have very low occupancy, (2) the cancrinite cage, that mainly houses K, (3) the gmelinite cage which holds Mg surrounded by disordered H<sub>2</sub>O, and (4) the wide channels which houses Ca-H<sub>2</sub>O complexes (Armbruster and Gunter, 2001). The main differences between erionite and offretite are crystal structure and Si/Al ratios. Based off of the chemical formula alone (i.e., cation content), erionite and offretite cannot be differentiated.

#### *Occurrences in Nature*

Erionite can be found throughout the western United States, as well as in similar geologic environments such as central Mexico and the Cappadocia region of Turkey (Dogan et al, 2008; Van Gosen et al., 2013). Generally erionite and other zeolites such as offretite form in either altered volcanic tuff or within the vesicles of basalts (Figure 1.2: Hay and Sheppard, 2001). In volcanic tuff, erionite occurs in combination with other minerals such as feldspars, clays, quartz, volcanic glass, and other zeolites. Normally the erionite is confined to certain geologic units, but fine-grained zeolite particles may also be disseminated throughout easily erodible formations. Erionite within volcanic tuffs is readily entrained into the atmosphere, thus providing the main source for exposure leading to a mesothelioma diagnosis (Bish and Chipera, 1991). In addition, alkaline-rich hydrothermal waters precipitate zeolites in the vesicles of basalts. Erionite in basalt vesicles can form well-developed crystals, but is usually found in small quantities and is difficult to access as it is encased in basalt.

#### *Classification Schemes*

The three main classification schemes applied to distinguish between the various zeolite species include (1) framework topologies (Meier et al, 1996), (2) structural building units (SBU) (Breck, 1974), and (3) a combination of SBUs and historical context (Gottardi and Galli, 1985). There are currently over 40 different framework topologies used to classify zeolites, which also considers the framework density (number of T-atoms per 1,000 Å<sup>3</sup>) of the individual zeolite. Framework topologies differentiate zeolites using three letter structural

codes (e.g., NAT). The zeolite that was discovered first receives priority in naming. For example, in the NAT group, which includes natrolite, mesolite, scolecite, gonnardite, and paranatrolite, natrolite was historically the first mineral discovered and thus has the NAT group named after it. Erionite's framework topology is ERI and is currently the only zeolite in this group. The second main classification scheme, SBU, is based on the linkages of tetrahedra. There are seven main SBU groups. For example, Group 5 ( $T_5O_{10}$ ) includes zeolites such as natrolite, mesolite, and scolecite. In this group the predominant crystallographic components are linked chains of five tetrahedra parallel to the c-axis, which causes minerals in this group to be elongated parallel to this axis. Erionite falls into SBU Group 2 or the S6R (single six-ring) group, which also contains offretite. The final classification scheme used is a combination of framework topologies and historical context. This classification scheme simply takes information from the SBU and attaches a group descriptive modifier to it. For example, erionite is in the 6-ring group as it combines the single and double six-membered ring zeolites. Some confusion in zeolite nomenclature arises in the fibrous zeolite subgroups, which are Group 5 ( $T_5O_{10}$ ) zeolites. Although zeolites in this subgroup have elongate morphologies, zeolites outside of this group may also exhibit this same morphology. For example, erionite can occur in both a fibrous and elongate morphology yet does not fall into the fibrous zeolite subgroup.

Zeolites can be difficult to differentiate using hand sample identification alone. Unless a well-defined crystal form can be observed, most zeolites share a similar vitreous, clear to white appearance. Identification of different zeolites requires an understanding of crystal chemistry, crystal structure, and optical properties. Many of the techniques for identification utilize instrumentation that can be found in most analytical laboratory setting, such as SAED on the TEM, PLM, and XRD. These methods are discussed below.

## **MATERIALS AND METHODS**

Zeolite samples used in this study all exhibit elongate particle morphologies. Samples were collected from basalt vesicles and altered volcanic tuff (Table 1.1).

## Transmission Electron Microscopy

### *Instrumentation*

TEM analyses on the zeolite samples were carried out at the University of Idaho on a JEOL JEM 2010 using a double tilt sample holder, and energy dispersive spectroscopy (EDS) was performed using a Thermo Scientific detector coupled with NSS software. Samples were run at an accelerating voltage of 200 KeV, and a thallium chloride diffraction standard was used.

### *Sample Preparation*

Sample preparation techniques follow the Jaffe-Wick method (Yamate et al, 1984). Samples were crushed with an agate mortar and pestle, diluted to 50 ml in isopropanol alcohol, and sonicated. Crushed aliquots were run through a simple vacuum filtration set up and particles were deposited onto 0.2- $\mu\text{m}$  polychloroethylene (PCE) filter paper. Dried sample-coated PCE filter paper was then carbon coated, cut, and transferred to blank 200-mesh copper TEM grids using chloroform. Samples were kept in a glass-covered dish for at most 24 hours, or until the PCE filter paper had dissolved. If this modified version of the Jaffe-Wick method was unsuccessful, crushed samples were placed in isopropanol alcohol, sonicated, and pipetted directly onto a carbon-coated TEM grid for analysis.

### *Methods*

Both SAED on the TEM and indexing the diffraction patterns using CrystalMaker software were used to characterize the structure of the zeolites. Erionite can be differentiated from offretite based upon SAED as seen by looking at the space group symmetry of  $P6_3/mmc$ . The  $6_3$  designation in the space group indicates that erionite's arrangement of atoms in the unit cell contains a symmetry operation called a screw axis. This screw axis is defined as being a  $180^\circ$  rotation followed by a  $\frac{1}{2}$  translation along the c-axis in the unit cell. This creates a plane of atoms in the unit cell and results in systematic absences (i.e., diffraction constraints) at  $00l = 2n$  along  $c^*$ . Since the erionite samples used in this study had elongate morphologies, and the c-crystallographic axis in erionite is parallel to the long direction, the minerals predominantly had the c-axis within, or close to, the plane of the stage. Zone axis

patterns could be obtained by adjusting the double-tilt sample holder. SAED patterns of erionite, along with many of the other zeolites, must be imaged quickly due to the abundance of H<sub>2</sub>O in the structure causing the diffraction pattern to disintegrate quickly under the intense electron beam. Consequently, the diffraction pattern should be analyzed first, followed by EDS and then a final particle image.

All of the zeolites analyzed in this study by TEM yielded diffraction patterns, images, and EDS with each sample. The known sample location and rough EDS served as the primary identification technique for these zeolites. Further identification by indexing the diffraction patterns was obtained using the CrystalMaker and SingleCrystal software (Palmer, 2015). This software allows users to download already determined crystal structure files from the American Mineralogist Crystal Structure Database (or create their own crystal structure data) into CrystalMaker and simulate a diffraction pattern in a certain orientation through SingleCrystal. Finally, the user is able to upload their own diffraction data into SingleCrystal and manipulate the software until a simulated and real diffraction pattern is matched. By using the SingleCrystal software for diffraction pattern indexing, it is easier to notice the systematic absences in erionite compared with the other zeolites from this study. Although there can be some discrepancies between the downloaded data and the user's data, it is important to note that the samples used may have slightly different unit cell dimensions and composition resulting in non-perfect matches when using the software along with real diffraction data.

## **Polarized Light Microscopy**

### *Instrumentation*

PLM analyses on the zeolite samples were performed on an Olympus BH-2 microscope and images were taken on an Olympus DP-70. Any PLM would be acceptable for use in this portion of the analysis, and the objectives used can vary depending on the resolution of your microscope.

### *Sample Preparation*

A refractive index liquid of 1.484 was used in order to distinguish between erionite and offretite due to having no overlap in refractive index values at this boundary, although future optical work might better define this boundary (Tschernich, 1992; Deer et al, 1967). For sample preparation a simple immersion method was used which included crushing samples with a mortar and pestle and then dropping sample directly onto a glass microscope slide with refractive index liquid and a cover slip for analysis.

### *Methods*

Particle morphologies, Becke line analyses, and the sign of elongation were used for indirect identification of erionite (Figure 1.3 A). Samples were placed in 1.484 refractive index liquid for grain mount analysis. Previous studies show that this refractive index liquid value defines the boundary between epsilon in erionite and epsilon in offretite (Figure 1.3 B). Based on this boundary between these two zeolites, the Becke line was additionally used to differentiate between erionite and offretite. However, erionite and offretite occasionally occur as overgrowths of one another, so results from Becke line analyses were at times ambiguous (Wise and Tschernich, 1976). Lastly, the sign of elongation was used in order to differentiate erionite from other elongate zeolites such as offretite, mordenite, and scolecite. The sign of elongation Test uses an elongate grain and determines whether the large or small refractive index is parallel to the long axis of the crystal. This is accomplished by having the crystal parallel to the slow direction of the accessory plate (Bloss, 1999). During this test the long axis of the grain is rotated clockwise 45 degrees from the polarizers, the polarizers are crossed, and the accessory plate is inserted. If there is an increase in retardation then the mineral is length slow (not related to optic sign), and the highest refractive index value is parallel to the long direction of the mineral. Conversely, if there is a decrease in retardation then the mineral is length fast, and the smallest refractive index value is parallel to the long direction of the mineral.

## **Powder X-Ray Diffraction**

### *Instrumentation*

Analyses were performed on a Bruker Diffractometer D5000 using the software XRD Commander and Eva. Individual scans were run from 2-52° $\theta$  for a period of about three hours in order to obtain better sensitivity on the main peaks in the scan.

### *Sample Preparation*

Altered volcanic tuff samples were initially crushed with an agate or ceramic mortar and pestle, and then further crushed using a McCrone Micronizing Mill. Crushed samples were then prepared for analyses' using a back filled powder mount to assist in creating reproducible scans. For vesicle samples, low quantities of zeolite prevented the use of the back filled powder mount method. Instead, samples were plucked from the basalt host and crushed with a mortar and pestle. Samples were then suspended in acetone and poured over a quartz zero background plate.

### *Methods*

The software Eva was used to identify the crystalline phases within the samples. Rietveld Refinements and further crystallographic refinements were not used, as the main purpose was mineral identification.

## **RESULTS**

### *TEM Analysis Results*

TEM analysis of the various elongate zeolites used in this study further confirmed that erionite shows systematic absences (i.e., diffraction constraints) of  $00l = 2n$  along  $uv0$  due to its space group symmetry while the other zeolites along a similar orientation will show no diffraction constraints (Figures 1.4-1.7). TEM results also proved that relying on cation content obtained by EDS for sole identification is inaccurate due to differences in count times, dead time, and overall composition of a unique zeolite sample, the EDS spectra used in these images were chosen to be representative of the unique zeolite formulas from this study,



although these are best grain case scenarios. The identification of these zeolites is mostly dependent on structure; due to similarities in cation content looking at compositional differences by EDS alone is not enough to distinguish between zeolite species.

### *Hand Calculations*

Since many analytical testing laboratories rely on the use of hand calculations to determine the zone axis of certain diffraction patterns, hand calculations were also performed on these zeolites. Using a thallium chloride standard, the zone axis was calculated for erionite, offretite, scolecite, and mordenite. The calculation for erionite will be discussed in detail. Using the 40 cm camera length used to obtain the diffraction pattern of erionite, the d-spacings of the standard, and the standard measurements, the camera constant was calculated to be roughly 72.998 mmÅ (Figure 1.8 A). Both  $d_1$  and  $d_2$  as well as the angle between the vectors was measured for the pattern of erionite, and using the Eva software hkl values were determined to be [200] and [512] (Figure 1.8 B). Further calculations showed the zone axes of the erionite pattern to be  $[0\bar{4}2]$  or  $[0\bar{2}1]$ , which differs from the [150] zone axis match found using SingleCrystal.

### *PLM Analysis Results*

Using the sign of elongation test to differentiate erionite from the other zeolites was often prohibited, as many samples did not contain particles large enough to produce noticeable coloration differences when the accessory plate was inserted because the sample yielded very low retardation. Zeolites in altered volcanic tuff samples were smaller than those in basalts [ $< 5$  nm]. Elongate zeolites were often splayed or bundled, producing anomalous interference colors that could not be quantified. On larger, well-defined, single crystals of erionite, the sign of elongation proved to be a useful technique for quick differentiation between the zeolites offretite, mordenite, and scolecite (Figure 1.9). Due to small particle sizes, the Becke line was only used when there were well-defined single zeolite particles.

### *Powder XRD Analysis Results*

The three-hour ( $2\text{-}52^\circ\theta$ ) powder XRD analysis of an altered volcanic tuff sample from Rome, Oregon, revealed abundant erionite with minor clay and/or feldspar mineral phases (Figure 1.10).

## **DISCUSSION**

Zeolite identification, especially that of erionite can be less than ideal due to small particle sizes and similar hand sample appearances, but by using scale-dependent identification techniques zeolite minerals can be distinguished from one another. SAED on the TEM utilizes a small-scale approach to identification, looking at the differences in unit cell (i.e., diffraction constraints) between erionite and other zeolite species. As shown in the results, erionite will have systematic absences along  $uv0$ , while the other zeolite species analyzed do not. However, when relying on the method used in analytical laboratories for zone axis hand calculations, these results are commonly inconsistent from what is actually being observed on an SAED pattern. For example, since erionite is hexagonal the last number when referring to the zone axis (i.e.,  $[uvw]$ ) corresponds to the  $c$ -crystallographic axis, and because the  $c$ -axis is lying within the plane of the microscope stage it should be zero or nearly zero. This just proves that with the integration of new tools such as SingleCrystal into an analytical laboratory setting, inconsistencies in the standard hand calculation practice become more prevalent, and TEM analysts must have a general understanding of when results make sense and when they do not. Identification using the PLM focuses on a larger scale, looking at the relationship between epsilon and omega in erionite versus other closely related zeolites such as offretite, and uses the sign of elongation test to show that erionite is the only zeolite used in this analysis to be length slow. Lastly, powder XRD is a good tool to use when trying to distinguish between the various zeolite species from a bulk sample since they each have unique structural fingerprints, although some analytical laboratories do not have access to a powder XRD. However, with the use of powder XRD, the patterns for both erionite and offretite overlap, so a match for erionite may also contain offretite, but a match for pure offretite will not have any erionite due to certain reflections being absent (Passaglia et al, 1998). We advise the use of all three methods for erionite identification.

Ultimately, the best method of identification is the use of SAED on the TEM along with the CrystalMaker software for mineral diffraction indexing. PLM and powder XRD are very useful, but most altered volcanic tuff of erionite is too small to get good resolution in the PLM and powder XRD will have a difficult time detecting small quantities of sample if the scan is too short.

## **FUTURE WORK**

Future studies of erionite and other closely related elongate zeolites would benefit from more precise optical characterizations, and better constraints on the changes in refractive index due to differences in cation content between erionite and closely related zeolites such as offretite. By using previously published compositional data on erionite and offretite by electron microprobe analysis, Gladstone-Dale values (i.e., average refractive index) could be determined and potentially related to changes in composition, as certain samples of erionite have shown to be either optically positive or negative (Passaglia et al, 1998). Calculated Gladstone-Dale constants thus far have shown no trend in relating the composition of erionite and offretite to refractive index value (Figure 1.11).

## **ACKNOWLEDGEMENTS**

I would like to thank the Natural History Museum of Los Angeles County for providing many outstanding zeolite samples, Bernie Saini-Eidukat for providing the North Dakota zeolites samples, and Tom Williams for his help and allowing us to use the University of Idaho's analytical laboratory facility.

**REFERENCES CITED**

- Armbruster, T., and Gunter, M. E. (2001) Crystal structures of natural zeolites, *Reviews in Mineralogy and Geochemistry*, 45, 1-67.
- ASTM Standard WK39550 (2012) New test methods for polarized light microscopy analysis of erionite in soils and gravels, ASTM International, West Conshohocken, PA, <http://www.astm.org/DATABASE.CART/WORKITEMS/WK39550.htm>
- Ballirano, P., Pacella, E., Creminsini, C., Nardi, E., Fantauzzi, M., Atzei, D., Rossi, A., and Cametti, G. (2015) Fe (II) segregation at a specific crystallographic site of fibrous erionite: a first step toward the understanding of the mechanisms inducing its arcinogenicity, *Microporous and Mesoporous Materials*, 211, 49-63.
- Baris, Y.I., Artvinli, M., and Sahin, A.A. (1979) Environmental mesothelioma in Turkey, *Annals of the New York Academy of Sciences*, 330:1, 423-432.
- Bish, D. L., and Chipera, S. J. (1991) Detection of trace amounts of erionite using x-ray powder diffraction: erionite in tuffs of Yucca Mountain, Nevada, and Central Turkey, *Clays and Clay Minerals*, 39:4, 437-445.
- Bloss, F. D., Gunter, M. E., Su, S., and Wolfe, H. E. (1983) Gladstone-Dale constants: a new approach, *The Canadian Mineralogist*, 21:1, 93-99.
- Bloss, F. D. (1999) *Optical Crystallography*, Mineralogical Society of America, 5, 120-121 pp.
- Breck, D.W. (1974) *Zeolite Molecular Sieves, Structure, Chemistry, and Use*, John Wiley and Sons, New York, 771 pp.
- Dyar, M. D., and Gunter, M.E. (2008) *Mineralogy and Optical Mineralogy*, Mineralogical Society of America, Chantilly, V.A., 708 pp.
- Deer, W.A., Howie, R.A., and Zussman J. (2013) *Rock Forming Minerals: Volume Four: Framework Silicates*, Longmans, 355-362 pp.
- Dogan, U.A., Dogan, M., and Hoskins, J. A. (2008) Erionite series minerals: Mineralogical and carcinogenic properties, *Environmental Geochemistry and Health*, 30, 367-381.
- Eyde, T.H., and Holmes, D.A. (2006) Zeolites. In *Industrial Minerals and Rocks*, eds., Kogel, J.E., Trivedi, N.C., Barker, J.M., and Krukowski, S.T. Society for Mining, Metallurgy, and Exploration, Inc., Littleton, Colorado, 971-986.
- Gottardi, G., and Galli, E. (1985) *Natural Zeolites*. Springer-Verlag, Berlin, 18, 409 pp.

Gualtieri, A., Artioli, G., Passaglia, E., Bigi, S., Viani, A., and Hanson, J.C. (1998) Crystal structure-crystal chemistry relationships in the zeolites erionite and offretite, *American Mineralogist*, 83, 590-606.

Hay, R. L., and Sheppard, R. A. (2001) Occurrence of zeolites in sedimentary rocks: an overview, *Reviews in Mineralogy and Geochemistry*, 45, 217-234.

IARC: International Agency for Research on Cancer (1987a) IARC Monographs on the Evaluation of Carcinogenic Risks to Humans, Silica and Some Silicates, Lyon, France, 42, 289.

IARC: International Agency for Research on Cancer (1987b) IARC Monographs on the Evaluation of Carcinogenic Risks to Humans, Overall Evaluations of Carcinogenicity, Lyon, France, Supplement 7, 440.

Kalló, D. (2001) Applications of natural zeolites in water and wastewater treatment, *Reviews in Mineralogy and Geochemistry*, 45, 519-550.

Kuntzinger, S., Ghermani, N.E., Dusausoy, Y., and Lecomte, C. (1998) Distribution and topology of the electron density in an aluminosilicate compound from high-resolution X-ray diffraction data: the case of scolecite, *Acta Crystallographica B*54, 819-833.

Meier, W.M., Olson, D.H., and Baerlocher, C. (1996) *Atlas of Zeolite Structure Types*: 4<sup>th</sup> revised edn. Zeolites 17:1-230 (<http://www.iza-structure.org/databases>)

Pabalan, R. R., and Bertetti, P. F. (2001) Cation-exchange properties of natural zeolites, *Reviews in Mineralogy and Geochemistry*, 45, 453-518.

Palmer, D. (2015) *CrystalMaker and SingleCrystal: Interactive crystallography for the Macintosh*. CrystalMaker Software, Oxfordshire, UK, [www.crystallmaker.com](http://www.crystallmaker.com).

Passaglia, E., Artioli, G., and Gualtieri, A. (1998) Crystal chemistry of the zeolites erionite and offretite, *American Mineralogist* 83, 577-589.

Pooley, F.D. (1979) Evaluation of fiber samples taken from the vicinity of two villages in Turkey, *Dust and Disease*, Pathodox Publication: Park Forest South, IL, 41.

Saini-Eidukat, B., and Triplett, J.W. (2014) Minerals in the Human Body: Erionite and offretite from the Killdeer Mountains, Dunn County, North Dakota, U.S.A., *American Mineralogist*, 99, 8-15.

Simoncic, P., and Armbruster, T. (2004) Peculiarity and defect structure of the natural and synthetic zeolite mordenite: A single-crystal X-ray study, *American Mineralogist*, 89, 421-431.

Tschernich, R.W. (1992) *Zeolites of the World*, Harbinger House.

Wise, W. S., and Tschernich, R. W. (1976) The chemical compositions and origin of the zeolites offretite, erionite, and levyne, *American Mineralogist* 61, 853-863 pp.

Van Gosen, B. S., Blitz, T. A., Plumlee, G. S., Meeker, G. P., and Pierson, M. P. (2013) Geologic occurrences of erionite in the United States: an emerging national public health concern for respiratory disease, *Environmental Health and Geochemistry*, 35, 419-430.

Yamate, G., Agarwal, S.C., and Gibbons, R.D. (1984) Methodology for the measurement of airborne asbestos by electron microscopy, EPA report draft, 31.

Table 1.1

| <i>Zeolite Name</i> | <i>Geologic Environment</i> | <i>Location</i>                                  |
|---------------------|-----------------------------|--|
| erionite            | altered volcanic tuff       | Rome, Oregon                                     |
| erionite            | altered volcanic tuff       | Killdeer Mountains, Dunn County,<br>North Dakota |
| offretite           | basalt vesicle              | Adamello, Italy                                  |
| mordenite           | basalt vesicle              | Challis, Idaho                                   |
| scolecite           | basalt vesicle              | Poona, India                                     |

Zeolite samples and locations used in this study, noting the geologic environment.

Figure 1.1

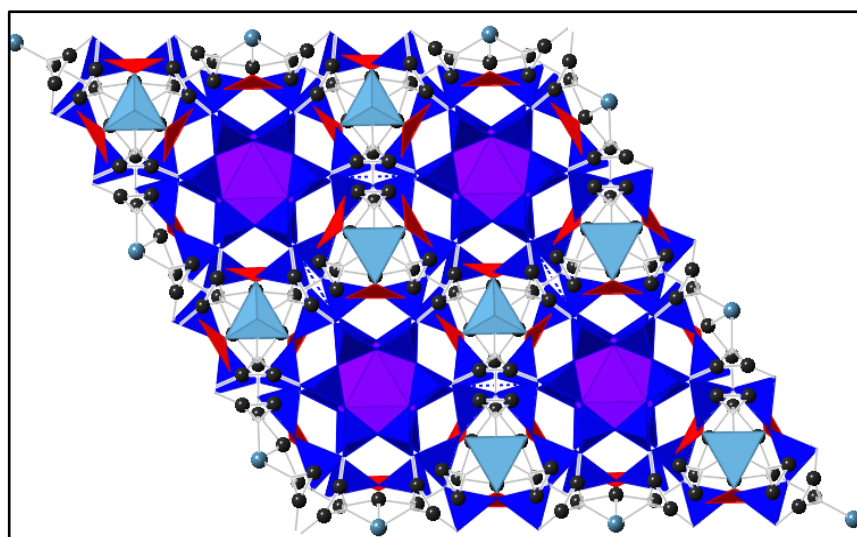
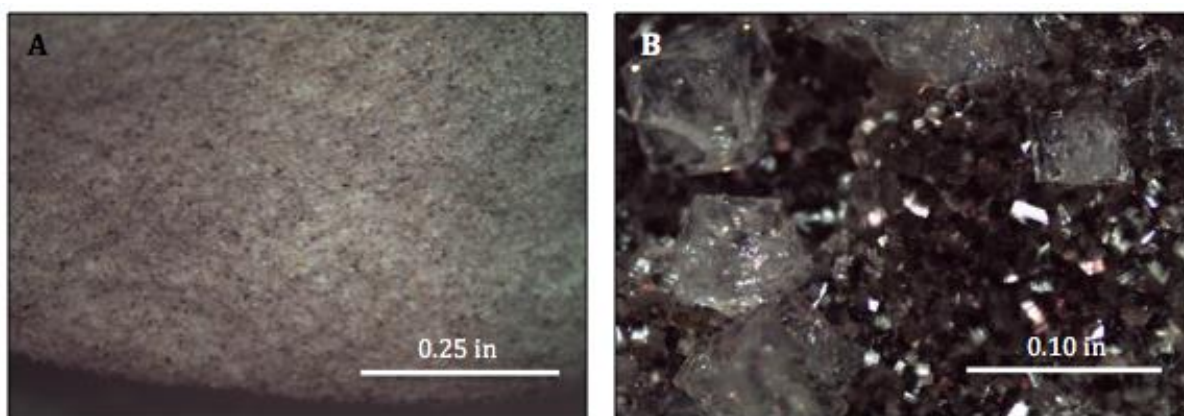


Diagram looking down the *c* axis of erionite. Si (dark blue), H<sub>2</sub>O (black), Ca (light blue), O (red), and K (purple) (Gualtieri et al, 1998).

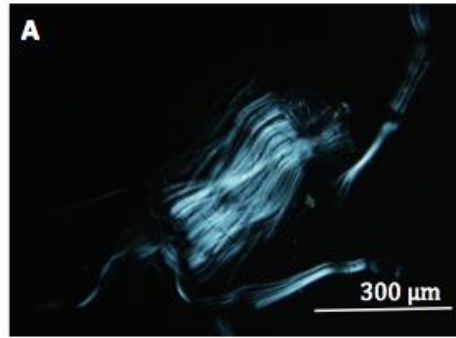


Figure 1.2



Stereoscope images (A), altered volcanic tuff from Killdeer, North Dakota containing erionite and other minerals (B), and offretite and chabazite in a basalt vesicle from Adamello, Italy.

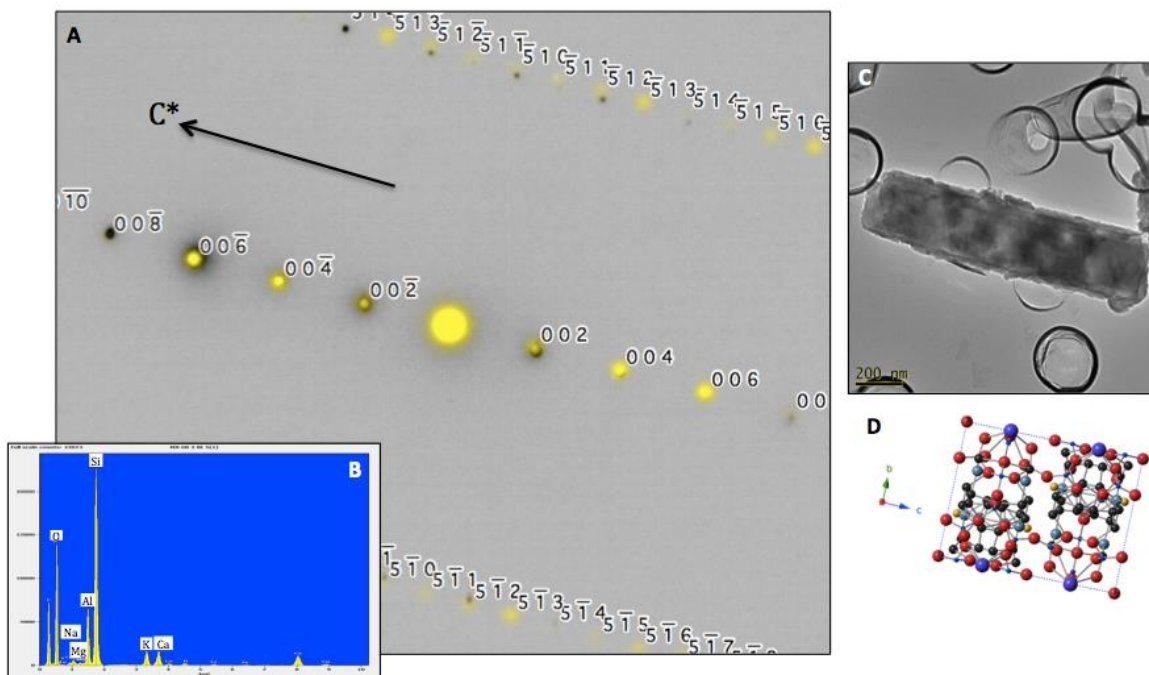
Figure 1.3



|          |   |            |       |  |       |  |
|----------|---|------------|-------|--|-------|--|
| <b>B</b> | $(K_2, Na_2, Ca, Mg)_{2.1}[Al_{4.2}Si_{13.8}O_{36}] \cdot 15H_2O$ | $\epsilon$ | 1.457 |  | 1.485 |  |
|          |   | $\omega$   | 1.455 |  | 1.483 |  |
|          | $(Na_2, K_2, Ca, Mg)_4Al_9Si_{27}O_{72} \cdot 27H_2O$             | $\epsilon$ | 1.473 |  | 1.476 |  |
|          | $(Ca, K_2, Mg)_{2.5}[Al_5Si_{13}O_{36}] \cdot 16H_2O$             | $\omega$   | 1.468 |  | 1.472 |  |
|          |   | $\epsilon$ |       |  | 1.486 |  |
|          |   | $\omega$   |       |  | 1.489 |  |
|          |   | $\omega$   |       |  | 1.491 |  |
|          |   |            |       |  | 1.493 |  |

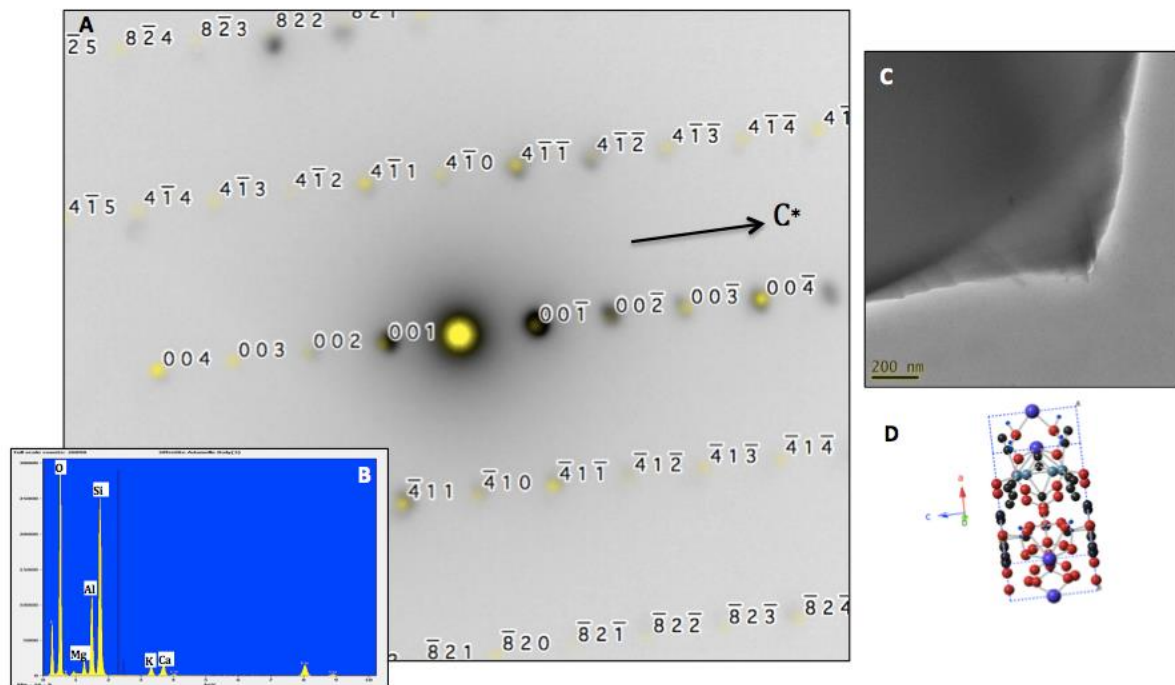
PLM image of woolly erionite from Durkee, Oregon. (B) Refractive index values for epsilon and omega of erionite and offretite (Tschernich, 1992; Deer et al, 1967). Red dotted line indicates region of no refractive index overlap.

Figure 1.4



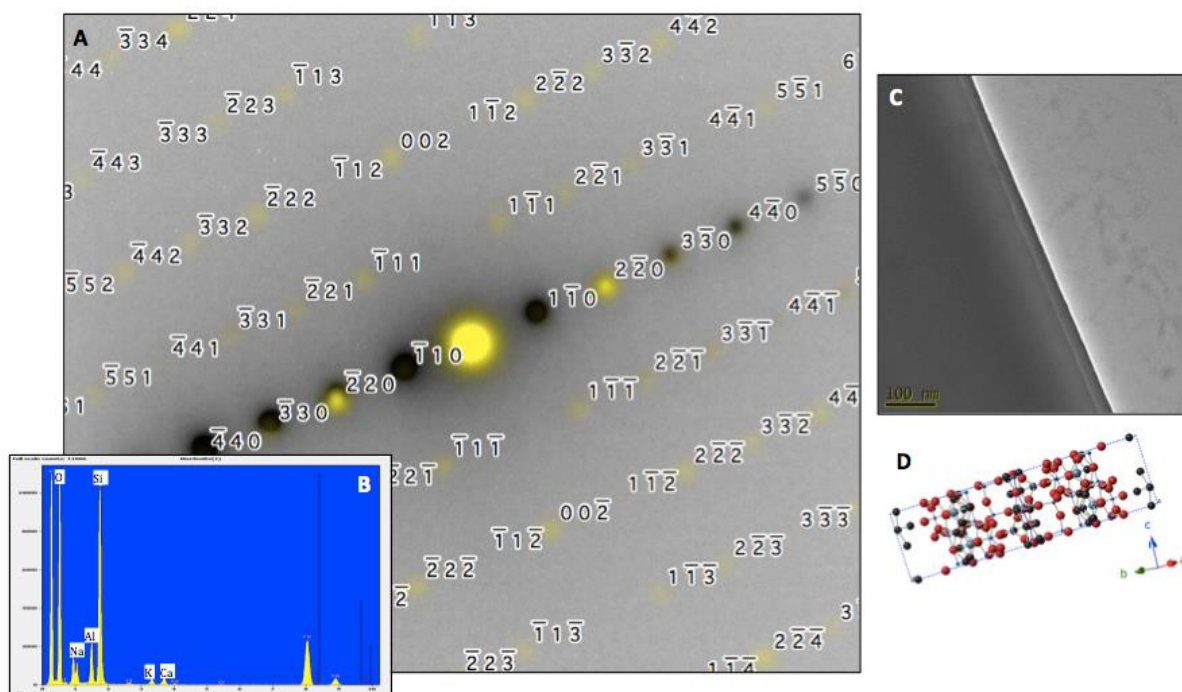
TEM results of  $[150]$  zone axis orientation of erionite from the Killdeer Mountains in North Dakota (A), simulated diffraction pattern from CrystalMaker (yellow), overlain on top of the real SAED diffraction pattern (black dots), note the systematic absences along  $c^*$  (Gualtieri et al, 1998). (B) EDS of erionite particle showing major cation content along with (C), TEM image of oriented erionite grain, and (D) CrystalMaker oriented structure diagram of erionite.

Figure 1.5



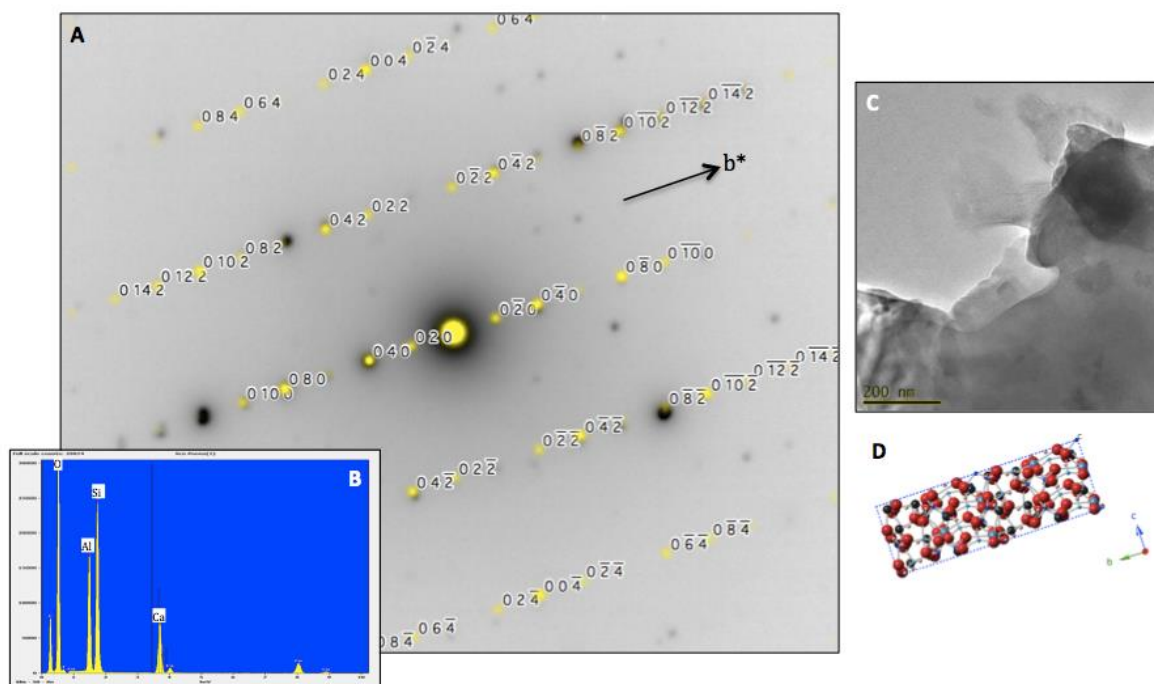
TEM results of  $[140]$  zone axis orientation of offretite from Adamello, Italy (A), simulated diffraction pattern from CrystalMaker (yellow), overlain on top of the real SAED diffraction pattern (black dots) (Gualtieri et al, 1998). (B) EDS of offretite particle showing major cation content along with (C), TEM image of oriented offretite grain, and (D) CrystalMaker oriented structure diagram of offretite.

Figure 1.6



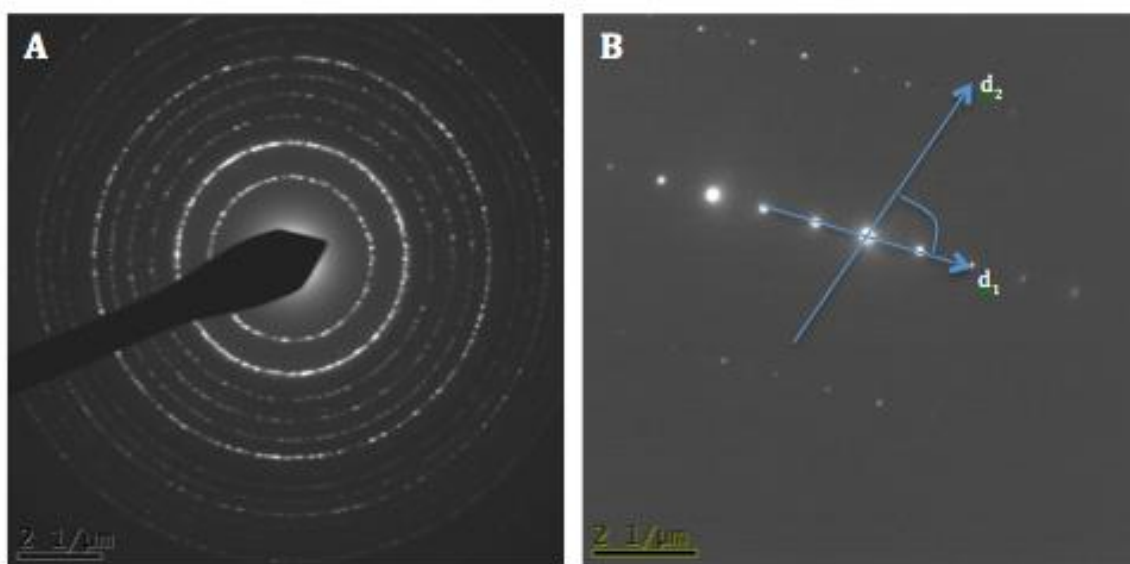
TEM results of  $[110]$  zone axis orientation of mordenite from Challis, Idaho (A), simulated diffraction pattern from CrystalMaker (yellow), overlain on top of the real SAED diffraction pattern (black dots) (Simoncic and Armbruster, 2004). (B) EDS of mordenite particle showing major cation content along with (C), TEM image of oriented mordenite grain, and (D) CrystalMaker oriented structure diagram of mordenite.

Figure 1.7



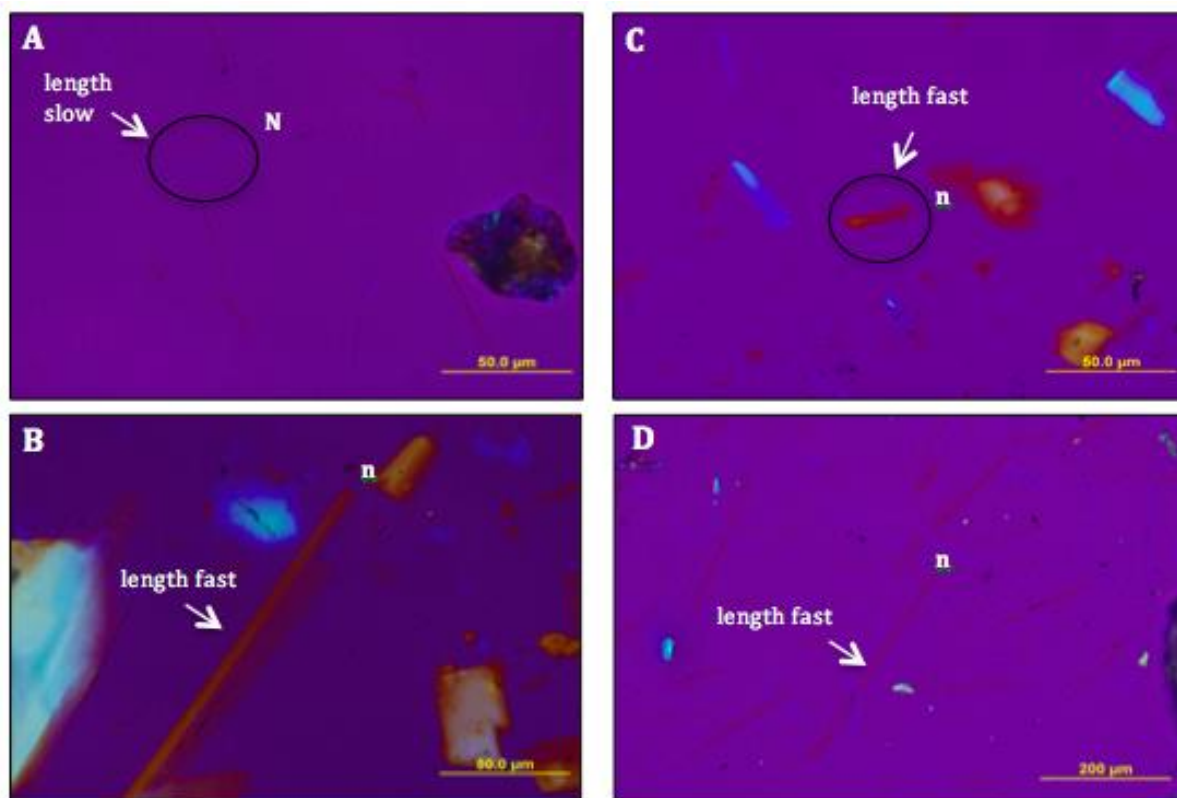
TEM results of [100] zone axis orientation of scolecite from Poona, India (A), simulated diffraction pattern from CrystalMaker (yellow), overlain on top of the real SAED diffraction pattern (black dots) (Kuntzinger et al, 1998). (B) EDS of scolecite particle showing major cation content along with (C), TEM image of oriented scolecite grain, and (D) CrystalMaker oriented structure diagram of scolecite.

Figure 1.8



Zone axis hand calculations (A), thallium chloride standard at 40cm, and (B) locations of measurements taken from Killdeer Mountain, North Dakota erionite sample.

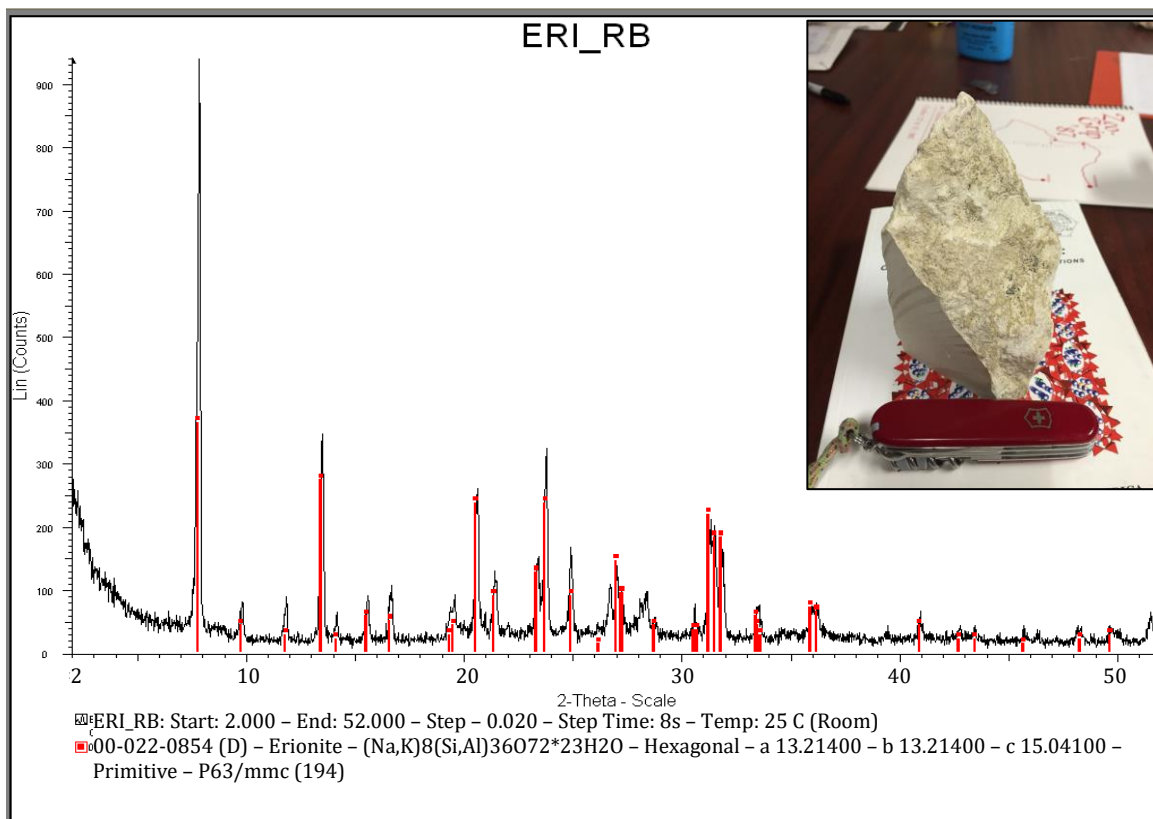
Figure 1.9



PLM images of sign of elongation test (A), Killdeer Mountain erionite in 1.484 liquid showing addition (B), Poona, India scolecite in 1.510 liquid showing subtraction (C) Adamello, Italy offretite in 1.484 liquid showing subtraction, and (C), Challis, Idaho mordenite in 1.474 liquid showing subtraction upon insertion of the wave plate.

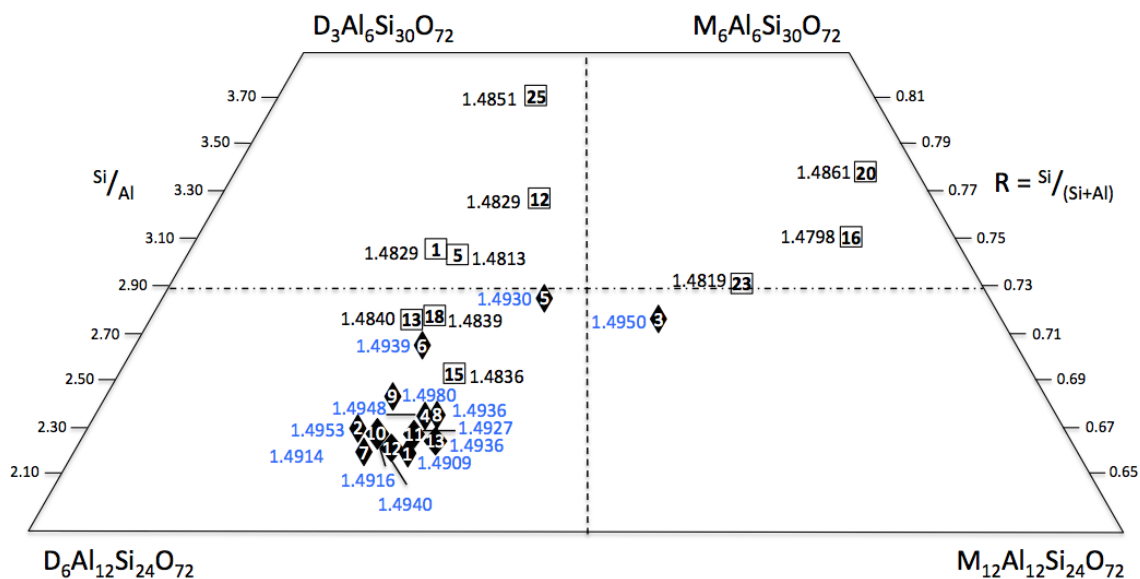


Figure 1.10



Powder XRD 3 hour scan 2-52  $\theta$  of Rome, Oregon altered volcanic tuff containing erionite, and inset picture showing hand sample with pocket knife for scale.

Figure 1.11



Modified diagram showing isolated erionite (open squares) and offretite (solid diamonds) in relation to divalent vs. monovalent cation content and Gladstone Dale values calculated using major elemental data provided by Passaglia et al, 1998.

## Chapter 2:

### Optical Analysis of the Fibrous/Acicular Zeolites: A Spindle Stage Approach

Kristina P. Pourtabib

Mickey E. Gunter

#### ABSTRACT

In recent years, analytical laboratories are observing that in addition to receiving samples containing asbestos and amphibole minerals they are noticing an increase in zeolite samples, in particular the mineral species erionite. It is now evident that a reliable method of identification is needed which uses a combination of the equipment most readily available to these analysts such as the Transmission Electron Microscope (TEM), Polarized Light Microscope (PLM), and powder X-Ray Diffractometer (XRD).

According to literature, the closely related zeolites erionite and offretite have Refractive Index (R.I.) values that do not overlap, specifically at 1.485 for epsilon ( $\epsilon$ ) in both minerals. Upon further analysis of R.I. values using various applications of the Spindle Stage and Abbe Refractometer on a suite of elongate zeolites from various locations, the R.I. of erionite and offretite for both epsilon and omega ( $\omega$ ) are seen to significantly overlap. This is most likely due to overlapping chemical compositions and hydration states of the minerals. In addition to R.I., the sign of elongation for both erionite and offretite was thought to be a means to differentiate these two species (length slow for erionite and length fast for offretite). Again, upon further investigation, the sign of elongation can also vary between these species again due to compositional similarities and frequent intergrowths/overgrowths that make determining sign of elongation anomalous.

Ultimately, preliminary PLM investigations combined with TEM analysis are required at a minimum for the identification of erionite. Until a precise chemical analysis and structural analysis can be performed on these zeolites using Electron Probe Microanalysis (EPMA) and

Single Crystal X-Ray Diffraction (SCXRD), then optical identification solely by PLM will not be a reliable technique for distinguishing erionite from offretite.

Keywords: zeolites, erionite, offretite, Optical Mineralogy, spindle stage, Abbe Refractometer, Sénarmont Compensator, Vickers A.E.I. Image Splitting Eyepiece

## INTRODUCTION

Asbestos minerals and commercial materials containing asbestos have long been encountered in the regulatory community. A standard protocol has been established for the identification of these minerals, but what happens when a relatively new mineral needs to be identified consistently and accurately? These are the issues that stem from the need for a correct identification method of the mineral erionite.

Arthur Eakle first discovered the mineral erionite in 1898 (Eakle, 1898). The discovery was made in what is now the type-locality for the mineral erionite, Durkee, Oregon, in a rhyolitic-tuff type deposit. Eakle described the mineral to contain a very wooly habit, although this habit is more recently known to be less common of erionite. Much later following the minerals discovery, studies linked erionite to cases of malignant mesothelioma (Carbone et al, 2012). Erionite-related cases of malignant mesothelioma are attributed to airborne exposure to the mineral, typically in a home or work setting where the mineral can be found abundantly in the surrounding geologic environment (not prevalent in basalt-hosted erionite samples). Links between erionite and malignant mesothelioma are most well known in the Cappadocia, Turkey case, where residents of certain villages built their homes from erionite-containing rock, and experienced a consistent and prolonged exposure to the mineral (Baris et al, 1979; Dogan et al, 2006). Other recorded instances of erionite-related malignant mesothelioma are rare, although in 2008 there were confirmed cases in the States of Jalisco and Zacatecas in Mexico also related to environmental exposure from the surrounding zeolite-rich rocks (Ilgren et al, 2008; Oczypok et al, 2016). According to the Environmental Protection Agency (EPA), erionite is currently listed as a Group I carcinogen causing both pleural and peritoneal mesothelioma to humans and animals, but erionite is not regulated by the EPA (IARC 1987a-b). The mechanisms behind the carcinogenetic properties of erionite

are still unclear, but studies have shown that a relationship between surficial Fe-nanoparticles and high surface area, due to the elongate morphology of erionite, could lend itself to producing cancerous mutations within the body (e.g., Ballirano et al, 2015).

Erionite  $K_2(Na,Ca_{0.5})_8[Al_{10}Si_{26}O_{72}] \cdot 28H_2O$  is a zeolite group mineral that occurs mainly in the vesicles of volcanic rocks or in altered volcanic tuff-type deposits (Saini-Eidukat and Triplett, 2014; Van Gosen et al, 2013). When erionite occurs in environments of diagenetically altered volcanic rock the composition is typically more Si and Na-rich (Passaglia et al, 1998). Erionite has a space group of  $P6_3/mmc$  characterized by offretite-type stacking faults with various cage structures and channels that run perpendicular to the c-axis. The various cage structures, along with the cations they most commonly contain, include, a six-membered empty double ring, a cancrinite cage with mainly K, and an erionite cage with varying amounts of Ca, Na, and Mg. The zeolite mineral offretite ( $KCaMg[Al_5Si_{13}O_{36}] \cdot 15H_2O$ , space group of  $P\bar{6}m2$ , found in vesicles of volcanic rocks) was also focused on in this study as it is very similar structurally and chemically to erionite and they can be easily misidentified (Armbruster and Gunter, 2001; Passaglia et al, 1998; Pourtabib and Gunter, 2015). Another aspect attributing to the confusion between the identification of erionite and offretite are the frequent intergrowths and overgrowths that can occur between these minerals and with other zeolites such as levyne. Erionite and offretite intergrowths occur less frequently in nature, and Mg is the primary factor that determines whether erionite or offretite will crystallize. Erionite is more commonly found overgrown on levyne while offretite can more commonly be found overgrown on the zeolite mineral chabazite (Armbruster and Gunter, 2001; Passaglia et al, 1998; Wise and Tschernich, 1976; Kokotailo, 1972).

The hydration state (i.e. orientation and quantity of  $H_2O$  molecules) of erionite and offretite can also affect the R.I. In most zeolites R.I. will decrease upon dehydration, but once the zeolite structure collapses, the R.I. will again increase, reflecting changes in the electron density of the sample. When zeolite structures are partially or fully dehydrated (before structure collapse), the cations will migrate within the structure also causing reorientation of  $H_2O$  molecules and changes in refractive index. Typically when erionite is dehydrated, the monovalent K cation is driven out of the cancrinite cage by the divalent cation Ca. Since zeolites are framework silicates, there is not a great difference between the large and small

R.I. values, thus, small changes in crystal structure and chemistry can affect crystal optics. Differences in H<sub>2</sub>O contents of erionite and offretite, as seen in their generalized chemical formula for one unit cell, can also affect R.I. values. Since H<sub>2</sub>O has a high refractivity, a sample with higher H<sub>2</sub>O contents can be predicted to have a higher overall R.I. (Gunter and Ribbe, 1993; Palmer and Gunter, 2000; Ballirano and Cametti, 2012).

Problems encountered with discriminating between erionite and offretite species is an ongoing issue for many analytical labs developing efficient identification protocols. Many labs only have access to instruments like the PLM, TEM, and possibly a powder XRD. PLM techniques for identification were assumed to be straightforward when observing changes in retardation ( $\Delta$ ) and differences in R.I. values. Since both erionite and offretite occur most often in elongate habits, and are both uniaxial with erionite being optically positive (+) while offretite is optically negative (-), optical identification appeared to be straightforward. However, due to the variable chemistry, and presence of intergrowths and overgrowths, PLM alone proves to be uncertain for differentiating erionite and offretite. Methods most commonly used on the PLM in the past have been the sign of elongation test and the Becke Line Test. For the sign of elongation test erionite was thought to be length slow while offretite is length fast (Sheppard, 1996; Deer et al, 2013). Note that sign of elongation is not the same thing as optic sign (Bloss, 1999). Because of frequent intergrowths and overgrowths initial optical determinations by the sign of elongation were inconclusive for erionite and offretite. This method, once frequently used to differentiate these two zeolite species, has since been discounted as a sole means of identification due to the overlapping Si/Al ratios of erionite and offretite that correlate to R.I. (Passaglia et al, 1998). Also, according to literature, it was thought that erionite and offretite could be easily differentiated by comparing differences in R.I. values, ( $\epsilon$  in erionite  $< 1.485$  while  $\epsilon$  in offretite  $> 1.485$ ); this is also an unreliable means of identification (Figure 2.1; Tschernich, 1992; Gottardi and Galli, 1985; Deer et al, 1967). Optical data for erionite, offretite, and other fibrous/acicular zeolites in general is sparse, and not always explained in detail. However, certain studies such as by Gunter and Ribbe, 1993, thoroughly explain optics in relation to crystal chemistry (Appendix A). It is important to characterize these elongate zeolites with as much detail as possible in order to understand the relation between optics, structure, and chemistry. This can be accomplished by combining

precise EMPA chemical data, and structural data either by SCXRD or SAED on the TEM in order to better understand the crystal optics at play.

## MATERIALS AND METHODS

Zeolite samples used in this study were basalt-hosted, and the majority of samples were of elongate particle morphology (Figure 2.2; Table 2.1; Figure 2.3 A-B). No altered-volcanic tuff samples were used because the particle size was too small for spindle stage optics to be performed. Sample number 35 (okenite) is not a zeolite but a sheet silicate mineral. Okenite is included in this study because it is a mineral commonly found in association with zeolites in vesicles of basalt and shares similar hand sample properties to the zeolites group minerals. For each sample location used in this study three grains were chosen for optical analysis in order to lessen the possibility of encountering irregular grains (i.e. sample location 1 provided samples 1, 1a, and 1b). The Natural History Museum of Los Angeles County, Philip Neuhoff, obtained from Shannon & Sons Minerals, and Mickey E. Gunter provided samples for this study. Zeolite identification and species names were taken directly from the already provided sample labels. Future EPMA work will better constrain the zeolite species present within this suite of samples.

### Instrumentation

Optical analyses of the zeolite samples were performed at the University of Idaho. Spindle stage analysis was performed on a Leitz Wetzlar, German 630168 microscope with 10x objective using a Supper spindle stage and spindle stage goniometer head with upper and lower arcs (Figure 2.4 A). Spindle stage microscope accessories used include a Carl Zeiss Sénarmont compensator  $\lambda/4$ , standard  $\lambda$  (530 nm) accessory plate, standard immersion cell, heated immersion cell, Leitz Wetzlar monochromator, Vickers A.E.I. Image Splitting Eyepiece (1.5x magnification), and camera. In addition to the spindle stage microscope an Olympus BH2-UMA microscope, Leica EZ4HD stereoscope, and a Bellingham and Stanley Abbe 60 Refractometer were also used in this study (Figure 2.4 B).

## Sample Preparation

Using the stereoscope, individual zeolite grains are plucked from the main vesicle and placed in a clear dish. Next, a glass fiber is set inside of a brass pin with wax, and each grain is mounted to the end of the glass fiber using generic colored nail polish. Every elongate grain is mounted so that its long axis is almost parallel to the long axis of the glass fiber, in order to simplify the spindle stage set up. After the nail polish dries, the brass pin then is placed into the spindle stage goniometer, and then onto the Supper spindle stage. Finally, the sample is centered under plane-polarized light (PPL) and ready for optical measurements.

## Methods

Once set up on the spindle stage for analysis, the zeolite samples were first visually checked for particle morphology (i.e. bundle of fibers, single crystals, multiple crystals). Many zeolite samples were comprised of multiple single grains, and for these samples the thickness, extinction, and Sénarmont measurements were done on one of the multiple grains. Exceptions to this measurement criterion were for fiber bundles. Fiber bundle measurements in this case were taken as an average of all the fibers. In addition, since the R.I. of zeolites are generally low, it is important to choose a R.I. liquid for use with the Vickers A.E.I. Image Splitting Eyepiece, and Sénarmont Compensator that is different from a oil/crystal match in order to ensure there is enough sample relief to make accurate measurements.

### *Sign of Elongation*

The sign of elongation test for each zeolite sample is used to determine if there are any possible intergrowths or overgrowths present. Intergrowths and overgrowths can exhibit more than one sign of elongation on a single crystal, but generally either the tip or core of an elongate grain will be the most common place for this to be seen (Figure 2.5 A-C). The test is also used to show that sign of elongation for erionite and offretite will vary based on compositional changes within the crystal and that it is not an exclusive way to differentiate between erionite and offretite (Passaglia et al, 1998). For the sign of elongation test, the elongate particle is first oriented in a NE-SW orientation or 45° clockwise from the N-S



analyzer. This insures that the vibration direction parallel to the long axis or cleavage is being measured. The analyzer is then inserted so that the crystal is viewed in cross-polarized light (XPL) and the accessory plate ( $1\lambda$  or 530 nm wave plate) is inserted. If there is an increase in the interference colors (retardations add = positive elongation) according to the Michel-Lévy chart then the vibration direction closest to the long axis or cleavage is the slow ray and the mineral is length slow. Vice versa, if there is a decrease in interference colors (retardations subtract = negative elongation) then the vibration direction closest to the long axis or cleavage is the fast ray and the mineral is length fast (Bloss, 1999; Dyar and Gunter, 2008). Remember, the sign of elongation is not the same as optic sign.

#### *EXCALIBR and 2016 Modified Version*

Data for this study were recorded and calculated using a 2016 modified version of the program EXCALIBR originally created by Bloss and Reiss (1973), and most recently modified by Gunter et al. (2005) (Gunter et al, 1988; Gunter and Schares, 1991). The 2016 modified version of EXCALIBR is formatted in excel and this user-friendly format was created by Cody Steven of the University of Idaho. This 2016 modified version of EXCALIBR was used on all of the optical analyses in this study with the exception of the Becke Line Test, sign of elongation test, and Vickers A.E.I. Image Splitting Eyepiece calculation. Additionally, extinction data along with stereographic projections were plotted for usable biaxial grains using the 2016 modified version of EXCALIBR and extinction data for uniaxial grains were plotted using the Gunter et al. (2005) version of EXCALIBR. At the time of this study, the uniaxial portion of the 2016 modified version of EXCALIBR was incomplete, hence the reason for using two different EXCALIBR versions for plotting extinction data.

#### *Vickers A.E.I. Image Splitting Eyepiece*

Measurement of particle thickness ( $t$ ) was performed using the Vickers A.E.I. Image Splitting Eyepiece. This device works by splitting the particle image to varying degrees utilizing a set of rotatable rhombohedral and right-angle prism blocks cemented together which are contained within the image splitting device. This allows for the width of particle to be found by shearing the images until they are tangent, reading the micrometer displacement,

and converting to units of length using constants unique to your microscope set up (Schubel and Schiemer, 1967). For this study, the mostly elongate particles are rotated with the particles' long axis being parallel to the lower (E-W) polarizer, the microscope is kept in PPL, and a 10x objective is used. Light is then allowed into the Vickers A.E.I. image splitting eyepiece and the micrometer displacement knob is rotated so that there is no image displacement. This value (i.e. 500.4-501.4) is then recorded as the baseline for this measurement. The micrometer displacement knob is then rotated counterclockwise until the single image is sheared into two edge-touching (red-blue) images and the value is recorded, next the same process is repeated with the knob moved in a clockwise direction and the two values are averaged. This averaged value is then multiplied by the constant determined for this microscope set up (i.e.  $1.73 \mu\text{m}$ ) and the resultant thickness is determined. Accuracy of measurements taken using this device can be as high as  $0.0001 \text{ mm}$  ( $= 0.1 \mu\text{m}$ ) depending on the numerical aperture (N.A.) of the objective lens used (Bloss, 1981).

#### *Sénarmont Compensator*

Measurement of sample retardation is determined by using the Sénarmont Compensator. Since the fibrous/acicular zeolites have such a small retardation ( $0.001$ - $0.02 \text{ nm}$ ), differences in retardation cannot be observed without the use of a device such as the Sénarmont Compensator. In basic terms, the Sénarmont Compensator works on the basis of converting elliptically vibrating light into linearly vibrating light of which the azimuth ( $\theta$ ) can be determined (Carl Zeiss Sénarmont Compensator and Rotary Mica Compensator operating instructions). In order to use this device, a microscope with a rotating analyzer ( $0.1^\circ$  vernier scale) and a monochromatic light source must be used. The Sénarmont Compensator differs from other accessory plates in that when inserted into the microscope the compensator can be rotated to align parallel to or perpendicular to the privileged direction of the polarizer. Generally each degree of rotation of the analyzer that produces crystal extinction (with the compensator inserted and the crystal at  $45^\circ$ ) will equate to a retardation of  $\lambda/180$  (Bloss, 1981). When taking measurements using the Sénarmont Compensator the analyzer is first rotated so that it is perpendicular to the lower polarizer (note analyzer normal setting), next, the crystal is rotated in XPL to  $45^\circ$  showing maximum interference colors, the monochromator is inserted to  $\sim 540 \text{ nm}$  ( $\sim 89.5$  messort number, green light), analyzer is then rotated until the

background is green and the grain is black (note analyzer final setting) (Figure 2.6 A-B). Retardation ( $\Delta$ ) can then be calculated using the equation  $\Delta = (\theta/180^\circ) \lambda$  (Bloss, 1981). For example, with an analyzer normal setting of 97, analyzer final setting of 126.4, and a monochromatic wavelength of 540 nm the retardation will equal 88.2 nm. From there thickness and retardation obtained from the Vickers A.E.I. Image Splitting Eyepiece and the Sénarmont Compensator can be incorporated into the simple equation for birefringence ( $\delta = t\Delta$  or  $\delta = t |N - n|$ ), whereas  $N =$  large R.I. value and  $n =$  small R.I. value.

#### *Double Variation Method*

The Double Variation Method was used on only two of the samples in this study. This method utilizes a heated immersion cell along with a monochromator (variable wavelength plate) in order to get precise crystal/R.I. matches without having to constantly change the R.I. oil in the immersion cell (Bloss, 1981). Due to the fact that the zeolite grains were very thin (5-50  $\mu\text{m}$ ), few grains exhibited a visible dispersion when there was a crystal/R.I. match, so the Becke Line test was primarily used for getting a basic R.I. match. On another note, since the grains are thin, R.I. matches only parallel to or near parallel to the long axis of the crystal are determined; the R.I. value perpendicular to the long axis of the grain was later calculated. When performing the Double Variation Method, grains are first matched closely with a R.I. liquid, the monochromator is then inserted until the Becke Line boundary is reached (line goes into the crystal and then into the liquid with minimal movement of the monochromator), this value along with the corresponding messort number (found on the side of the monochromator) and temperature is recorded. Next, the immersion cell is slightly heated (2-5°C) and the process is repeated. Eventually with enough data points, a Double Variation curve is constructed with wavelength on the x-axis and R.I. on the y-axis. In an ideal situation, it is possible to map dispersion curves for each vibration direction in the grain and match it to various R.I. values within the visible spectrum (Bloss, 1981). Since the Double Variation method proved difficult with the zeolite samples in this study, it was not used in the final data sets.

### *Abbe 60 Refractometer*

Precise oil calibrations were obtained through use of the Abbe 60 Refractometer. Data were recorded and calculated using the 2016 excel-modified version of the program EXCALIBR as previously mentioned above. The Abbe 60 Refractometer data are fit to multiple calibration curves including the Cauchy, Sellmeier, Refractometer, and Equation 1 created by Gunter (Gunter, 1989).

Once R.I. oil(s) of match are determined by using the Becke Line test or Double Variation Method, the oil is then used on the Abbe Refractometer to get a precise match of the R.I. value(s). The Abbe Refractometer uses two glass prisms to measure the critical angle of incidence for light passing through the R.I. liquid to the measuring prism (Bloss, 1981). The wavelengths of light used for the Abbe Refractometer measurements include Mercury (435.8, 546.1, 579 nm), Cadmium (467.8, 480, 508.6, 643.8 nm), and Sodium (589.3 nm). If the Becke Line test indicates two possible R.I. (i.e. 1.482/1.484) oils of match then both oils are calibrated using the Abbe Refractometer and the final values are averaged. It is important to note that all Abbe Refractometer calculations are corrected for temperature.

The first, and most widely used, calibration curve for fitting R.I. data is Cauchy's Equation. Cauchy's Equation works on the principle of dispersion, whereas refraction will vary with varying wavelengths of light  $n_{\lambda} = c_1 + (c_2/\lambda^2) + (c_3/\lambda^3) \dots$   $n_{\lambda} = \text{R.I.}$ ,  $c = \text{Cauchy Constants}$ , and  $\lambda = \text{wavelengths (nm) of light}$ . The Sellmeier Equation is similar to the Cauchy Equation, but it takes into account selective absorption bands that may occur near or in the visible spectrum,  $n^2 = 1 + \{(A\lambda^2) / (\lambda^2 - \lambda_o^2)\}$  where  $n = \text{R.I.}$ ,  $\lambda = \text{wavelength (nm)}$ ,  $\lambda_o = \text{wavelength of maximum absorption}$ ,  $A = \text{absorption band (constant)}$  (Bloss, 1999). The Refractometer equation used was taken directly from the Abbe 60 Refractometer operating instructions manual, and the final Equation 1 by Gunter calculates a more precise R.I. value (up to the 5<sup>th</sup> decimal place) using predicted estimators from regression analysis (Gunter, 1989).

## **RESULTS**

Zeolite samples that did not provide refractive index matches using the Becke Line test were omitted from the final results of this study. Reasons for not obtaining a Becke Line

match include, if the sample was too fibrous (composed of bundles of individual grains), if extinction data were anomalous due to particle morphology and/or particle thickness, or if the sample was in an unusable orientation. Sample numbers 4b, 5, 5a, 5b, 15, 15a, 19b, 22a, 22b, 23, 23a, 23b, 34, 34a, 34b, 36, 36a, 36b, 37, 37a, 37b, 41, 42, and 42a were excluded from the results of this study. Again it is important to note that the sample names used in these results came directly from the labeled samples and future compositional using SAED and SCXRD work might alter some of these name designations.

### *Sign of Elongation*

Although the sign of elongation test was performed on all of the zeolites in this study, only the results of erionite and offretite-containing samples were analyzed due to their similar composition and structure (Figure 2.7). From the samples analyzed, it is apparent that there is much overlap between length fast and length slow sign of elongations for both erionite and offretite. In partial agreement with earlier studies (Sheppard, 1996; Deer et al, 2013), the majority of erionite samples were found to be length slow, while the majority of offretite samples seemed to be a mix of both length fast and length slow possibly relating to the presence of overgrowths or intergrowths. Samples labeled as being erionite/offretite intergrowths were length slow while samples labeled as offretite intergrowths were found to be length fast.

### *Refractive Index Values*

Upon completion of optical analyses, R.I. values for each sample are recorded on an N (slow) vs. n (fast) scatter plot (Figure 2.8). The variables N and n are used to represent the largest (N) and smallest (n) R.I. values for each mineral so that all zeolite samples can be plotted together regardless of optical class (i.e. uniaxial or biaxial). For the elongate zeolite samples, the R.I. value parallel or near parallel to the long axis of the crystal is approximately measured using the Becke Line Test and further refined after performing an oil calibration on the Abbe 60 Refractometer. The other R.I. value is then calculated solving for either N or n in the equation for birefringence. It is important to note that zeolite samples of the same species may appear to cluster together on the N vs. n plot, but this is likely due to the samples originating from the same location, thus having similar compositions. For this study, erionite

and offretite comprised the majority of zeolite samples analyzed, so R.I. values for the other zeolites might not be equally representative. Generally, all of the zeolite samples plotted below 1.500 for both N and n while okenite, the non-zeolite mineral, plotted above 1.515 for both R.I. values. When looking at the N vs. n data for just erionite, offretite and intergrowths (overgrowths), no clear pattern can be observed between the large and small R.I. values (Figure 2.9). This point further shows that R.I. values for erionite and offretite cannot be distinguished based on optic analysis alone. Other minerals such as mordenite and natrolite have R.I. values that can overlap with erionite and offretite but they are both biaxial while erionite and offretite are uniaxial making differentiation by PLM possible (Tschernich, 1992; Gottardi and Galli, 1985; Deer et al, 1967). Expanded N vs. n graphs for the other zeolite minerals can be viewed in Figures 2.10 – 2.11.

#### *Birefringence and Retardation*

The birefringence and retardation for each sample was compared on a scatter plot for each mineral (Figure 2.12). Remember, retardation and birefringence were calculated using a combination of the Sénarmont Compensator and Vickers A.E.I. Image Splitting Eyepiece. The graph's results are consistent with what is to be expected with zeolite minerals, a low birefringence and retardation. Again, zeolites are framework silicate minerals so they typically display low, first order interference colors under XPL meaning there is a very small difference between R.I. values. The majority of erionite, offretite, and intergrowth (overgrowth) samples appear to be clustered at the lower end of birefringence and retardation values, while the other zeolite samples are more scattered.

## **DISCUSSION**

Optical identification of the zeolites erionite and offretite should be used in combination with other identification methods such as TEM, EPMA, SCXRD, and XRD. The sign of elongation test alone should no longer be used to differentiate between erionite and offretite. With the precise optical analysis of a large zeolite sample set, it is easy to see that erionite and offretite overlap significantly when it comes to sign of elongation and R.I. The role that intergrowths and overgrowths play in affecting zeolite optics is still unclear, so

again, future studies are needed to better highlight this connection. Overall, a much more realistic picture of the R.I. ranges for both  $\epsilon$  and  $\omega$  for erionite and offretite was achieved in this study as compared to the narrow range of R.I. values defined in previous literature. Differences in environments of formation of these zeolite species, H<sub>2</sub>O content, and cation content will always be a major factor in controlling the R.I. of these samples. Optics alone is not an exact determination of crystal chemistry or structure for erionite and offretite.

## **FUTURE WORK**

Future work on these fibrous/acicular zeolites will include more precise chemical determinations using EPMA. Since, optical identification of these zeolites is more of an indirect method of investigation, it is important to continue to emphasize the identification of these fibrous/acicular zeolites using a suite of analyses. This idealized suite of analyses include using Selected Area Electron Diffraction (SAED) on the TEM for structural characterizations and/or SCXRD, PLM for indirect analysis, and using Wavelength Dispersive Spectroscopy (WDS) on EPMA for precise chemical compositions if available. In the future, after EPMA with these samples are complete, the now polished epoxy-hosted zeolite samples will again be analyzed optically under the PLM for potential correlations between changes in sign of elongation and changes in chemical composition of individual grains. The most interesting samples in this study came from the Ajo. District of Pima, Co., AZ, USA (Figure 2.13). The majority of these samples were large, single crystals, and had distinctive intergrowths/overgrowths on the grains. Samples like these will help to better constrain the chemical changes associated with intergrowths and overgrowths of erionite, offretite, and other zeolite species. This will provide more insight into how variations in chemical composition and structure affect the optics of the fibrous/acicular zeolite samples.

## **ACKNOWLEDGEMENTS**

I would like to thank the Natural History Museum of Los Angeles County for providing the majority of the zeolite sample used in this study, Philip Neuhoff, obtained from Shannon & Sons Minerals, and Mickey E. Gunter for also providing outstanding zeolite

samples. Finally, I would like to thank Cody Steven for creating this amazing modified version of the EXCALIBUR program, without it, this study would have taken much longer.



**REFERENCES CITED**

- Armbruster, T., and Gunter, M. E. (2001) Crystal structures of natural zeolites, *Reviews in Mineralogy and Geochemistry*, 45, 1-67.
- Ballirano, P., and Cametti, G. (2012) Dehydration dynamics and thermal stability of erionite-K: Experimental evidence of the “internal ionic exchange” mechanism. *Microporous and Mesoporous Materials*, 163, 160-168.
- Ballirano, P., Pacella, A., Cremisini, C., Nardi, E., Fantauzzi, M., Atzei, D., Rossi, A., and Cametti, G. (2015) Fe (II) segregation at a specific crystallographic site of fibrous erionite: A first step toward the understanding of the mechanisms inducing its carcinogenicity. *Microporous and Mesoporous Materials*, 211, 49-63.
- Bariş, Y. I., Artvinli, M., and Şahin, A. A. (1979) Environmental mesothelioma in Turkey. *Annals of the New York Academy of Sciences*, 330(1), 423-432.
- Bloss, F. D., and Riess, D. (1973) Computer determination of 2V and indicatrix orientation from extinction data. *American Mineralogist*, 58, 1052-1061.
- Bloss, F.D. (1981) *The Spindle Stage: Principles and Practice*. Cambridge University Press. New York, N.Y. 120-121, 198-200, 265-268, 274-275.
- Bloss, F. D. (1999) *Optical Crystallography*, Mineralogical Society of America, 5, 119-121.
- Carbone, M., Ly, B. H., Dodson, R. F., Pagano, I., Morris, P. T., Dogan, U. A., Gazdar, A.F., Pass, H.I., and Yang, H. (2012) Malignant mesothelioma: facts, myths, and hypotheses. *Journal of cellular physiology*, 227(1), 44-58.
- Dyar, M. D., and Gunter, M.E. (2008) *Mineralogy and Optical Mineralogy*, Mineralogical Society of America, Chantilly, V.A., 708.
- Deer, W.A., Howie, R.A., and Zussman J. (2013) *Rock Forming Minerals: Volume Four: Framework Silicates*, Longmans, 355-362.
- Dogan, A. U., Baris, Y. I., Dogan, M., Emri, S., Steele, I., Elmishad, A. G., and Carbone, M. (2006) Genetic predisposition to fiber carcinogenesis causes a mesothelioma epidemic in Turkey. *Cancer Research*, 66(10), 5063-5068.
- Eakle, A. S. (1898) Erionite, a new zeolite. *American Journal of Science*, (31), 66-68.
- Gottardi, G., and Galli, E. (1985) *Natural Zeolites*. Springer-Verlag, Berlin, 18, 409 pp.

Gualtieri, A., Artioli, G., Passaglia, E., Bigi, S., Viani, A., and Hanson, J.C. (1998) Crystal structure-crystal chemistry relationships in the zeolites erionite and offretite, *American Mineralogist*, 83, 590-606.

Gunter, M.E. (1989) Dispersion equations for commonly used compensator plate materials. *The Microscope*, 37(1), 1-8.

Gunter, M. E., Bloss, F. D., and Su, S. C. (1988) EXCALIBR revisited. *American Mineralogist*, 73(11-12), 1481-1482.

Gunter, M. E., and Ribbe, P. H. (1993) Natrolite group zeolites: Correlations of optical properties and crystal chemistry. *Zeolites*, 13(6), 435-440.

Gunter, M. E., Downs, R. T., Bartelmehs, K. L., Evans, S. H., Pommier, C. J., Grow, J. S., Sanchez, M.S., and Bloss, F. D. (2005) Optic properties of centimeter-sized crystals determined in air with the spindle stage using EXCALIBRW. *American Mineralogist*, 90(10), 1648-1654.

Gunter, M. E., and Schares, S. M. (1991) Computerized Optical Mineralogy Calculations. *Journal of Geological Education*, 39(4), 289-290.

Ilgren, E. B., Pooley, F. D., Larragoitia, J. C., Talamantes, M., Navarrete, G. L., Krauss, E., and Breña, A. F. (2008) First confirmed erionite related mesothelioma in North America. *Indoor Built Environ*, 17, 567-568.

IARC: International Agency for Research on Cancer (1987a) IARC Monographs on the Evaluation of Carcinogenic Risks to Humans, Silica and Some Silicates, Lyon, France, 42, 289.

IARC: International Agency for Research on Cancer (1987b) IARC Monographs on the Evaluation of Carcinogenic Risks to Humans, Overall Evaluations of Carcinogenicity, Lyon, France, Supplement 7, 440.

Kokotailo, G. T., Lawton, S., and Sawruk, S. (1972) Direct Observation of Stacking-Faults in Zeolite Erionite. *American Mineralogist*, 57(3-4), 439.

Oczypok, E. A., Sanchez, M. S., Van Orden, D. R., Berry, G. J., Pourtabib, K., Gunter, M. E., Roggli, V.L., Kraynie, A.M., and Oury, T. D. (2016) Case Report Erionite-associated malignant pleural mesothelioma in Mexico. *International Journal of Clinical and Experimental Pathology*, 9(5), 5722-5732.

Palmer, J. L., and Gunter, M. E. (2000) Optical properties of natural and cation-exchanged heulandite group zeolites. *American Mineralogist*, 85(1), 225-230.

Passaglia, E., Artioli, G., and Gualtieri, A. (1998) Crystal chemistry of the zeolites erionite and offretite, *American Mineralogist* 83, 577-589.

Pourtabib, K.P., and Gunter, M.E. (2015) Analytical approach for identification of the zeolite erionite, *The Microscope* 63(4), 175-185.

Saini-Eidukat, B. and Triplett, J.W. (2014) Minerals in the Human Body: Erionite and offretite from the Killdeer Mountains, Dunn County, North Dakota, U.S.A., *American Mineralogist*, 99, 8-15.

Schubel, J. R., and Schiemer, E.W. (1967) A Semiautomatic Microscopic Particle Size Analyzer Utilizing the Vickers Image Splitting EYEPIECE1. *Sedimentology*, 9(4), 319-326.

Sheppard, R. A., and Gude, A. J. (1969) Chemical composition and physical properties of the related zeolites offretite and erionite. *American Mineralogist*, 54(5-6), 875.

Sheppard, R. S. (1996) Occurrences of erionite in sedimentary rocks of the western United States (No. 96-18). US Geological Survey.

Tröger, W.E., Bambauer, H.U., Taborszky, F., and Trochim, H.D. (1979) Optical determination of rock-forming minerals. Schweizerbart.

Tschernich, R.W. (1992) *Zeolites of the World*, Harbinger House.

Van Gosen, B. S., Blitz, T. A., Plumlee, G. S., Meeker, G. P., and Pierson, M. P. (2013) Geologic occurrences of erionite in the United States: an emerging national public health concern for respiratory disease. *Environmental geochemistry and health*, 35(4), 419-430.

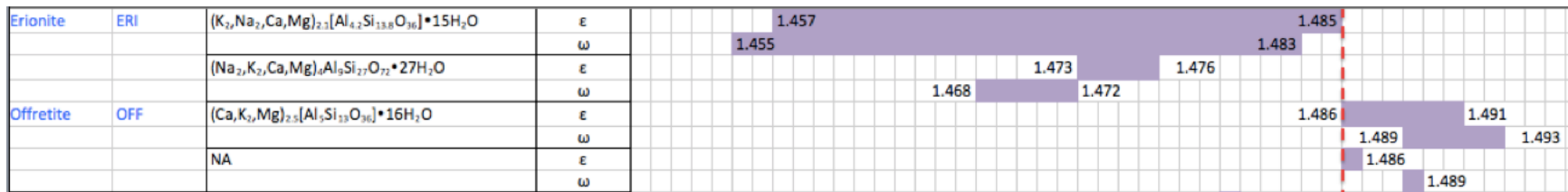
Wise, W. S., and Tschernich, R. W. (1976) The chemical compositions and origin of the zeolites offretite, erionite, and levyne, *American Mineralogist* 61, 853-863.

Table 2.1

| Sample Number | Sample Location  | Primary Zeolites                      |
|---------------|--|---------------------------------------|
| 1 and 45      | Phelps Dodge Co. Well No. 1, Little Ajo Mtns, Ajo District, Pima County, AZ, USA | erionite (Ca)                         |
| 2             | Bozarth Mesa near Hillside, Yavapai County, AZ, USA                              | erionite (K)                          |
| 3             | Phelps Dodge Co. Well No. 1, Little Ajo Mtns, Ajo District, Pima County, AZ, USA | erionite (K)                          |
| 4             | Thumb Butte, Graham County, AZ, USA  | erionite (K)                          |
| 5             | Spray, Oregon, USA   | levyne with epitaxial offretite       |
| 6             | Clifton, AZ, USA   | offretite                             |
| 7             | Adamello, Italy  | offretite, chabazite                  |
| 8             | Rock Island Dam, Washington, USA   | erionite, clinoptilolite, phillipsite |
| 9             | Chase Creek, Falkland, Kamloops Mining Division, B.C., Canada                    | erionite                              |
| 10            | Chase Creek, Falkland, Kamloops Mining Division, B.C., Canada                    | erionite                              |
| 11            | Clifton, Greenlee Co, AZ, USA  | erionite                              |
| 12            | Eureka Valley, Del Norte Co, California, USA                                     | erionite                              |
| 13            | Herbstein, Vogelsberg, Germany   | erionite                              |
| 14            | Herbstein, Vogelsberg, Hesse, Germany  | erionite                              |
| 15            | Rock Island Dam, Douglas Co, Washington, USA                                     | erionite, heulandite                  |
| 16            | Malpais Hill, Didleyville, Pinal Co, AZ, USA                                     | erionite                              |
| 17            | Chase Creek, B.C., Canada  | erionite                              |
| 18            | Pinans Lake, Westworld, B.C., Canada   | erionite                              |
| 19            | Mt. Semiol, Loire, Rhone Alps, France  | mazzite (Mg), phillipsite             |
| 20            | Greenlee Co, AZ, USA   | mesolite                              |
| 21            | Oregon, USA  | mesolite                              |
| 22            | Palermo #1, North Groton, Grafton Co, New Hampshire, USA                         | mesolite                              |
| 23            | Talisker Bay, Isle of Skye, Scotland   | mesolite                              |
| 24            | Howenegg Hegau Quarry, Baden Wurttemberg, Germany                                | natrolite                             |
| 25            | Kibblehouse Quarry, Perkiomenville, Montgomery Co, Pennsylvania, USA             | natrolite                             |
| 26            | Mt. St. Hilaire, Rouville, Quebec, Canada  | natrolite                             |
| 27            | Springfield Lane Co, Oregon, USA   | natrolite                             |
| 28            | Rock Island Dam, Douglas Co, Washington, USA                                     | offretite, erionite                   |
| 29            | Douglas Creek Road, Westworld, B.C., Canada                                      | offretite, levyne                     |
| 30            | Mont Semiol, Chatelneuf, Loire, Rhone Alps, France                               | offretite                             |
| 31            | Mt. Simieuse, Loire, France  | offretite                             |
| 32            | Mt. Simieuse Semiol, Chatelneuf, Loire, Rhone Alps, France                       | offretite, phillipsite                |
| 33            | Sasbach am Kaiserstuhl, Germany  | offretite                             |
| 34            | Yuma Co, AZ, USA   | offretite                             |
| 35            | Poona, India   | okenite                               |
| 36            | Tahiti   | scolecite                             |
| 37            | British Canadian Mine, Black Lake, Quebec, Canada                                | scolecite, chabazite                  |
| 38            | Beach, Oregon, USA   | scolecite, heulandite                 |
| 39            | Poona, India   | scolecite                             |
| 40            | limausaq Groenlandia, Jose Ignacio Garate Zubillaga Del Museo De Zapala          | tetranatrolite                        |
| 41            | Magheramorne Quarry near Larne Co Antrim, Northern Ireland                       | tetranatrolite, paranatrolite         |
| 42            | Faroe Islands  | thomsonite, chabazite, celadonite     |
| 43            | Yaquina Head, Agate Beach, Oregon, USA   | erionite                              |
| 44            | Challis, Idaho, USA  | mordenite                             |

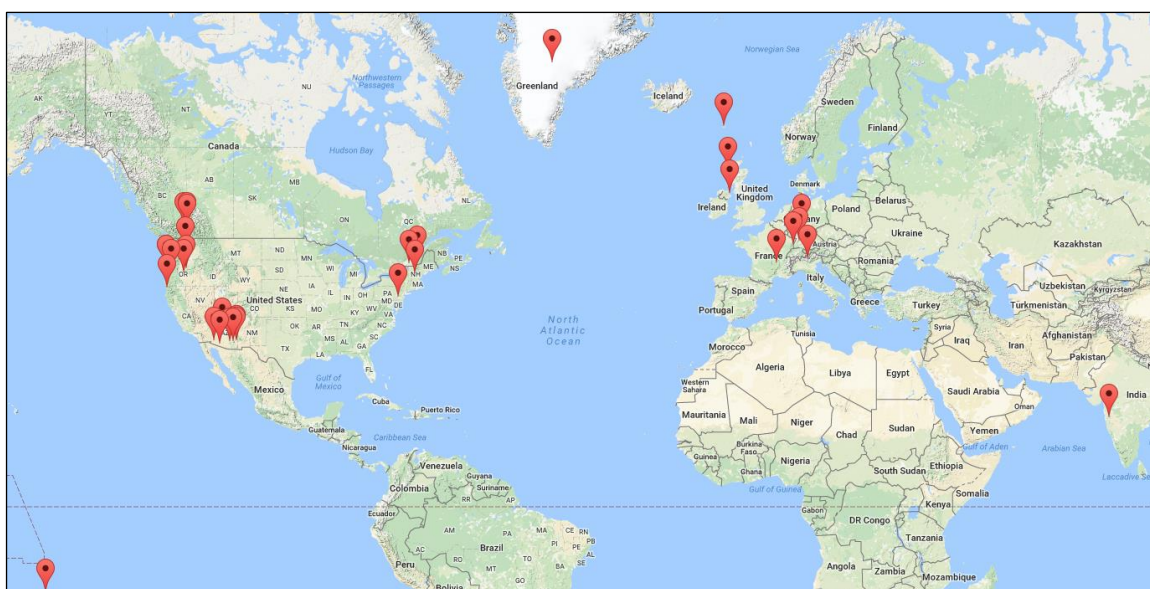
Primary zeolites found in each sample used in this study.

Figure 2.1



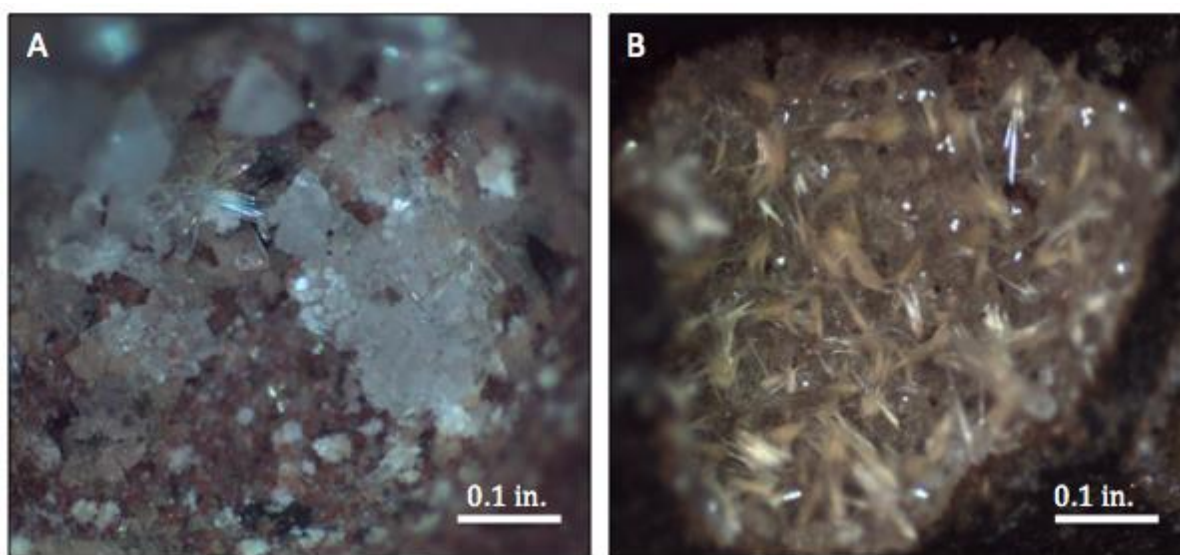
Refractive index values found in literature for erionite and offretite. Illustrating a lack of refractive index overlap around 1.485-1.486 for  $\epsilon$  in erionite and  $\epsilon$  in offretite (Tschernich, 1992; Gottardi and Galli, 1985; Deer et al, 1967).

Figure 2.2



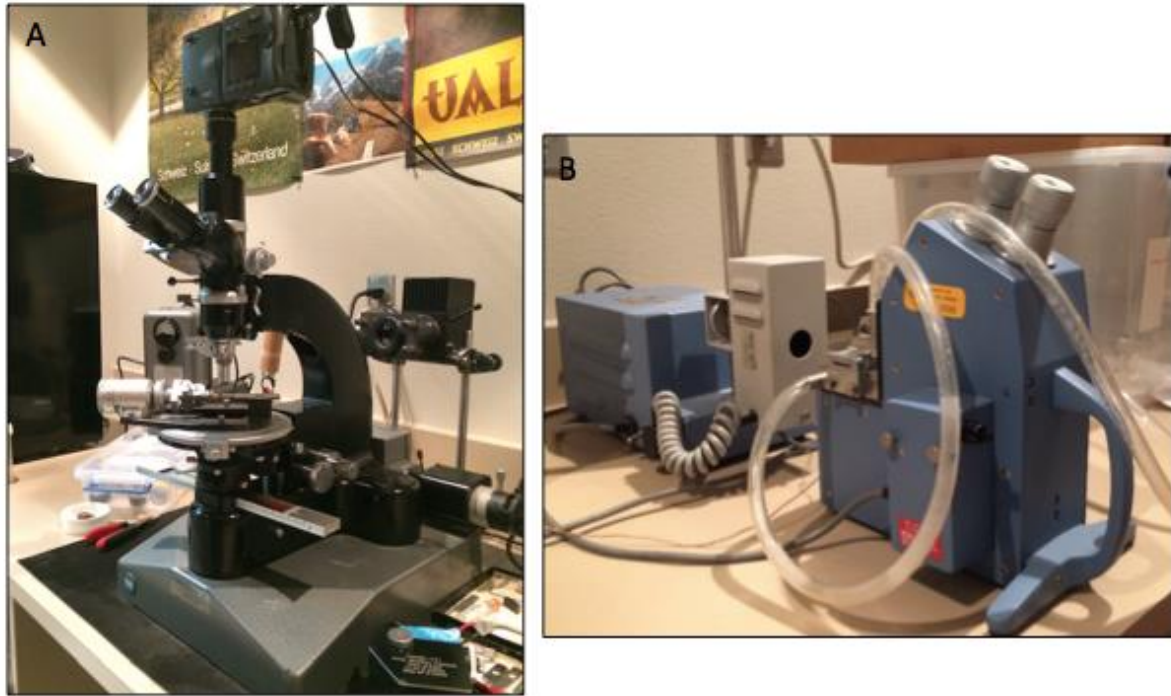
Google Map of zeolite sample locations used in this study

Figure 2.3



Stereoscopic images of elongate zeolite samples (A) erionite sample 1 (Pima Co., AZ, USA), and (B) offretite and erionite sample 28 (Rock Island Dam, Douglas Co, WA, USA).

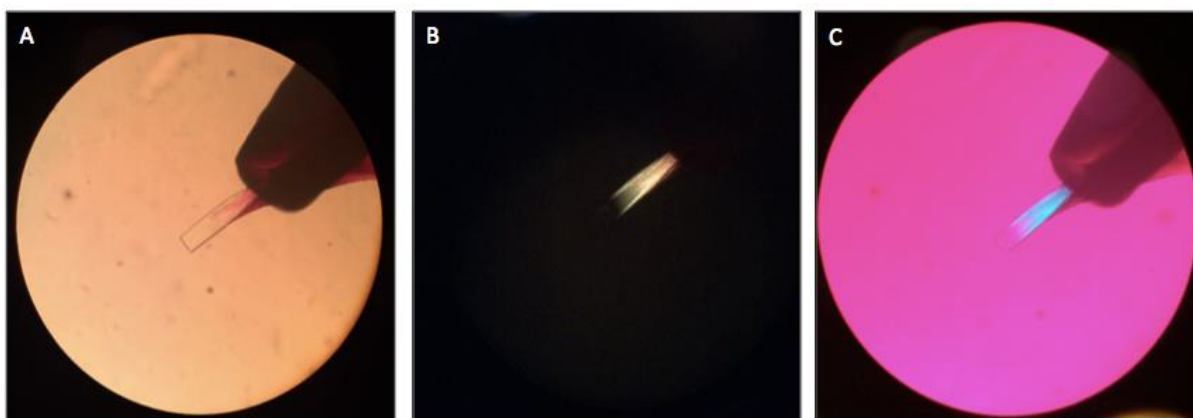
Figure 2.4



(A) Leitz microscope, fitted with a Supper spindle stage, spindle stage goniometer, Vickers A.E.I. Image Splitting Eyepiece (not shown in this image), camera, and monochromator and (B) Abbe Refractometer used in this study.

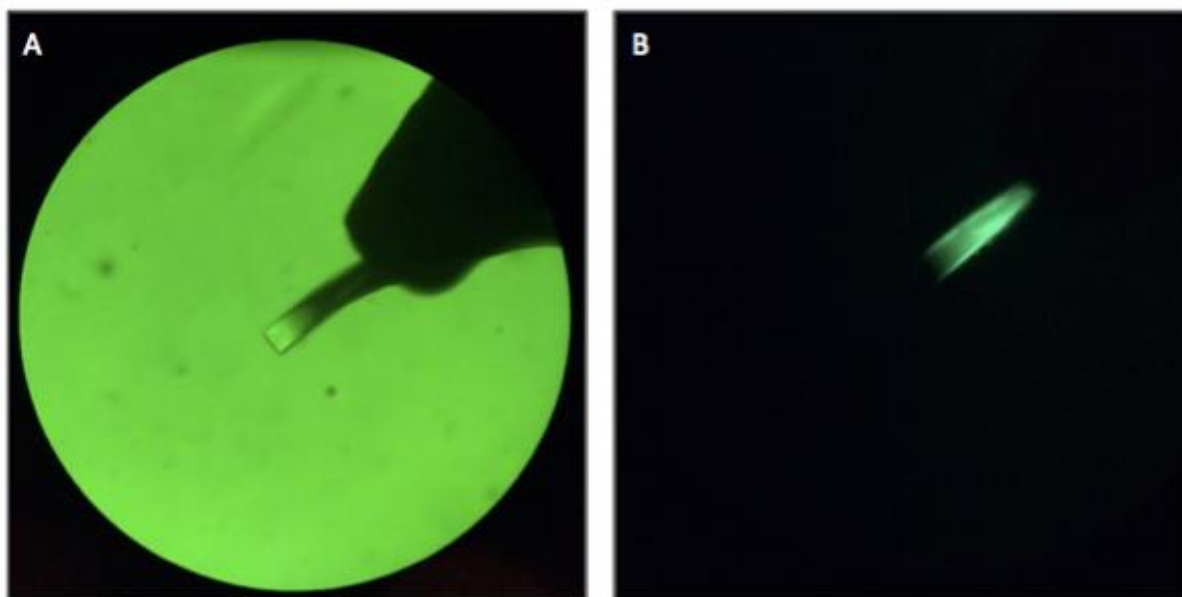


Figure 2.5



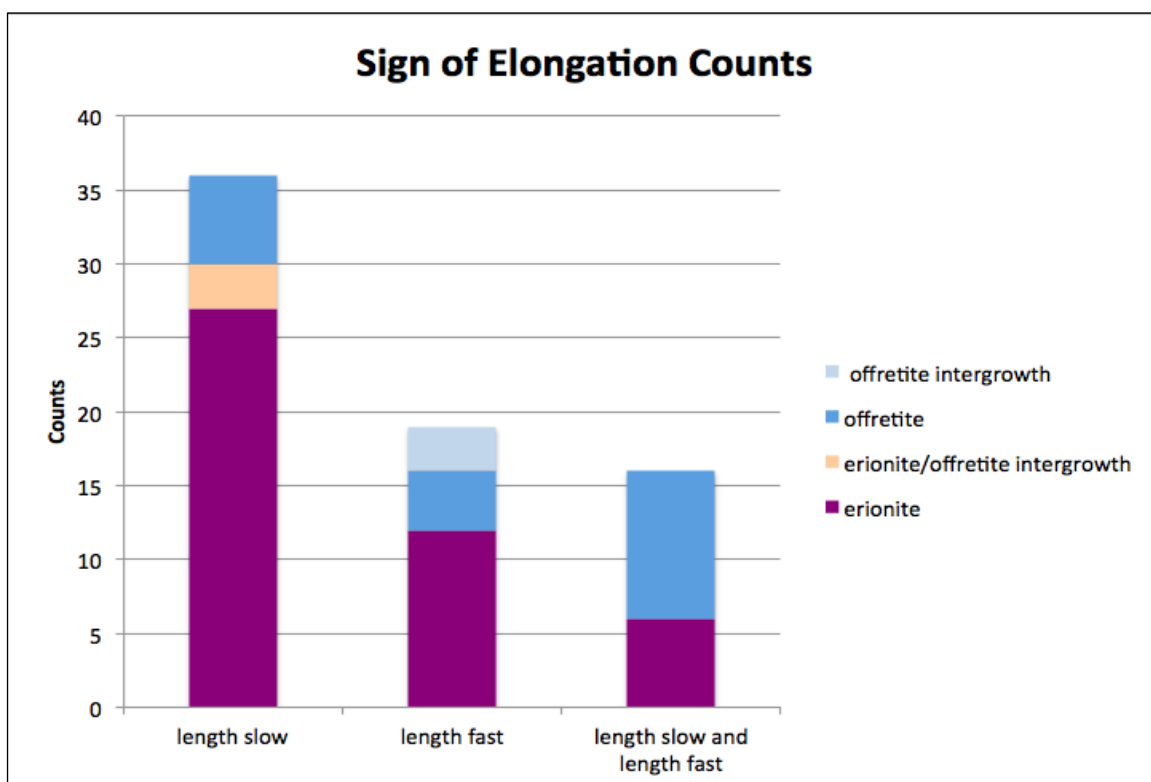
10x magnification of erionite sample number 1 (Pima Co., AZ, USA), (A) Plane Polarized Light (PPL) image, (B) Cross Polarized Light (XPL) image, (C) XPL image with 530 nm accessory plate inserted. Note: tip of grain and base of grain show different changes in retardation.

Figure 2.6



10x magnification of erionite sample number 1 using the Sénarmont Compensator. (A) PPL image of sample with monochromator inserted to about 540 nm (green). (B) Same PPL image of sample with analyzer rotated to reverse the colors.

Figure 2.7



Sign of elongation of erionite, offretite, erionite/offretite intergrowth, and offretite intergrowth samples. For this study the zeolite species determination comes directly from the labeled sample names.

Figure 2.8

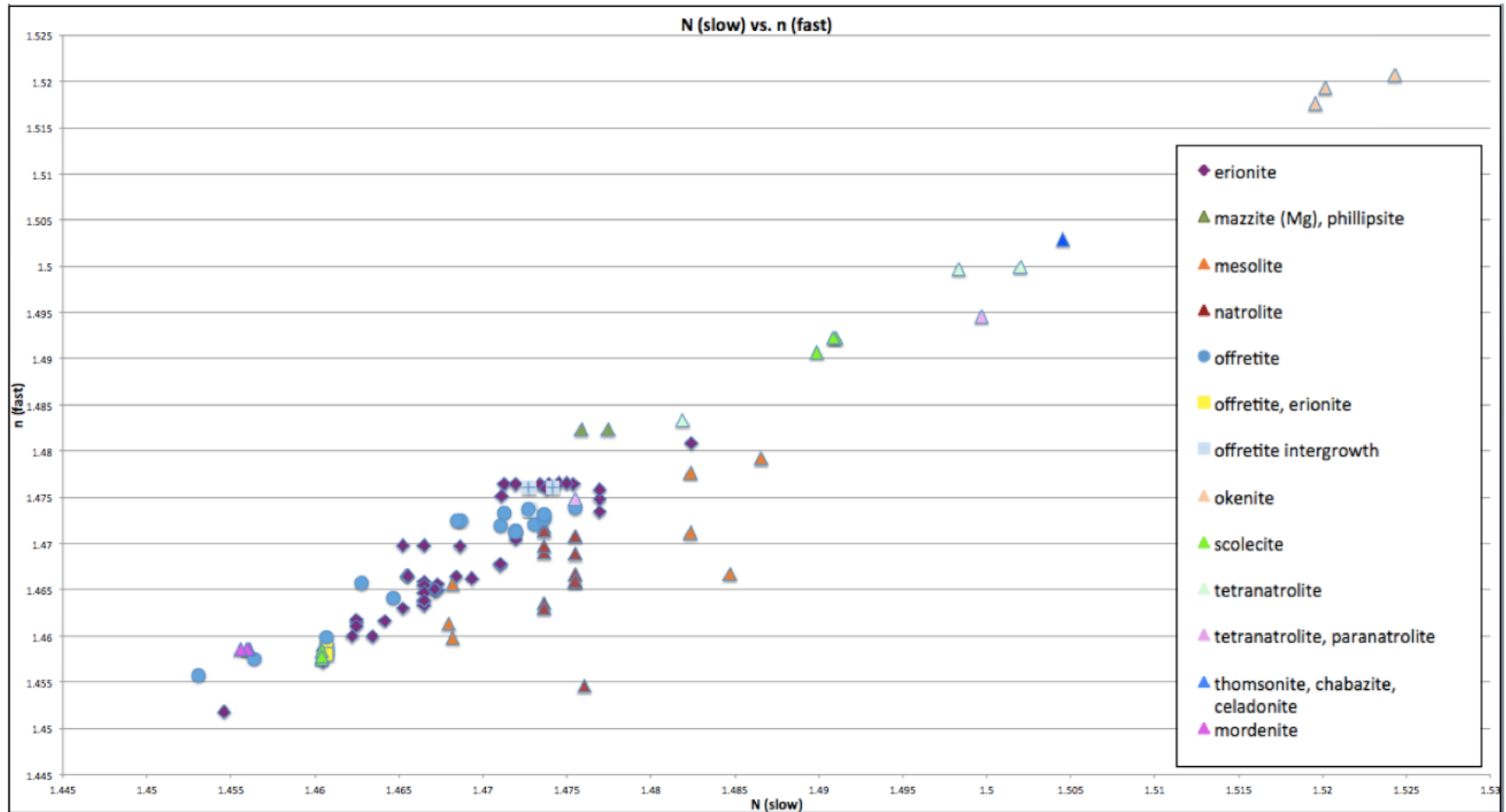
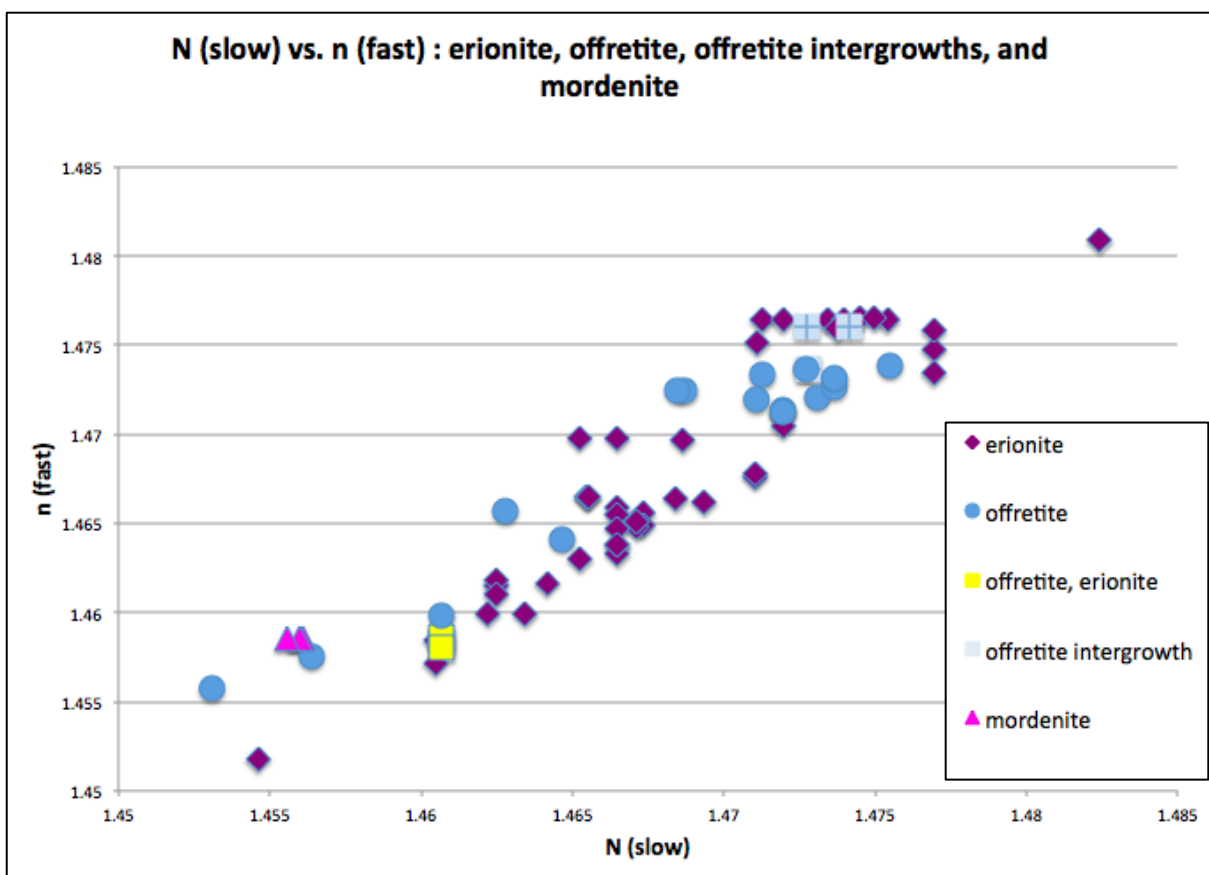


Chart displaying refractive index values for each fibrous/acicular zeolite from this study, using a combination of measured values via spindle stage analysis, and calculated values from precise oil calibrations using the Abbe Refractometer both fast and slow refractive index values were determined.

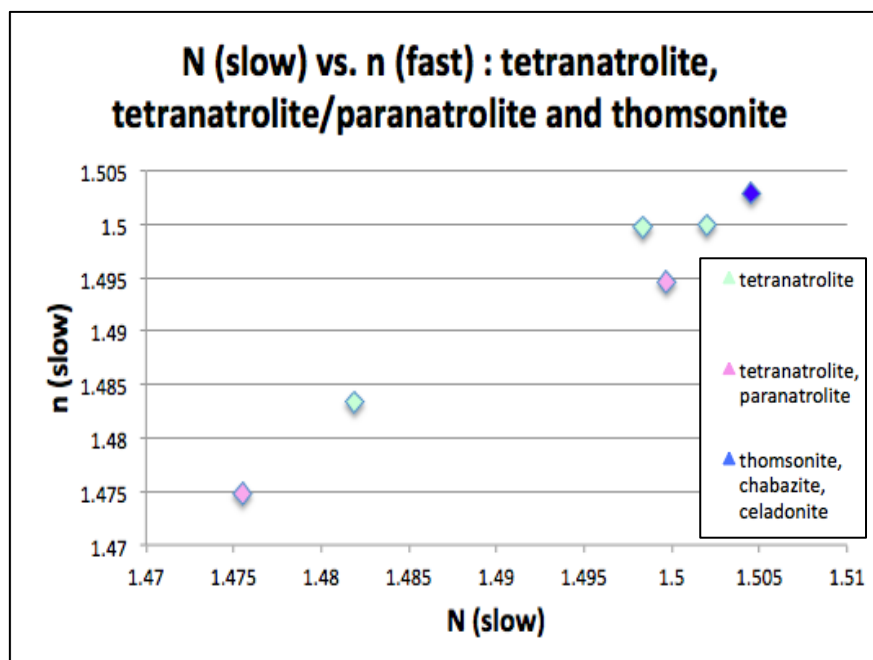
Figure 2.9



Measured and calculated refractive index values for erionite, offretite, erionite/offretite intergrowths, offretite intergrowths (or overgrowths), and mordenite.



Figure 2.11



Measured and calculated refractive index values for tetranatrolite, tetranatrolite/paranatrolite and thomsonite.

Figure 2.12

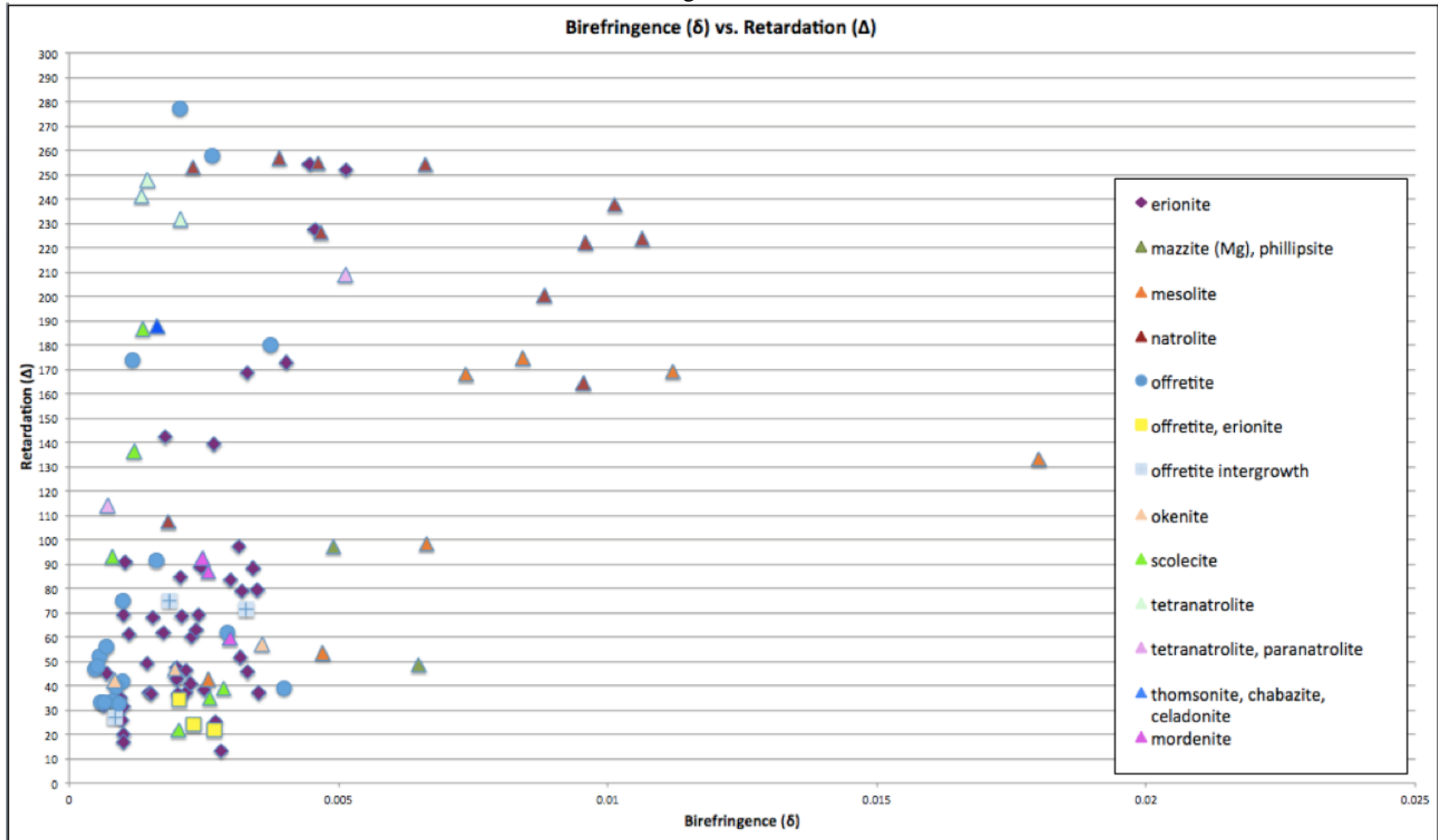
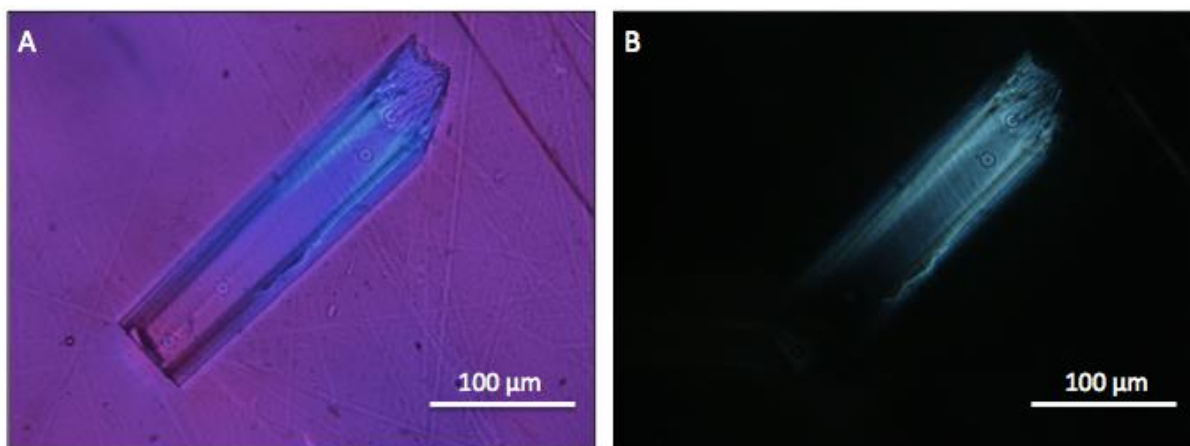


Chart displaying birefringence ( $\delta$ ) and retardation ( $\Delta$ ) for each zeolite sample. Birefringence was calculated using the Sénarmont Compensator and Vickers Image Splitting Eyepiece, while retardation was calculated using the Abbe Refractometer and the Sénarmont Compensator.



Figure 2.13



Sample 1, erionite-Ca, Phelps Dodge Co., Well no. 1, Little Ajo Mountains, Ajo District, Pima Co., AZ, USA. Sample shows a distinctive difference in sign of elongation on the tip of the grain (A) image in XPL with accessory plate inserted, (B) image in XPL.

## **Chapter 3:**

### **Relationship between Chemistry, Structure and Optics of the Zeolites Erionite and Offretite**

Kristina P. Pourtabib

Mickey E. Gunter

#### **ABSTRACT**

Erionite and offretite are two zeolite minerals that have several overlapping properties such as composition, near-similar structure, and optics. It is important to be able to differentiate between these two species because erionite has carcinogenic properties while offretite appears not to. By correlating multiple means of identification, such as electron probe microanalysis (EPMA), selected area electron diffraction (SAED), single crystal x-ray diffraction (SCXRD) and optics, trends in the data can be found. For both erionite and offretite, Mg and Ca are the two most variable cations and share an inverse relationship with one another. Length slow erionite and offretite have more Mg than Ca, while length fast erionite and offretite generally have the opposite relationship. Due to various intergrowth and overgrowth textures, as well as stacking faults, identification between these two minerals can get complicated. By taking a scale-dependent approach to data analysis, fine-scale trends in the data can be correlated to large-scale findings.

**Keywords:** Zeolites, erionite, offretite, Optical Mineralogy, Electron Probe Microanalysis, Transmission Electron Microscopy, Single Crystal XRD, Polarized Light Microscopy

#### **INTRODUCTION**

The zeolite minerals erionite and offretite share many common characteristics in their structure, composition, and optical properties. Researchers are working to better constrain these minerals both compositionally and structurally so as to establish a simpler means for identification (Passaglia et al, 1998, Gualtieri et al, 1998; Dogan et al, 2006; Dogan and

Dogan, 2008; Ballirano et al, 2009; Dogan, 2011). Although erionite occurs more frequently in nature than offretite, potential intergrowths and overgrowths of these minerals with one another and with other zeolites, as well as microstructural stacking faults can make differentiation difficult (Wise and Tschernich, 1976, Armbruster and Gunter, 1998; Passaglia et al, 1998; Gualtieri et al, 1998; Ballirano et al, 2009). It is important to practice multiple means of identification, in order to properly distinguish between these two minerals.

### *Structure and Composition*

Erionite and offretite primarily form in low pressure and low temperature environments. The main environments of formation include, altered volcanic tuff-type deposits, and crystallization in the vesicles of basalts (Sheppard, 1996; Van Gosen et al, 2013; Saini-Eidukat and Triplett, 2014). Erionite found in deposits of altered volcanic tuff are more easily erodible, thus it is more likely the setting for human exposure (Dogan et al, 2006; Pourtabib and Gunter, 2015). There are no known connections between offretite and cancer, but erionite is listed as a Group I carcinogen meaning that it is found to cause cancer in both humans and animals alike, but the mechanisms by which erionite induces cancer are still unclear (IARC, 1987a-b; Dogan et al, 2006; Dogan et al, 2008; Dogan and Dogan, 2008; Ballirano and Cametti, 2015; Ballirano et al, 2015; Matassa et al, 2015; Mattioli et al, 2015; Oczypok et al, 2016). Both erionite and offretite crystallize in the hexagonal crystal system with varying unit cell sizes (erionite:  $a=b = 13.26$ ,  $c = 15.12$  Å and offretite:  $a=b = 13.29$ ,  $c = 7.58$  Å), but both minerals have different space group symmetry (Armbruster and Gunter, 2001). Erionite has the space group  $P6_3/mmc$  while offretite contains a space group of  $P\bar{6}m2$ . This space group symmetry is one of the main ways to tell erionite from offretite when doing SAED on the TEM. The  $6_3$  screw axis found in erionite is a symmetry operation with a  $180^\circ$  rotation followed by a  $\frac{1}{2}$  translation along  $c$ , the planes of atoms created from this symmetry are reflected in the diffraction patterns of erionite by showing diffraction constraints (i.e. systematic absences) at  $00l = 2n$  along  $c^*$  (Kokotailo et al, 1972; Armbruster and Gunter, 2001; Dyar and Gunter, 2008; Pourtabib and Gunter, 2015).

Compositionally both erionite and offretite have similar formulas, but slight differences in cation content can help to distinguish between the two minerals. Erionite,  $K_2(Na,Ca_{0.5})_8[Al_{10}Si_{26}O_{72}] \cdot 28H_2O$ , and offretite,  $KCaMg[Al_5Si_{13}O_{36}] \cdot 15H_2O$ , both contain

K and Ca as some of the primary extraframework cations while Mg seems to be associated mainly with offretite, and Na is associated with erionite (Armbruster and Gunter, 2001). Both structures of erionite and offretite are composed of various channels and cages that house extraframework cations and H<sub>2</sub>O. In erionite, there are three main cage structures which include: a six-membered double ring which is empty, a cancrinite cage with K, and an erionite cage with varying amounts of Ca, Na, and Mg (Gualtieri et al, 1998; Passaglia et al, 1998; Armbruster and Gunter, 2001). In offretite, the cage structures include: a six-membered double ring which is empty or has low occupancy, a cancrinite cage with K, a gmelinite cage with Mg surrounded by H<sub>2</sub>O, and wide channels where Ca-H<sub>2</sub>O complexes can be found (Gualtieri et al, 1998; Passaglia et al, 1998; Armbruster and Gunter, 2001). The Mg/(Ca+Na) cation ratio is thought to be a reliable way to tell the difference between erionite and offretite with offretite ratios close to 1.0 and erionite ratios < 0.3 (Passaglia et al, 1998). Detailed structural studies have shown that Ca, which is more prevalent in erionite, is more flexible than Mg in charge balancing and can easily bond to framework O atoms and H<sub>2</sub>O in distorted and/or higher coordination arrangements (Gualtieri et al, 1998; Passaglia et al, 1998). In offretite, the smaller radius of Mg inhibits any bonding to framework oxygens, but larger structural openings in gmelinite cages are sufficient for octahedrally-coordinated Mg with disordered H<sub>2</sub>O along with Ca (used to balance the framework charge) to fit (Gualtieri et al, 1998, Passaglia et al, 1998). It has been proposed that samples with Mg > 0.80 in APFU should be considered offretite, while samples with Mg < 0.80 are erionite (Gualtieri et al, 1998; Dogan and Dogan, 2008; Dogan, 2011). While not directly considered by others, Mg would have a larger and more tightly bound hydration sphere than either Ca or Na. EPMA, TEM, and SCXRD data in this paper show that there can be erionite samples with higher Mg content than 0.80. Further information can be found in the results and discussion sections.

#### *Erionite and Offretite Optics*

Erionite and offretite are both framework silicate minerals with a 1:2, Si + Al : O ratio. Framework silicates typically have a low birefringence ( $\delta$ ) because the structures are similar in all directions (Dyar and Gunter, 2008); specifically for zeolite changes in optical properties – especially optical class and orientation – have been shown to be very sensitive to slight variations in composition or hydration (Ribbe and Gunter, 1993; Gunter et al, 1993; Gunter et

al, 1994; Palmer and Gunter, 2000). Since erionite and offretite are both hexagonal, they fall under the uniaxial optic class of minerals. These minerals have two main refractive indices represented by epsilon ( $\epsilon$ ) and omega ( $\omega$ ). Erionite was thought to be uniaxial (+), meaning  $\epsilon > \omega$  while offretite was thought to be uniaxial (-), meaning  $\omega > \epsilon$  (Sheppard and Gude; 1969; Gottardi and Galli, 1985, Deer et al, 2013). Since many of these zeolites have an elongate form, it is easy to determine the sign of elongation in order to determine whether or not the large ( $N$  = slow-ray) or small ( $n$  = fast-ray) refractive index value is parallel to the long axis of the grain (Bloss, 1999; Dyar and Gunter, 2008; Pourtabib and Gunter, 2015). This test is fairly straightforward, and it is easy to see differences in sign of elongation on larger grains, which are usually grains from basalt-hosted deposits. Note: the sign of elongation is different than the optic sign, but directly correlated for uniaxial minerals. More recent findings, including this study, suggest that both erionite and offretite can be length fast and length slow, and that this is related to the Si/Al ratio in the framework tetrahedral, where Al can be found in the six-member single rings of erionite and Al is found to be disordered over two different tetrahedral sites in offretite (Passaglia et al, 1998; Armbruster and Gunter, 2001; Neuhoff and Ribbe, 2006; Pourtabib and Gunter, 2015). It is thought that erionite can be distinguished from offretite based off of having a Si/Al ratio  $> 2.4$  (Wise and Tschernich, 1976; Rinaldi, 1976; Passaglia et al, 1998). Generally in zeolite minerals, the optical properties are sensitive to small changes in crystal structure and composition (Gunter and Ribbe, 1993).

Another factor when looking at variations in refractive index with changes in composition and structure of zeolites is the presence of  $H_2O$ . The orientation of the  $H_2O$  molecules will greatly affect the refractive index of the mineral. When the  $H_2O$  bonds become parallel to the plane of view, when looking under a microscope, the electron density will greatly increase along and perpendicular to the long axis of the grain (Gunter and Ribbe, 1993; Palmer and Gunter, 2000). Zeolite minerals are also sensitive to changes in temperature. Usually, when temperature increases, the refractive index will decrease, but some zeolites will reach a point where their internal structure collapses upon heating, and associated dehydration, which causes the refractive index to then increase (Gunter and Ribbe, 1993; Palmer and Gunter, 2000; Passaglia et al, 1998; Ballirano and Cametti, 2012).

Erionite and offretite, as well as other zeolites, are prone to internal cation migration. This has been seen in cation-exchange studies as well as studies on dehydration (Sherry,

1979; Gualtieri et al, 1998; Ballirano and Cametti, 2012; Ballirano and Cametti, 2015). Upon heating, the eight-membered ring in erionite will shrink, the six-membered ring between the cancrinite and erionite cage will expand, and the depletion of H<sub>2</sub>O molecule sites occur throughout the heating process (Ballirano and Cametti, 2012). Again, the long connecting channels in offretite allow for almost complete ion exchange from univalent cations to divalent cations (Sherry, 1979). Little is still known about the orientation of hydrogen atoms in the H<sub>2</sub>O structure of erionite and offretite upon dehydration. Orientation of H<sub>2</sub>O as well as knowing the types of bonds most prevalent in erionite and offretite (i.e. covalent, ionic) could greatly influence the polarization of the sample and thus change the refractive index (Gunter and Ribbe, 1993; Palmer and Gunter, 2000).

#### *Intergrowths, Overgrowths, and Stacking Sequences*

Additional difficulties encountered in identifying erionite and offretite are related to various intergrowths, overgrowths and stacking sequences often times found in these minerals (Kokotailo et al, 1972; Rinaldi, 1976; Wise and Tschernich, 1976; Passaglia et al, 1998). Typically erionite is characterized as having an AbAc stacking sequence, composed of alternating six-membered single (b and c) and double rings (A), while offretite has an AbAb stacking sequence. Erionite contains offretite-stacking faults that lead to a localized AbAb sequence, and offretite has erionite stacking faults leading to a localized AbAc sequence (Armbruster and Gunter, 2001). These stacking faults occur as a random distribution on the crystal as a whole, and can be observed parallel to c\* in diffraction as streaked spots (Kokotailo et al, 1972). This effect was not observed during the SAED TEM work on this study. Erionite and offretite can form as overgrowths on levyne or other zeolites such as chabazite, and can be found as intergrowths with one another (Rinaldi, 1976; Wise and Tschernich, 1976; Passaglia et al, 1998). According to Passaglia et al (1998), erionite is found to be most often overgrown on levyne, offretite is found to be more commonly overgrown on chabazite, and erionite and offretite intergrowths are not commonly found in large amounts. When erionite is found overgrown on levyne there is a noticeable change in chemistry to being more Al-rich. Also, erionite must develop a Si/Al ratio close to that of levyne in order to start the overgrowth process (Passaglia et al, 1998). In addition to intergrowth and overgrowth textures, some grains are also found to contain cores of varying composition. Rinaldi (1976)

noticed that in samples of offretite from Sasbach, Kaiserstuhl, Germany there was chemical zoning along the direction of crystal growth that reflected changes in composition from erionite to offretite. This transition in composition could be seen by looking at the differences in Si/Al ratios and the presence of more monovalent cations on the erionite side of the grain (Rinaldi, 1976). The formation of erionite over offretite and vice versa is due largely to chemistry and the availability of cations present in the starting solution. For instance, if Mg starts to crystallize initially then gmelinite cages will be the first structures to form, and this could lead to the formation of an offretite structure (Rinaldi, 1976). Overall, the structure, chemistry, optical properties and intergrowth/overgrowth textures of erionite and offretite are complex, and significant overlaps in these properties can further add confusion to their identification. It is again important that multiple analytical methods are used in order to differentiate between these minerals.

## **MATERIALS AND METHODS**

Erionite and offretite samples used in this study were basalt-hosted and have mostly elongate particle morphologies (Table 3.1). Zeolites from altered volcanic tuff-type deposits were not used due to small particle size, which would provide insufficient optic and EPMA data. Samples with associated optical data are designated by sample number and/or sample number with an 'a or b' attached to the name (i.e. sample 1 and sample 1a have optical data in addition to EPMA data). Samples labeled with the sample number and 'extra' are samples with no optical data but EPMA data (i.e. sample 1\_extra and 1\_extra\_1 have EPMA data but no optical data).

Problems encountered during the polishing phase of sample preparation were the primary reasons for why some samples with optic data had no EPMA data. Some polishing problems include; brittle grains that broke upon polishing, grains that were too fibrous to polish, grains that fully plucked out of the epoxy, grains that were not intersected during polishing, or grains that did not provide smooth enough polished surface for EPMA work. The following list of samples fell into the category of having optic data but no EPMA data, these include; 1, 1b, 2, 2a, 2b, 3b, 4a, 4b, 5b, 6b, 7a, 8a, 8b, 9a, 9b, 10b, 11, 11b, 13b, 16, 16a, 16b, 17, 17a, 19, 20a, 21, 21a, 22, 22a, 22b, 23, 23a, 24a, 25, 25b, 27, 28, 28a, 28b, 29b, 31a,

32, 35, 35a and 35b. In addition, certain grains were also omitted from the final results due to providing inadequate EPMA data, these grains include; 6a, 6\_extra, 6\_extra\_1, 11\_extra\_1, 17\_extra\_2, 21\_extra\_1, 28\_extra\_1, 28\_extra\_2, 36\_extra, 37\_extra, 37\_extra\_1, 38\_extra, 38\_extra\_1 and 41\_extra. Criterion for inadequate EPMA data for this study are as follows; grain is too small for the diameter of the electron beam (10  $\mu\text{m}$ ), grain has an irregular surface, Si+Al:O ratio is incorrect for APFU calculations, or the balance error percent (E%) is  $> \pm 10$ .

The Natural History Museum of Los Angeles County, Philip Neuhoff, obtained from Shannon & Sons Minerals, and MEG provided samples for this study. All of the preliminary sample names used were taken directly from the sample labels already provided. Sample #34 was labeled as offretite, but EPMA data shows a composition more similar to that of apatite. SCXRD data and TEM data for sample #34 proved difficult, so no structural data was obtained, however this sample was omitted from the study. Any additional revised sample names will be discussed later in the paper. EPMA data for other fibrous/acicular zeolites can be found in the Appendix C.

### **Instrumentation**

EPMA was performed at Washington State University's GeoAnalytical Lab on a JEOL JXA-8500F. TEM analyses were done at The University of Idaho on a JEOL JEM-2010 using a Thermo Scientific detector coupled with NSS software. Preliminary PLM analysis for checking sample polish was done on an Olympus BH-2 microscope and sample images after EPMA work were taken on an Olympus DP-70. A Leica EZ4HD stereoscope was also used for sample preparation. SCXRD analyses were also carried out at The University of Idaho on a Siemens SMART single-crystal x-ray diffractometer with APEX 3 software and a 0.71  $\text{\AA}$  Mo x-ray source.



## Sample Preparation

### *EPMA*

Glass petrographic microscope slides were first frosted using 320 grit silicon carbide polishing paper, and excess grit was removed using ethanol and compressed air. One laser-cut acrylic disk (1" diameter, ¼" height, with three 1cm diameter holes drilled into it) is then adhered to the frosted side of the glass slide using a 5:1 epoxy resin to hardener (slow) mixture. The slide is then allowed to cool and harden at room temperature for 24 hours. Next, individual grains used for optical analysis are removed from their glass fiber using acetone (grains were held to a glass fiber using nail polish for spindle stage analysis). The grain with the best optical data is placed into one of the laser cut holes in the acrylic disk, the next two grains with associated optic data are placed in the next laser cut hole, and the final laser cut hole is filled with 5 or more grains (no optic data on these grains) from the same sample location. The same epoxy resin + hardener mixture is made and poured equally into each individual laser cut hole. This entire set-up is then periodically heated on the low-heat setting of a hot plate and cooled on a counter-top to try and eliminate excess bubbles. It is important to try and eliminate bubbles that are next to grains. The sample is then allowed to cool for 24 hours. Once sample is cooled, it is cut on a Hillquist thin-section machine to a few mm in thickness. Sample is then polished first using 320 grit silicon carbide papers and subsequently polished using a series of 15, 6, and 3 µm diamond polishing papers. Next, the samples are polished further using a set of 5, 3.5, 2.5, 1.5, 1, 0.5, and 0.25 µm diamond-polishing pastes. It is important to make sure the samples are thoroughly washed using mild soap and water between changing polishing papers/pastes in order to avoid contamination. The sample polish is continually checked under reflected light. Finished samples were then carbon-coated at the WSU GeoAnalytical Lab and ready for analysis.

### *TEM and SCXRD*

Samples used for TEM and SCXRD analysis were first visually inspected using a stereoscope, and individual erionite/offretite grains were plucked from the original basalt-hosted sample and placed into a petri dish. For TEM, zeolite grains were lightly crushed using a bit of isopropanol alcohol and a mortar and pestle, then the mixture was pipetted directly

onto a carbon-coated copper TEM grid. The sample was allowed to dry and grain distribution was checked using a PLM before analysis. For SCXRD analysis, an individual grain was attached to a glass fiber mounted into a brass pin using nail polish. The grain is attached so that its long axis is parallel to the long axis of the glass fiber. It is important to try and mount a grain that has no visible twinning. The grain is then placed into a SCXRD goniometer, and particle morphology and sign of elongation is checked on a spindle stage microscope set-up. If the grain is usable then it is ready for SCXRD analysis.

## **Methods**

### *EPMA*

For EPMA analysis a 15 kV accelerating voltage was used, 8 nA beam current, and 10  $\mu\text{m}$  beam size. Relatively low and diffuse beam parameters were used due to very small grain sizes and the presence of  $\text{H}_2\text{O}$  in the zeolite chemistries, also to minimize Na being volatilized. Mean atomic number background corrections were made using the Kramer's Rule Method, and corrections for elemental migration due to beam damage were also applied (Donovan and Tingle, 1996; Nielsen and Sigurdsson, 1981). The Armstrong-Love/Scot phi-rho-z method was used for ZAF matrix corrections, and counting times were acquired on multiple spectrometers and aggregated (Armstrong, 1988). Elements analyzed, counting times, analyzing crystals and calibration standard information can be found in Table 3.2. Grain cracks, edges, and other surficial imperfections were avoided when possible while picking individual points. EPMA results are presented as weight % oxides with  $\text{H}_2\text{O}$  content being calculated by difference using the ZAF corrections. Atoms per formula unit (APFU) were calculated later based off of methods used by Dyar and Gunter (2008). For each point analyzed a E% calculation was done in order to look at the relationship between exchangeable cations and Al and  $\text{Fe}^{3+}$  ( $100 \times [(\text{Al}+\text{Fe})_{\text{ob}} - \text{Al}_{\text{th}}]/\text{Al}_{\text{th}}$ ;  $\text{Al}_{\text{th}} = \text{Na} + \text{K} + 2 \times (\text{Ca} + \text{Mg} + \text{Sr} + \text{Ba})$ ). Positive E% are meant to indicate an excess of trivalent cations and a negative E% will indicate excess amounts of exchangeable cations (Passaglia, 1970; Passaglia et al, 1998). All statistical analysis was performed using the JMP 13 statistical analysis software.

### *TEM and SCXRD*

For SAED, samples were run at an accelerating voltage of 200 kV and a thallium chloride diffraction standard was used. Diffraction patterns for erionite and offretite can be differentiated due to the unique space group symmetry of erionite,  $P6_3/mmc$  and noting diffraction constraints along  $c^*$ . Diffraction patterns were indexed for erionite and offretite grains using CrystalMaker and SingleCrystal software with simulated crystal structure patterns found using the American Mineralogists Crystal Structure Database. Acquired zone axis diffraction patterns were uploaded into the SingleCrystal software and matched to previously determined crystal structure data of erionite and offretite (Figure 3.1: Pourtabib and Gunter, 2015).

For SCXRD methods, the same parameters were used for the data collection of both erionite and offretite. For unit cell determinations the spot threshold was reduced so that lower intensity diffractions spots could be included in the data collection. This is important because higher order reflections in erionite are very weak, so if the threshold is too high then the unit cells will not match for erionite. Also, the space group of erionite and offretite share many similarities, so the more diffraction spots acquired, the easier it will be to differentiate between the two minerals. For the purpose of this study only preliminary unit cell determinations were made using SCXRD, later studies will focus more on longer data acquisition times and making crystal structure refinements.

## **RESULTS**

Erionite and offretite analyses were compared on a variety of scales such as, point-by-point comparison of changes in composition along a single grain transect, as well as overall averaged chemical compositions for each grain. In addition to composition, information on previous optical work was also used to find correlations between changes in chemistry and optics in each sample. Any changes in the original sample name after identification by EPMA, TEM, and SCXRD can be found on Table 3.3.

### *EPMA*

Erionite and offretite EPMA results on Tables 3.4 and 3.5 are taken as an average of all points per grain. Initial EPMA results are reported as weight % oxides and later calculated into APFUs. Number of points per grain, R-value, balance error %, unit cell dimensions, and sign of elongation are also reported for each averaged sample. Grains that did not exhibit clear elongation are listed as “–“ for sign of elongation. Mg values in red represent APFU values >0.80 (Gualtieri et al, 1998; Dogan and Dogan, 2008, Dogan, 2011). Additional EPMA data for other fibrous/acicular zeolites can be found in Appendix B.

#### *Single-grain-scale: erionite*

Erionite grains that exhibit both length fast and length slow signs of elongation (Figure 3.2 and 3.3), as well as grains that are completely length fast and completely length slow are compared on a point-by-point basis to find trends at the single-grain-scale. Erionite grains that are both length fast and length slow generally decrease in Mg content and increase in Ca content when moving from the length slow base to the length fast tip. Looking at erionite sample 45\_extra in more detail, by plotting the major cations (APFU) on a ternary diagram along with the signs of elongation for each point along the grain, it is apparent that the overall chemical variability along the grain is subtle. The majority of length slow grains appear to have a higher Mg content compared to the length fast grains, and the majority of length fast grains appear to have a slightly higher Ca (+Na) content. There is too much overlap with the K (+Sr +Ba) endmember to discriminate between the length fast and length slow points (Figure 3.4). Further scatter diagram analyses of the individual points from sample 45\_extra, again confirm these same relationships, showing that in the length slow portion of the grain, the Mg content is high, while the Ca content is low (Figure 3.5). While in the length fast portion of the grain the Mg content is low while the Ca content is high. These trends, as well as the positive and negative line of best-fit slopes correlate to the same changes in composition while moving from the base to the tip of sample 45\_extra. This graph also shows that the R-value does not vary significantly from length fast to length slow portion.

Next, erionite grains that are completely length slow (Figure 3.6) and completely length fast (Figure 3.7) are compared on a point-by-point basis. In grains that are not splayed, it is difficult to tell which end is the base and which end is the tip of the grain, so general relationships are used instead. In sample 11\_11a of a completely length slow erionite as Mg

increases, Ca will decrease, and in sample 14\_14b of a completely length fast erionite, again as Mg increases, Ca will decrease. Sample 12\_12a of erionite shows an overgrowth texture where there is a defined grain core (Figure 3.8). When taking a closer look at changes in composition along this grain again, as Mg increases, Ca will decrease. On this grain there is no obvious difference in composition in the overgrowth core, except that this is where Mg content is lowest and Ca content is highest.

*Single-grain-scale: offretite*

The changes in composition of offretite along a single grain are less clear than the relationships found in the erionite samples. Sample 32\_32b of offretite shows a grain with a defined intergrowth texture where one half of the grain is length fast and one half is length slow (Figure 3.9). Looking closely at the compositional changes on the length slow portion of the grain, as Mg increases, K also increases and there is no definite trend in Ca. On the length fast portion of the same grain, as Mg and K increase, Ca decreases. When looking at sample 7\_7b of a completely length fast offretite, Mg and K generally decrease from base to tip while Ca will increase from base to tip (Figure 3.10). Finally, looking at a completely length slow offretite sample, as K and Mg increase, Ca will decrease (Figure 3.11).

*Whole-grain-scale: erionite and offretite*

Trends in composition and optics of erionite and offretite grains are compared next on a whole-grain-scale. First, multivariate analyses on parameters such as refractive index, and chemistry of each sample are used to determine the strength of one variables affect on another. The Pearson product-moment correlation coefficient measures the strength of the relationship between variables. In this case, high correlation ( $>0.80$ ), moderate correlation ( $0.5-0.8$ ) and low correlation ( $<0.5$ ) parameters are used. It is important to note that outliers heavily influence correlation coefficient trends, so this analysis is only used as a preliminary means to point out strong correlations in the data. The correlation coefficient matrix of erionite and offretite show all points with EPMA data for each grain used in this study, and any misidentified samples moved to their respective graph. Variables with strong correlations in the erionite matrix are N (slow)/n (fast), Si/Al, Si/Ca and Al/Ca (Figure 3.12). This shows

that for erionite, the point-by-point relationships discussed previously show clear trends, but when looking at the entire dataset, the correlations only partially reflect the individual grain scale. Conversely, variables in the offretite correlation coefficient matrix have strong correlation between N (slow)/n (fast), Si/Al, Si/Fe, Si/Mg, Al/Fe, Al/Mg and Sr/Na (Figure 3.13). This shows that at a point-by-point scale, the correlation between chemistry in offretite is not always distinct, but when looking at all of the grains, there is a strong relationship between some of the variables.

Trends between major cations and signs of elongation for each averaged grain APFU are plotted on a ternary diagram. Generally, offretite has a higher Mg content and lower K (+Sr +Ba) and Ca (+Na) content, while erionite has a lower Mg content, and higher K (+Sr +Ba) and Ca (+Na) content (Figure 3.14). These relationships are in agreement with the general chemical formulas for each mineral (Armbruster and Gunter, 2001). The only outliers in the data are offretite samples 29 and 29a (circled in orange) which are labeled as offretite overgrown on levyne, and erionite samples 9, 13a, and 14b which were structurally found to be offretite (all sample symbols were changed to reflect a correct identification). Next, in observing the APFU values of each point from all the grains in this study, the major cations of erionite and offretite and the R-values are compared using a scatter diagram (Figure 3.15). Again, this graph confirms that erionite commonly has a higher Ca content while offretite has a higher Mg content. Inherently, erionite has more Si than offretite, which gives it a higher R-value; hence the distinctive blue line separating the R-values of both minerals. Offretites with low Mg and low R-values (yellow circles) are associated with levyne, while offretites with low R-values and high Ca (samples 29, 29a, orange circle) are mislabeled offretites that are actually erionites. Finally, samples with a purple circle are mislabeled erionite that are actually offretites (samples 9, 13a, 14b), and these samples have inconclusive SCXRD identifications that will again be discussed in the results section (Passaglia et al, 1998). Figure 3.16 shows the same relationship between R-value with respect to erionite and offretite but also shows that K content. Erionites generally have a higher K content than offretite based off of APFU calculations, and the data outliers are consistent with the mislabeled samples discussed above.

*Whole-grain-scale: erionite and offretite optics and chemistry*

When looking at diagrams which compare the  $N$  (slow)/ $n$  (fast) refractive index values vs.  $R$ -values (averaged points per grain using APFUs) from this study, it is clear that changes in the  $R$ -value have a direct effect on changes in refractive index, as they in-turn effect the amount and type of extraframework cations and  $H_2O$ . This point is illustrated using a scatter diagram with shaded confidence intervals, which describe the uncertainty associated with the data, and this is used to generate a line of best fit. For both erionite and offretite, the refractive index values for both  $N$  (slow) and  $n$  (fast) overlap greatly, but generally erionite will have a higher  $R$ -value because of having more Si (Figure 3.17). Erionite is found to be both optically positive ( $\epsilon > \omega$ ,  $n$  (fast)  $>$   $N$  (slow), length slow) and optically negative ( $\omega > \epsilon$ ,  $N$  (slow)  $>$   $n$  (fast), length fast), with the optically positive erionites having more a higher  $R$ -value and optically negative erionites having a lower  $R$ -value. It is important to note that the optically negative erionites were found to be samples 12a, 12b, 13a, 14, and 14b, all of which are samples that have caused problems with other means of identification. Once more, further detail will be discussed in the discussion section. For the offretites, the optically positive samples again tend to have higher  $R$ -values and the intermediate (optically positive and negative) and optically negative samples tend to have lower  $R$ -values. Optically positive offretite samples are 30a, and 30b, all of which show very low retardations when the accessory plate is inserted. Again, these interpretations will be discussed in detail below.

When comparing refractive index and  $R$ -values for both erionite and offretite samples together, it is clear where the crossover between optically positive and optically negative grains falls, around 0.73  $R$ -value, sample outliers are 3, 30b, 12, 12a, and 12b (Figure 3.18 A). When comparing refractive index to the Mg/Ca ratio for both erionite and offretite, erionite again has a higher Ca value while offretite has a higher Mg value (Figure 3.18 B). When observing this relationship, the crossover between optically positive and optically negative grains is unclear. Finally, observing the last set of graphs, length slow grains of erionite tend to have a moderate Ca content with a range of Mg contents, while length fast grains of erionite have higher Ca contents and lower Mg contents (Figure 3.19 A). The averaged whole-grain offretite samples typically have a high Mg content and low Ca content and the data points are more clustered than the data for the erionite samples (Figure 3.19 B).

## DISCUSSION

Generally, when looking at compositional changes along an erionite grain, Mg will share an inverse relationship with Ca. For erionite, the length slow grains tend to have higher amounts of Mg and lower amounts of Ca, while the relationship for length fast erionites is the opposite. This is most likely related to the movement of cations and removal of H<sub>2</sub>O upon grain dehydration. Since H<sub>2</sub>O was not measured directly in this study but is directly related to changes in refractive index and migration of cations, it is assumed that H<sub>2</sub>O values will vary along a grain. Interpretations of the data will factor in cation migration upon sample dehydration. Usually, if an erionite grain is both length fast and length slow, the length fast portion is at the tip. As stated previously, when erionite is dehydrated, the expansion of the link between the K-filled cancrinite cage and the Ca, Na, and Mg-filled erionite cage allows for these cations to migrate freely. Since, the H<sub>2</sub>O sites surround the Ca cations, and the H<sub>2</sub>O depletes when dehydrated, the Ca could bump other cations out of the erionite cage, taking their place, hence the increase in Ca when erionite is length fast (Sherry, 1979; Gualtieri et al, 1998; Ballirano and Cametti, 2012; Ballirano and Cametti, 2015). Another factor that could contribute to having a length fast erionite is an increase in H<sub>2</sub>O within the ring structures causing higher polarizability within the plane and therefore, an increase in the omega refractive index, resulting in a change in optic sign (Palmer and Gunter, 2000).

For offretite samples, the general trends in composition are not as well defined as in erionite, but some relationships can be seen. Overall, in grains of offretite that are both length fast and length slow Mg and Ca are inversely related. In length fast offretite grains Mg is generally higher than Ca, and in length slow offretite grains Ca is generally higher than Mg. As stated before, when offretite undergoes dehydration, the long connecting channels allow for free movement of cations, specifically Mg and Ca, which are both surrounded by H<sub>2</sub>O (Sherry, 1979; Gualtieri et al, 1998; Ballirano and Cametti, 2015). The reasoning behind possible changes in Mg and Ca upon dehydration might be due to preferential movement in order to balance charge offsets created by changes in H<sub>2</sub>O. It is important to note that grains of offretite with both length fast and length slow portions appear to be divided following trends in surface features such as cracks. For both erionite and offretite samples, there were few trends in K along a grain transect. This may be due to the fact that K is fixed in the



cancrinite cage and will not easily exchange with neighboring monovalent cations in the erionite cage unless large amounts of dehydration have taken place (Neuhoff and Ruhl, 2006). Another cation that was not as significant in this study was Na. The EPMA results of Na were below detection limits, due to the fast migration of Na away from the electron beam during EPMA analysis, so Na was not a factor in comparing the compositional data. Based on these subtle structural changes it is unconvincing to believe that both erionite and offretite are present on the grains that are both length fast and length slow. Perhaps there are a few cases where this is possible such as sample 33, but it was not evident in the samples from this study.

There were a few samples throughout the study that kept showing up as outliers during data analysis, and these samples were 12, 13, and 14. Compositionally all of these samples plot more similar to offretite when looking at the R-value, and samples 13 and 14, which come from the same deposit, also have a high Mg content like that of offretite. Upon further investigation using SAED, these two samples matched strongly with offretite, while no erionite diffraction pattern could be found. Due to the similar hand sample appearance of both erionite and offretite these samples were most likely mislabeled. Although sample 12 has an R-value more similar to that of offretite, it has a low Mg and high Ca content more similar to that of erionite. Analysis by SAED showed diffraction patterns matching both that of erionite and offretite for sample 12, so this sample could potentially be an intergrowth of erionite and offretite. Samples 12, 13, and 14 were also the only erionite samples to be optically negative. Since samples 13 and 14 are actually offretite, sample 12 may instead be the only entirely length fast erionite in this study. When looking at offretite, sample 30 was the only sample to be optically positive. This sample was proven to be offretite through SAED analysis, and is possibly the only entirely length slow offretite in this study. For both erionite and offretite the R-value largely controls the refractive index.

Sample 33 of offretite from Sasbach, Kaiserstuhl, Germany is another outlier with a Mg/Ca ratio similar to the other offretite samples but this sample has a range of R-values. This sample contained grains that were both length fast and length slow and had distinctive overgrowth textures. Rinaldi (1976) did a detailed study of grains from this location and attributed this variation in sign of elongation on a single grain to be an intergrowth between erionite and offretite. When analyzing sample 33 by SAED the diffraction patterns spacings were that of offretite but the 2<sup>nd</sup> order spots along  $c^*$  were slightly offset, almost as if it was a

disordered erionite and offretite pattern. Compositionally, there was not enough data on these samples to definitively say if the grain represents a transition from erionite to offretite, so more work needs to be done.

When taking another look at the composition of the erionite samples many of the grains have Mg contents that exceed 0.80. Samples that exceeded this 0.80 Mg amount were previously disregarded and thrown out as not being erionite (Gualtieri et al, 1998; Dogan and Dogan, 2008; Dogan, 2011). Grains 2 extra\_1 (1.41 Mg), 3\_extra (0.87 Mg), 9 (1.28 Mg), 10 (1.11 Mg), 11a (1.11 Mg), 13a (2.03 Mg), and 14b (2.18 Mg) have Mg amounts higher than 0.80. Additional identification by SAED and SCXRD shows that samples 2, 3, 9, and 10 all have positive erionite or erionite/offretite identifications. While samples 13 and 14 were identified as offretite and sample 11 has no SCXRD data. This shows that there can be erionite samples that contain higher abundances of Mg while still retaining the unit cell dimensions of erionite. Since Ca and Mg are both divalent cations that can be found in the erionite cages of erionite, it seems reasonable to suggest that more Mg can replace Ca in these structures. Finally, for both erionite and offretite, the R-value was distinctive for both erionite and offretite (i.e. higher R-value in erionite), but the R-value varies independently of the extraframework cation content due to changes in environments of formation conditions (Neuhoff and Ruhl, 2006).

## **FUTURE WORK**

Future work on erionite and offretite will be focused on obtaining more detailed structural, chemical and optical observations of these minerals, in order to solidify trends in the data. Crystal structure refinements will be done on SCXRD in order to better constrain the locations and bond distances of atoms, especially in erionite samples with high Mg contents. More detailed work will be done on samples that exhibit both length fast and length slow grains (i.e. sample location #1, Ajo erionite) so as to determine the major factor controlling this transition. More work will also be done to better quantify the amount of H<sub>2</sub>O and to look at the orientation of the H<sub>2</sub>O molecules in erionite and offretite in order to relate this with dehydration and refractive index values.

## ACKNOWLEDGEMENTS

I would like to thank the Natural History Museum of Los Angeles County for providing the majority of the zeolite sample used in this study, Philip Neuhoff, obtained from Shannon & Sons Minerals, and Mickey E. Gunter for also providing outstanding zeolite samples. I would also like to thank Cody Steven at the University of Idaho for handling all of the SCXRD analysis. Finally, I would like to thank Owen Neill at Washington State University GeoAnalytical Lab for making the EPMA analysis go so smoothly, and Tom Williams at the University of Idaho for helping with TEM analysis.

**REFERENCES CITED**

- Armbruster, T., and Gunter, M. E. (2001) Crystal structures of natural zeolites. *Reviews in mineralogy and geochemistry*, 45(1), 1-67.
- Armstrong, J. T. (1988) Quantitative analysis of silicate and oxide minerals: comparison of Monte Carlo, ZAF and phi-rho-z procedures. *Microbeam analysis*, 23, 239-246.
- Ballirano, P., and Cametti, G. (2012) Dehydration dynamics and thermal stability of erionite-K: Experimental evidence of the “internal ionic exchange” mechanism. *Microporous and Mesoporous Materials*, 163, 160-168.
- Ballirano, P., and Cametti, G. (2015) Minerals in the human body. Crystal chemical and structural modifications of erionite fibers leached with simulated lung fluids. *American mineralogist*, 100(4), 1003-1012.
- Ballirano, P., Pacella, A., Cremisini, C., Nardi, E., Fantauzzi, M., Atzei, D., Rossi, A., and Cametti, G. (2015) Fe (II) segregation at a specific crystallographic site of fibrous erionite: A first step toward the understanding of the mechanisms inducing its carcinogenicity. *Microporous and mesoporous materials*, 211, 49-63.
- Bloss, F. D. (1999) *Optical Crystallography*, Mineralogical Society of America, 5, 119-121.
- Deer, W.A., Howie, R.A., and Zussman J. (2013) *Rock Forming Minerals: Volume Four: Framework Silicates*, Longmans, 355-362.
- Dogan, M. (2011) Quantitative characterization of the mesothelioma- inducing erionite series minerals by transmission electron microscopy and energy dispersive spectroscopy. *Scanning*, 34(1), 37-42.
- Dogan, A. U., Baris, Y. I., Dogan, M., Emri, S., Steele, I., Elmishad, A. G., and Carbone, M. (2006) Genetic predisposition to fiber carcinogenesis causes a mesothelioma epidemic in Turkey. *Cancer Research*, 66(10), 5063-5068.
- Dogan, A. U., Dogan, M., and Hoskins, J. A. (2008) Erionite series minerals: Mineralogical and carcinogenic properties. *Environmental Geochemistry and Health*, 30(4), 367-381.
- Dogan, A. U., and Dogan, M. (2008) Re-evaluation and re-classification of erionite series minerals. *Environmental Geochemistry and Health*, 30(4), 355-366.
- Donovan, J. J., and Tingle, T. N. (1996) An improved mean atomic number background correction for quantitative microanalysis. *Microscopy and Microanalysis*, 2(01), 1-7.
- Dyar, M. D., and Gunter, M.E. (2008) *Mineralogy and Optical Mineralogy*, Mineralogical Society of America, Chantilly, VA, 708.

Gottardi, G., and Galli, E. (1985) *Natural Zeolites*. Springer-Verlag, Berlin, 18, 409 pp.

Gualtieri, A., Artioli, G., Passaglia, E., Bigi, S., Viani, A., and Hanson, J. C. (1998) Crystal structure-crystal chemistry relationships in the zeolites erionite and offretite. *American Mineralogist*, 83(5-6), 590-606.

Gunter, M. E., and Ribbe, P. H. (1993) Natrolite group zeolites: Correlations of optical properties and crystal chemistry. *Zeolites*, 13(6), 435-440.

IARC: International Agency for Research on Cancer (1987a) IARC Monographs on the Evaluation of Carcinogenic Risks to Humans, Silica and Some Silicates, Lyon, France, 42, 289.

IARC: International Agency for Research on Cancer (1987b) IARC Monographs on the Evaluation of Carcinogenic Risks to Humans, Overall Evaluations of Carcinogenicity, Lyon, France, Supplement 7, 440.

Kokotailo, G. T., Lawton, S., and Sawruk, S. (1972) Direct Observation of Stacking-Faults in Zeolite Erionite. *American Mineralogist*, 57(3-4), 439.

Matassa, R., Familiari, G., Relucenti, M., Battaglione, E., Downing, C., Pacella, A., Cametti, G., and Ballirano, P. (2015) A deep look into erionite fibres: An electron microscopy investigation of their self-assembly. *Scientific reports*, 5.

Mattioli, M., Giordani, M., Dogan, M., Cangiotti, M., Avella, G., Giorgi, R., Dogan, U.A., and Ottaviani, M. F. (2016) Morpho-chemical characterization and surface properties of carcinogenic zeolite fibers. *Journal of hazardous materials*, 306, 140-148.

Neuhoff, P. S., and Ruhl, L. S. (2006) Mechanisms and geochemical significance of Si–Al substitution in zeolite solid solutions. *Chemical Geology*, 225(3), 373-387.

Nielsen, C. B. H., and Sigurdsson, H. (1981) Quantitative methods for electron microprobe analysis of sodium in natural and synthetic glasses. *American Mineralogist*, 66, 547-552.

Oczypok, E. A., Sanchez, M. S., Van Orden, D. R., Berry, G. J., Pourtabib, K., Gunter, M. E., Roggli, V.L., Kraynie, A.M., and Oury, T. D. (2016) Case Report Erionite-associated malignant pleural mesothelioma in Mexico. *Int. J. Clin. Exp. Pathol*, 9(5), 5722-5732.

Palmer, D. (2015) *CrystalMaker and SingleCrystal: Interactive crystallography for the Macintosh*. CrystalMaker Software, Oxfordshire, UK, [www.crystallmaker.com](http://www.crystallmaker.com).

Palmer, J. L., and Gunter, M. E. (2000) Optical properties of natural and cation-exchanged heulandite group zeolites. *American Mineralogist*, 85(1), 225-230.

Passaglia, E. (1970) Crystal chemistry of chabazites. *American Mineralogist* 55.7-8, 1278-1301.

- Passaglia, E., Artioli, G., and Gualtieri, A. (1998) Crystal chemistry of the zeolites erionite and offretite, *American Mineralogist* 83, 577-589.
- Pourtabib, K.P., and Gunter, M.E. (2015) Analytical approach for identification of the zeolite erionite, *The Microscope* 63(4), 175-185.
- Rinaldi, R. (1976) Crystal chemistry and structural epitaxy of offretite-erionite from Sasbach, Kaiserstuhl. *N Jahrb Mineral Mh*, 1976, 145-156.
- Saini-Eidukat, B., and Triplett, J. W. (2014) Erionite and offretite from the Killdeer Mountains, Dunn County, North Dakota, USA. *American Mineralogist*, 99(1), 8-15.
- Sheppard, R. S. (1996) Occurrences of erionite in sedimentary rocks of the western United States (No. 96-18). US Geological Survey.
- Sheppard, R. A., and Gude, A. J. (1969) Chemical composition and physical properties of related zeolites offretite and erionite. *American Mineralogist*, 54(5-6), 875.
- Sherry, H. S. (1979) Ion-exchange properties of the natural zeolite erionite. *Clays and Clay Minerals*, 27(3), 231.
- Van Gosen, B. S., Blitz, T. A., Plumlee, G. S., Meeker, G. P., and Pierson, M. P. (2013) Geologic occurrences of erionite in the United States: an emerging national public health concern for respiratory disease. *Environmental geochemistry and health*, 35(4), 419-430.
- Wise, W. S., and Tschernich, R. W. (1976) The chemical compositions and origin of the zeolites offretite, erionite, and levyne. *American Mineralogist*, 61(9-10), 853-863.

Table 3.1

| Sample Number | Sample Location  | Primary Zeolites                      |
|---------------|--|---------------------------------------|
| 1 and 45      | Phelps Dodge Co. Well No. 1, Little Ajo Mtns, Ajo District, Pima County, AZ, USA | erionite (Ca)                         |
| 2             | Bozarth Mesa near Hillside, Yavapai County, AZ, USA                              | erionite (K)                          |
| 3             | Phelps Dodge Co. Well No. 1, Little Ajo Mtns, Ajo District, Pima County, AZ, USA | erionite (K)                          |
| 4             | Thumb Butte, Graham County, AZ, USA  | erionite (K)                          |
| 5             | Spray, Oregon, USA   | levyne with epitaxial offretite       |
| 6             | Clifton, AZ, USA   | offretite                             |
| 7             | Adamello, Italy  | offretite, chabazite                  |
| 8             | Rock Island Dam, Washington, USA   | erionite, clinoptilolite, phillipsite |
| 9             | Chase Creek, Falkland, Kamloops Mining Division, B.C., Canada                    | erionite                              |
| 10            | Chase Creek, Falkland, Kamloops Mining Division, B.C., Canada                    | erionite                              |
| 11            | Clifton, Greenlee Co, AZ, USA  | erionite                              |
| 12            | Eureka Valley, Del Norte Co, California, USA                                     | erionite                              |
| 13            | Herbstein, Vogelsberg, Germany   | erionite                              |
| 14            | Herbstein, Vogelsberg, Hesse, Germany  | erionite                              |
| 15            | Rock Island Dam, Douglas Co, Washington, USA                                     | erionite, heulandite                  |
| 16            | Malpais Hill, Didleyville, Pinal Co, AZ, USA                                     | erionite                              |
| 17            | Chase Creek, B.C., Canada  | erionite                              |
| 18            | Pinans Lake, Westworld, B.C., Canada   | erionite                              |
| 28            | Rock Island Dam, Douglas Co, Washington, USA                                     | offretite, erionite                   |
| 29            | Douglas Creek Road, Westworld, B.C., Canada                                      | offretite, levyne                     |
| 30            | Mont Semiol, Chatelneuf, Loire, Rhone Alpes, France                              | offretite                             |
| 31            | Mt. Simiouse, Loire, France  | offretite                             |
| 32            | Mt. Simiouse Semiol, Chatelneuf, Loire, Rhone Alpes, France                      | offretite, phillipsite                |
| 33            | Sasbach am Kaiserstuhl, Germany  | offretite                             |
| 34            | Yuma Co, AZ, USA   | offretite                             |
| 43            | Yaquina Head, Agate Beach, Oregon, USA   | erionite                              |

Sample numbers and locations of erionites and offretites used in this study.

Table 3.2

| Element                        | Peak Counting Time (s) | Low Background Counting Time (s) | High Background Counting Time (s) | Spectrometer # | Analyzing Crystal | Calibration Standard             |
|--------------------------------|------------------------|----------------------------------|-----------------------------------|----------------|-------------------|----------------------------------|
| SiO <sub>2</sub> *             | 10                     | MAN                              | MAN                               | 5              | TAP               | K-412 NIST Glass                 |
| Al <sub>2</sub> O <sub>3</sub> | 10                     | MAN                              | MAN                               | 5              | TAP               | K-412 NIST Glass                 |
| Fe <sub>2</sub> O <sub>3</sub> | 30                     | 15                               | 15                                | 3              | LIFH              | Hematite #2 (C.M. Taylor)        |
| MgO**                          | 200                    | 100                              | 100                               | 1, 5           | TAP               | Diopside #1 (C.M. Taylor)        |
| CaO                            | 20                     | 10                               | 10                                | 4              | PETJ              | Wollastonite, Wards              |
| SrO                            | 120                    | 60                               | 60                                | 2              | PETJ              | SrTiO <sub>3</sub> (C.M. Taylor) |
| BaO**                          | 130                    | 65                               | 65                                | 3, 4           | LIFH, PETJ        | Barite #4 (C.M. Taylor)          |
| Na <sub>2</sub> O*             | 10                     | 5                                | 5                                 | 1              | TAP               | Albite, Tiburon                  |
| K <sub>2</sub> O*              | 20                     | 10                               | 10                                | 4              | PETJ              | Orthoclase, OR-1 (Ingamells)     |

EPMA parameters used in this study.



Table 3.3

| Sample Number | Museum Name                               | TEM Results | SCXRD Results | a / b (Å) | C (Å)  | V (Å <sup>3</sup> ) | Sign of Elongation |
|---------------|---|-------------|---------------|-----------|--------|---------------------|--------------------|
| 1             | erionite-Ca                               | ERI/OFF     | ERI           | 13.31     | 15.15  | 2325                | LS/LF              |
| 2             | erionite-K                                | ERI         | ERI           | 12.84     | 14.66  | 2091                | LS                 |
| 3             | erionite-K                                | ERI         | ERI           | 13.31     | 15.14  | 2325                | LS/LF              |
| 4             | erionite-K                                | ERI         | ERI           | 13.26     | 15.06  | 2295                | LS                 |
| 5             | levyne, epitaxial offretite               | LEV         | NA            | -         | -      | -                   | -                  |
| 7             | chabazite with offretite                  | OFF         | OFF           | 13.3142   | 7.5925 | 1165.6              | LF                 |
| 8             | clinoptilolite, erionite, and phillipsite | -           |               |           |        |                     | -                  |
| 9             | erionite                                  | OFF         | ERI/OFF?      | 13.39     | 15.22  | 2362                | LS/LF              |
| 10            | erionite                                  | ERI/OFF     | ERI/OFF?      | 13.29     | 15.12  | 2313                | LS                 |
| 11            | erionite                                  | -           |               |           |        |                     | LS                 |
| 12            | erionite                                  | ERI/OFF     |               |           |        |                     | LF                 |
| 13            | erionite                                  | OFF         |               |           |        |                     | LF                 |
| 14            | erionite                                  | OFF         |               |           |        |                     | LF                 |
| 15            | erionite                                  | ERI         | ERI           | 13.326    | 15.153 | 2330                | LS                 |
| 16            | erionite                                  | ERI/OFF     |               |           |        |                     | LS                 |
| 17            | erionite                                  | -           |               |           |        |                     | LS                 |
| 18            | erionite                                  | ERI         |               |           |        |                     | LS                 |
| 28            | offretite and erionite                    | ERI         |               |           |        |                     | -                  |
| 29            | offretite and levyne                      | ERI         |               |           |        |                     | LF                 |
| 30            | offretite                                 | OFF         |               |           |        |                     | LS                 |
| 31            | offretite                                 | -           |               |           |        |                     | LS/LF              |
| 32            | offretite                                 | OFF         |               |           |        |                     | LS/LF              |
| 33            | offretite                                 | OFF?        |               |           |        |                     | LS/LF              |
| 43            | erionite                                  | ERI         |               |           |        |                     | LS                 |

Final mineral identification chart using initial sample names, TEM, and SCXRD results.

Table 3.4

|                                | 1a            | 2_Extra_1 | 3_Extra   | 4     | 9             | 10    | 11a   | 12a           | 13a   | 14b   | 15b    | 16_Extra_3 | 17_Extra_1 | 43_Extra | 45_Extra  |
|--------------------------------|---------------|-----------|-----------|-------|---------------|-------|-------|---------------|-------|-------|--------|------------|------------|----------|-----------|
| SiO <sub>2</sub>               | 57.38         | 58.25     | 57.45     | 62.33 | 58.85         | 62.94 | 58.68 | 56.47         | 51.40 | 55.04 | 58.85  | 60.72      | 59.13      | 60.41    | 59.95     |
| Al <sub>2</sub> O <sub>3</sub> | 16.60         | 17.28     | 16.77     | 16.57 | 17.55         | 17.72 | 17.26 | 19.27         | 20.40 | 20.83 | 14.61  | 15.95      | 14.12      | 16.64    | 17.82     |
| Fe <sub>2</sub> O <sub>3</sub> | –             | –         | –         | –     | 0.14          | –     | –     | 0.04          | –     | –     | 0.05   | –          | –          | 0.05     | 0.05      |
| MgO                            | 1.04          | 2.06      | 1.24      | 0.84  | 1.88          | 1.46  | 1.62  | 0.98          | 2.84  | 3.22  | 0.56   | 0.41       | 1.00       | 1.14     | 0.80      |
| CaO                            | 5.31          | 4.13      | 4.95      | 3.60  | 4.56          | 4.41  | 4.83  | 6.65          | 4.54  | 4.31  | 4.77   | 5.74       | 4.22       | 3.73     | 5.97      |
| SrO                            | 0.14          | 0.09      | 0.16      | 0.09  | 0.09          | 0.08  | 0.13  | 0.21          | 0.16  | 0.08  | 0.05   | 0.15       | 0.10       | 0.07     | 0.15      |
| BaO                            | –             | 0.05      | –         | –     | 0.13          | 0.21  | 0.05  | 0.04          | 0.15  | 0.09  | –      | –          | 0.23       | –        | 0.06      |
| Na <sub>2</sub> O              | 0.09          | 0.13      | 0.35      | 0.62  | 0.09          | 0.22  | –     | –             | 0.06  | 0.17  | 0.20   | 0.06       | 0.16       | 0.54     | 0.09      |
| K <sub>2</sub> O               | 3.19          | 3.35      | 3.41      | 4.77  | 3.57          | 3.82  | 3.23  | 3.27          | 3.08  | 3.48  | 3.42   | 3.19       | 3.11       | 3.83     | 3.48      |
| H <sub>2</sub> O*              | 16.26         | 14.76     | 15.69     | 11.18 | 13.23         | 9.27  | 14.23 | 13.12         | 17.40 | 12.90 | 17.56  | 13.77      | 18.06      | 13.60    | 11.76     |
| Si                             | 26.91         | 26.75     | 26.81     | 27.72 | 26.65         | 26.94 | 26.80 | 25.76         | 24.65 | 24.97 | 27.91  | 27.57      | 28.14      | 27.36    | 26.75     |
| Al                             | 9.17          | 9.36      | 9.22      | 8.48  | 9.37          | 9.25  | 9.29  | 10.36         | 11.54 | 11.14 | 8.16   | 8.53       | 7.89       | 8.89     | 9.37      |
| Fe                             | –             | –         | –         | –     | 0.05          | –     | –     | –             | –     | –     | –      | –          | –          | –        | –         |
| Mg                             | 0.73          | 1.41      | 0.87      | 0.54  | 1.28          | 1.11  | 1.11  | 0.67          | 2.03  | 2.18  | 0.40   | 0.28       | 0.70       | 0.77     | 0.54      |
| Ca                             | 2.67          | 2.03      | 2.47      | 1.72  | 2.21          | 2.03  | 2.36  | 3.25          | 2.34  | 2.10  | 2.42   | 2.79       | 2.15       | 1.81     | 2.85      |
| Sr                             | 0.04          | 0.02      | 0.04      | 0.02  | –             | –     | 0.04  | 0.05          | 0.04  | 0.02  | –      | 0.04       | –          | –        | 0.04      |
| Ba                             | –             | –         | –         | –     | 0.02          | 0.04  | –     | –             | 0.03  | 0.02  | –      | –          | 0.04       | –        | –         |
| Na                             | 0.08          | –         | 0.31      | 0.53  | –             | –     | –     | –             | –     | –     | –      | –          | –          | 0.47     | –         |
| K                              | 1.91          | 1.96      | 2.03      | 2.58  | 2.06          | 2.06  | 1.88  | 1.91          | 1.89  | 2.02  | 2.07   | 1.85       | 1.89       | 2.21     | 1.98      |
| H <sub>2</sub> O               | 13.10         | 11.53     | 12.53     | 8.90  | 10.32         | 7.18  | 11.08 | 10.30         | 14.36 | 10.06 | 14.17  | 10.64      | 14.58      | 10.47    | 8.99      |
| Points per Grain               | 3             | 3         | 3         | 2     | 3             | 3     | 5     | 6             | 3     | 4     | 4      | 2          | 3          | 5        | 12        |
| R-value                        | 0.746         | 0.739     | 0.744     | 0.764 | 0.737         | 0.747 | 0.743 | 0.713         | 0.678 | 0.691 | 0.776  | 0.768      | 0.767      | 0.755    | 0.741     |
| E%                             | 3.67          | 4.64      | 1.36      | 10.45 | 0.03          | 0.09  | 4.44  | 5.21          | 7.10  | 4.33  | 4.01   | 5.31       | 1.22       | 13.01    | 5.53      |
| a (Å <sup>3</sup> )            | 13.31         | 12.84     | 13.31     | 13.26 | 13.39         | 13.29 |       |               |       |       | 13.326 |            |            |          |           |
| c (Å <sup>3</sup> )            | 15.15         | 14.66     | 15.14     | 15.06 | 15.22         | 15.12 |       |               |       |       | 15.153 |            |            |          |           |
| V (Å <sup>3</sup> )            | 2325          | 2091      | 2325      | 2295  | 2362          | 2313  |       |               |       |       | 2330   |            |            |          |           |
| Sign of Elongation             | L.S./<br>L.F. | L.S.      | L.S./L.F. | L.S.  | L.S./<br>L.F. | L.S.  | L.S.  | L.S./<br>L.F. | L.F.  | L.F.  | L.S.   | L.S./L.F.  | L.S.       | L.S.     | L.S./L.F. |

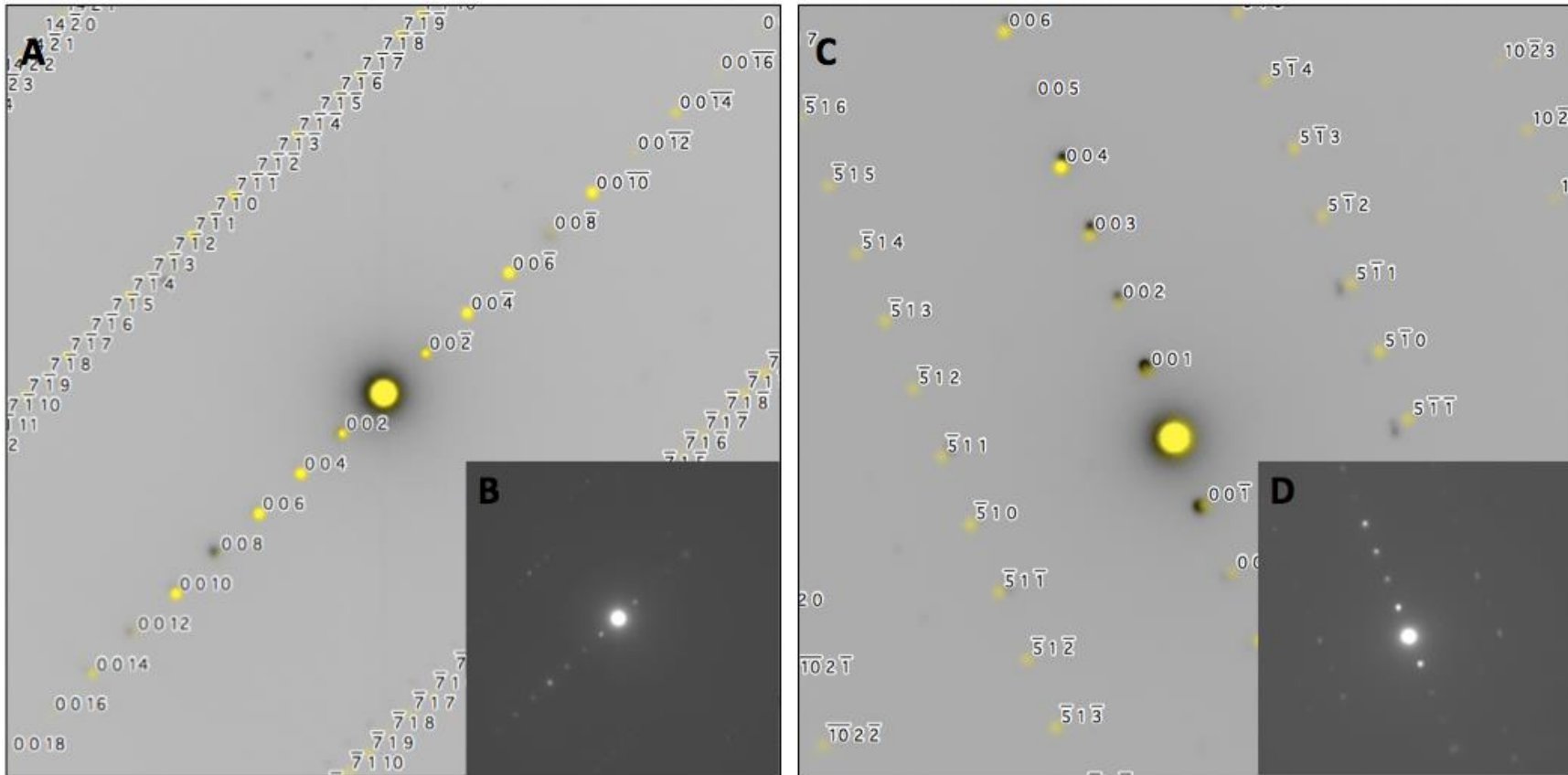
Erionite samples used in this study showing average chemistry per grain. H<sub>2</sub>O\* was calculated by difference with EPMA. E% = Balance Error Calculation, R-value = Si/(Si+Al) (Passaglia, 1970; Passaglia et al, 1998. L.S. = length slow, L.F. = length fast. Values in red indicate Mg contents > 0.80 (Gualtieri et al, 1998; Dogan and Dogan, 2008, Dogan, 2011).

Table 3.5

|                                | 5a    | 7b     | 29a   | 30    | 31b           | 32b           | 33b           |
|--------------------------------|-------|--------|-------|-------|---------------|---------------|---------------|
| SiO <sub>2</sub>               | 42.26 | 53.51  | 53.95 | 55.16 | 52.82         | 54.81         | 52.59         |
| Al <sub>2</sub> O <sub>3</sub> | 21.08 | 20.21  | 20.03 | 19.47 | 18.99         | 19.61         | 19.63         |
| Fe <sub>2</sub> O <sub>3</sub> | -     | -      | 0.06  | -     | -             | -             | -             |
| MgO                            | -     | 3.21   | 0.59  | 2.98  | 2.94          | 2.92          | 2.87          |
| CaO                            | 9.04  | 4.31   | 6.91  | 4.10  | 3.94          | 4.14          | 3.37          |
| SrO                            | 0.08  | 0.19   | 0.07  | 0.06  | 0.07          | 0.10          | 0.86          |
| BaO                            | -     | 0.04   | 0.10  | -     | -             | 0.07          | 0.08          |
| Na <sub>2</sub> O              | 2.43  | -      | 0.80  | -     | -             | 0.06          | 0.15          |
| K <sub>2</sub> O               | 1.04  | 3.58   | 3.31  | 3.53  | 3.39          | 3.51          | 3.37          |
| H <sub>2</sub> O*              | 24.10 | 14.94  | 14.23 | 14.70 | 17.85         | 14.92         | 17.16         |
| Si                             | 11.31 | 12.46  | 12.56 | 12.74 | 12.67         | 12.70         | 12.57         |
| Al                             | 6.65  | 5.55   | 5.50  | 5.30  | 5.37          | 5.36          | 5.55          |
| Fe                             | -     | -      | -     | -     | -             | -             | -             |
| Mg                             | -     | 1.12   | 0.21  | 1.02  | 1.05          | 1.01          | 1.03          |
| Ca                             | 2.59  | 1.08   | 1.73  | 1.02  | 1.01          | 1.03          | 0.86          |
| Sr                             | -     | 0.03   | -     | -     | -             | -             | 0.12          |
| Ba                             | -     | -      | 0.01  | -     | -             | -             | -             |
| Na                             | 1.26  | -      | 0.36  | -     | -             | -             | -             |
| K                              | 0.35  | 1.06   | 0.98  | 1.04  | 1.04          | 1.04          | 1.03          |
| H <sub>2</sub> O               | 11.36 | 5.99   | 5.78  | 5.82  | 7.34          | 5.93          | 7.24          |
| Points per Grain               | 2     | 5      | 3     | 7     | 7             | 9             | 9             |
| E%                             | -2.30 | 0.91   | 5.17  | 3.28  | 3.60          | 4.39          | 8.73          |
| R-value                        | 0.630 | 0.692  | 0.695 | 0.706 | 0.702         | 0.703         | 0.694         |
| a (Å <sup>3</sup> )            | -     | 13.31  |       |       |               |               |               |
| c (Å <sup>3</sup> )            | -     | 7.59   |       |       |               |               |               |
| V (Å <sup>3</sup> )            | -     | 1165.6 |       |       |               |               |               |
| Sign of Elongation             | -     | L.F.   | L.F.  | L.S.  | L.S./<br>L.F. | L.S./<br>L.F. | L.S./<br>L.F. |

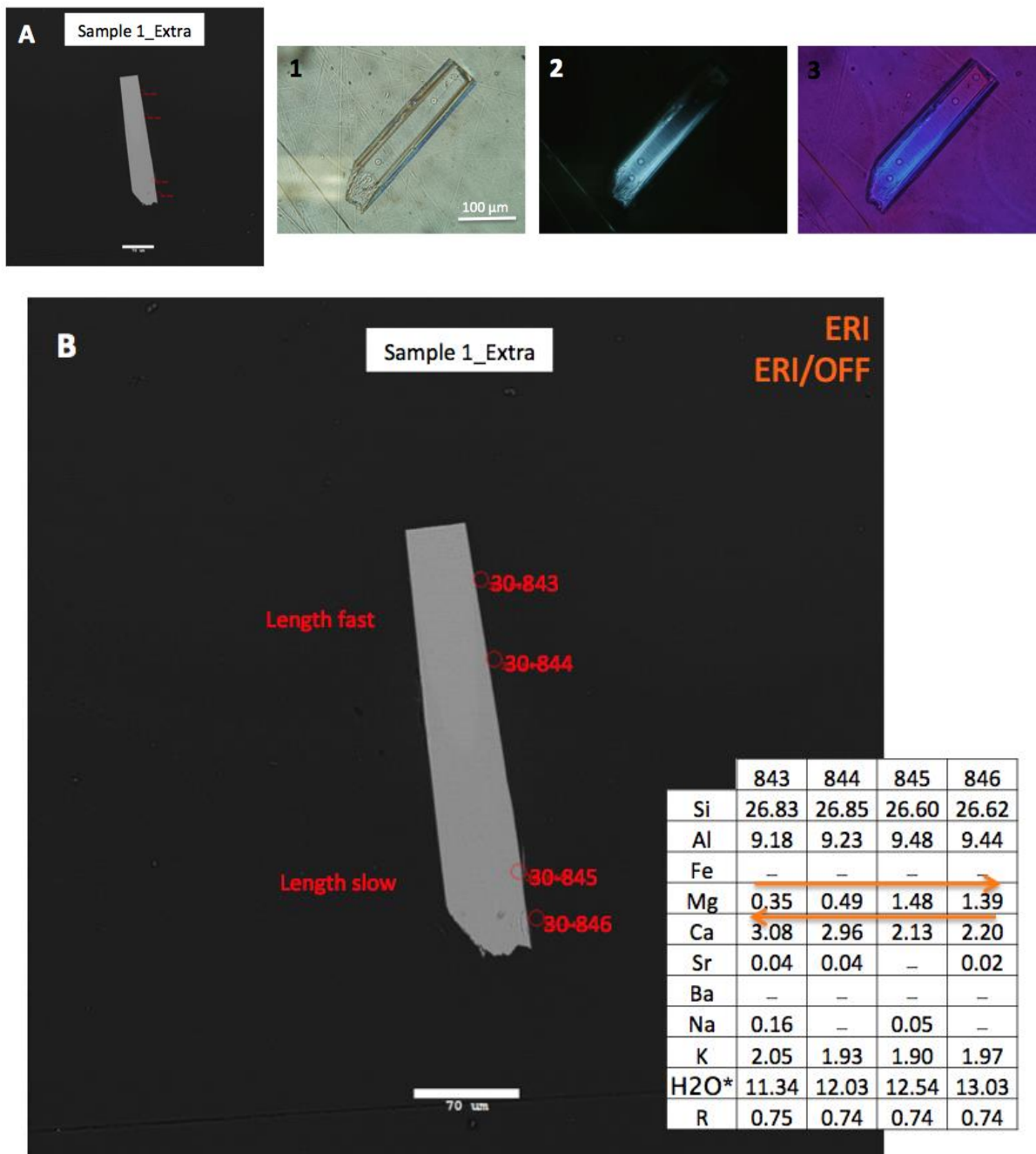
Offretite samples used in this study showing average chemistry per grain. H<sub>2</sub>O\* was calculated by difference with EPMA. E% = Balance Error Calculation, R-value = Si/(Si+Al) (Passaglia, 1970; Passaglia et al, 1998. L.S. = length slow, L.F. = length fast.

Figure 3.1



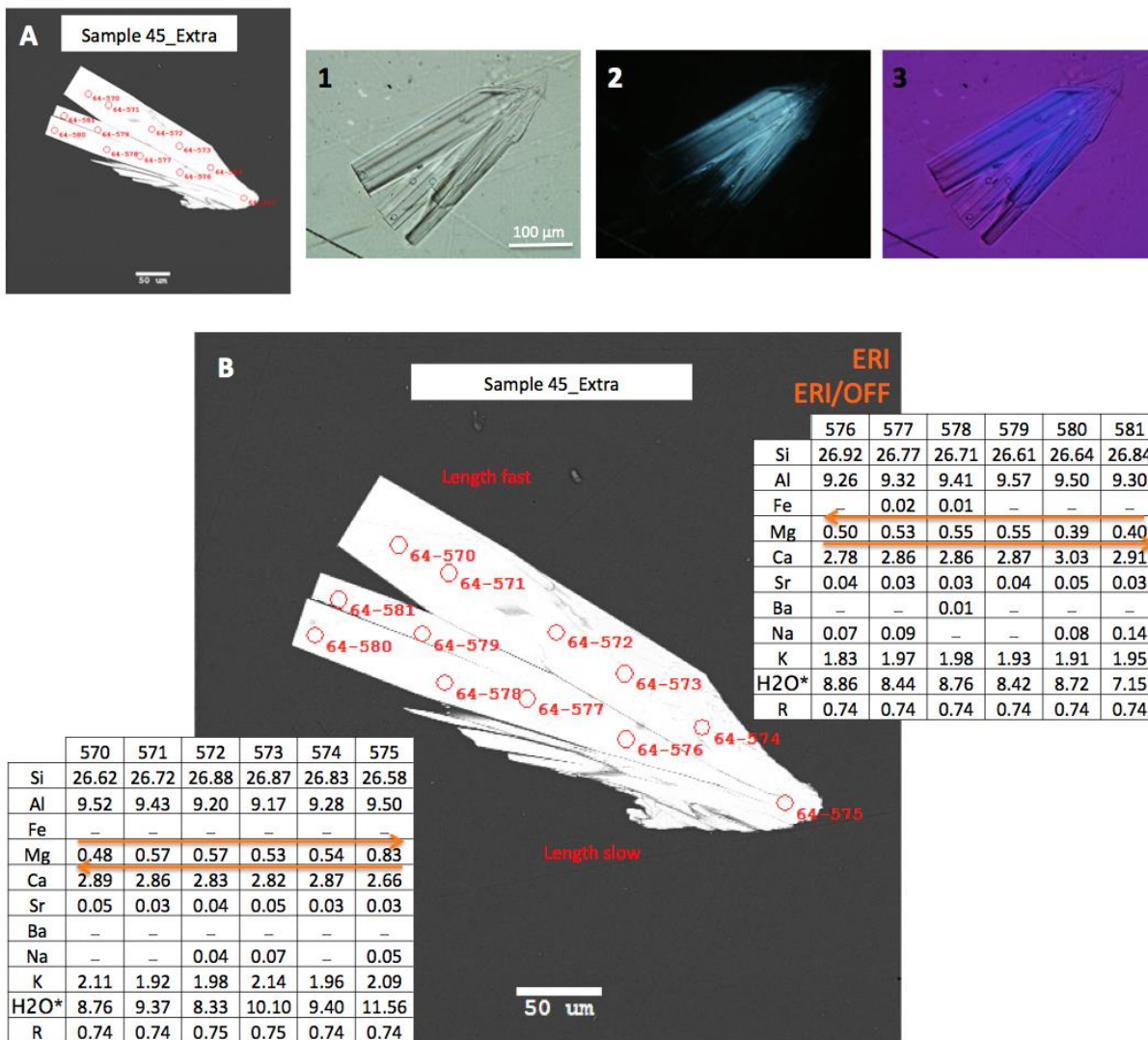
Indexed diffraction patterns of (A) erionite 170 zone axis and (C) offretite 150 zone axis from sample location #1, Phelps Dodge Co. Well No. 1, Little Ajo Mtns, Ajo District, Pima County, AZ, USA. Yellow dots indicate the simulated pattern while black dots indicate the actual diffraction pattern. Images (B) and (D) show the original diffraction pattern. Simulated diffraction pattern (yellow dots) data is taken from Gualtieri et al., 1998.

Figure 3.2



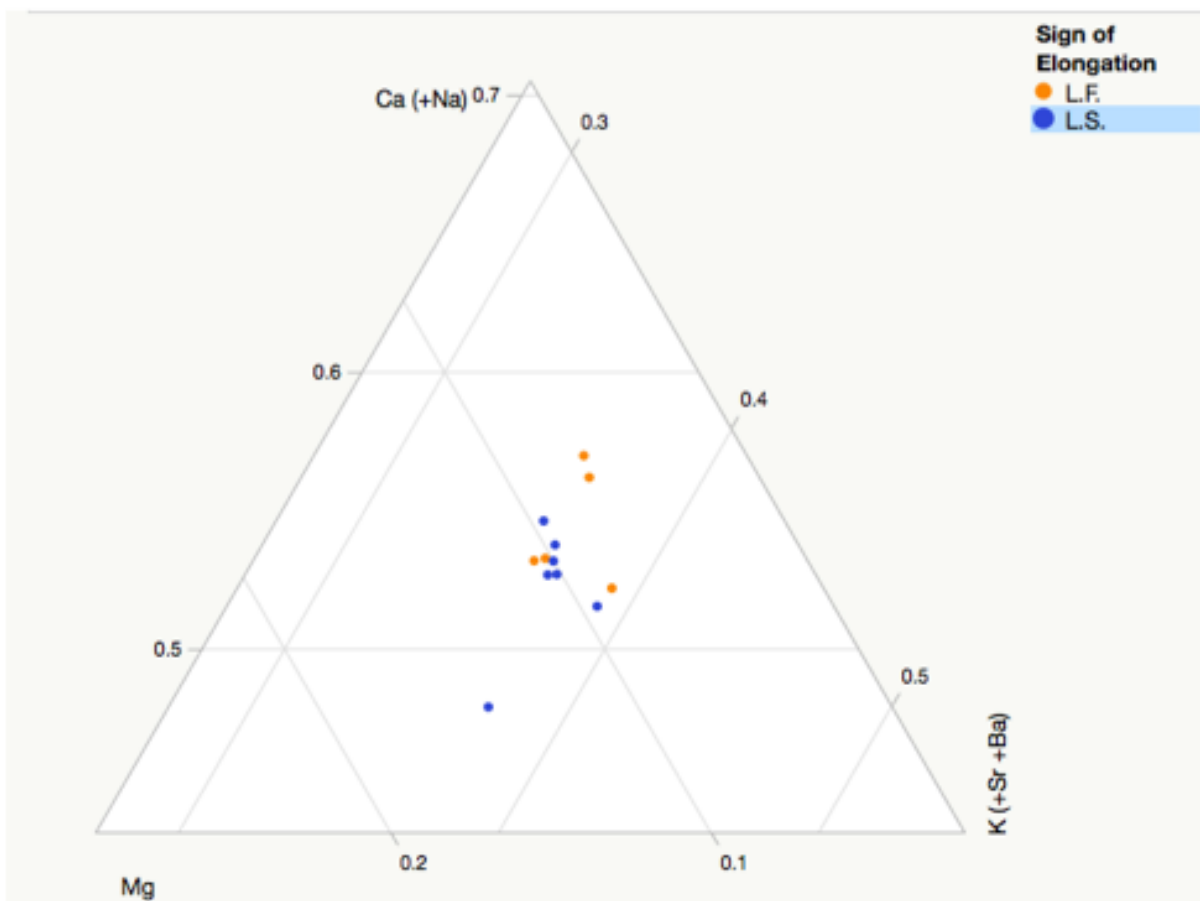
(A) shows a backscattered electron (BSE) images of a sample of erionite from Phelps Dodge Co. Well No. 1, Little Ajo Mtns, Ajo District, Pima County, AZ, USA. A1 and B1 show PLM images, A2 and B2 are XPL images where extinction on the grain tip is visible. A3 and B3 are XPL images with the  $\lambda$  accessory plate inserted clearly showing different signs of elongation on each grain. (B) BSE image of erionite sample from Phelps Dodge Co. Well No. 1, Little Ajo Mtns, Ajo District, Pima County, AZ, USA along with associated APFU data.

Figure 3.3



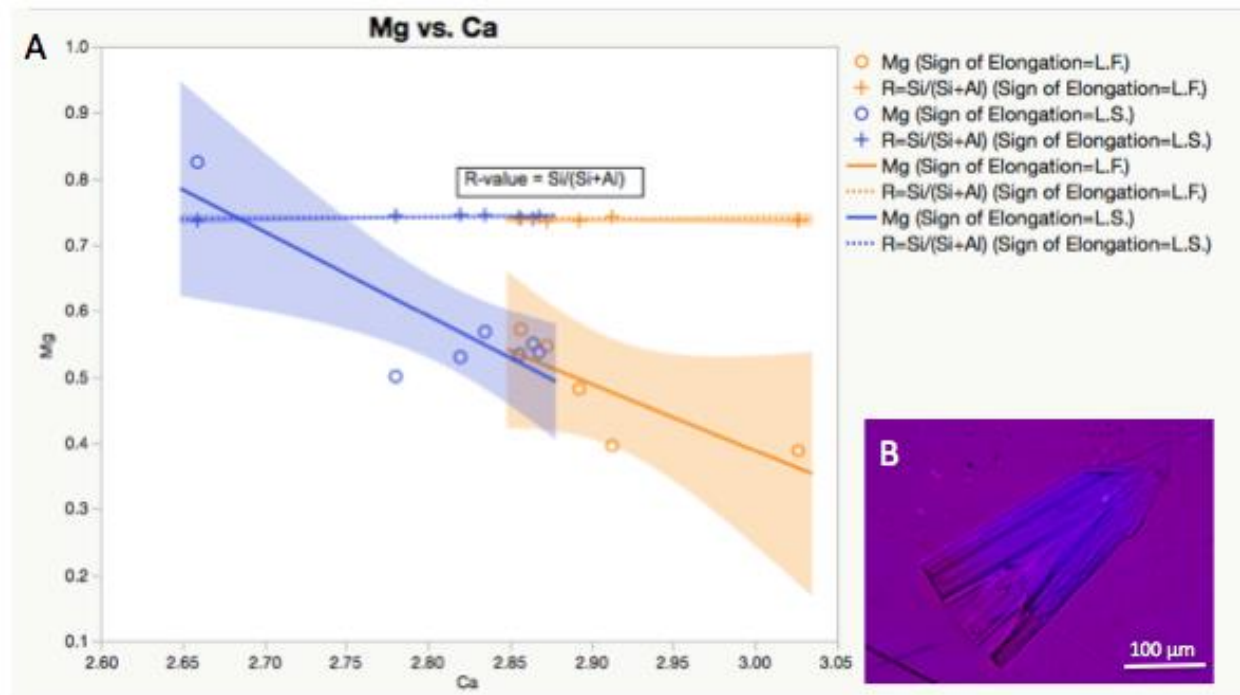
(A) shows a backscattered electron (BSE) images of a sample of erionite from Phelps Dodge Co. Well No. 1, Little Ajo Mtns, Ajo District, Pima County, AZ, USA. A1 and B1 show PLM images, A2 and B2 are XPL images where extinction on the grain tip is visible. A3 and B3 are XPL images with the  $\lambda$  accessory plate inserted clearly showing different signs of elongation on each grain. (B) BSE image of erionite sample from Phelps Dodge Co. Well No. 1, Little Ajo Mtns, Ajo District, Pima County, AZ, USA along with associated APFU data.

Figure 3.4



Ternary diagram of individual APFU and sign of elongation points from erionite sample 45\_extra.

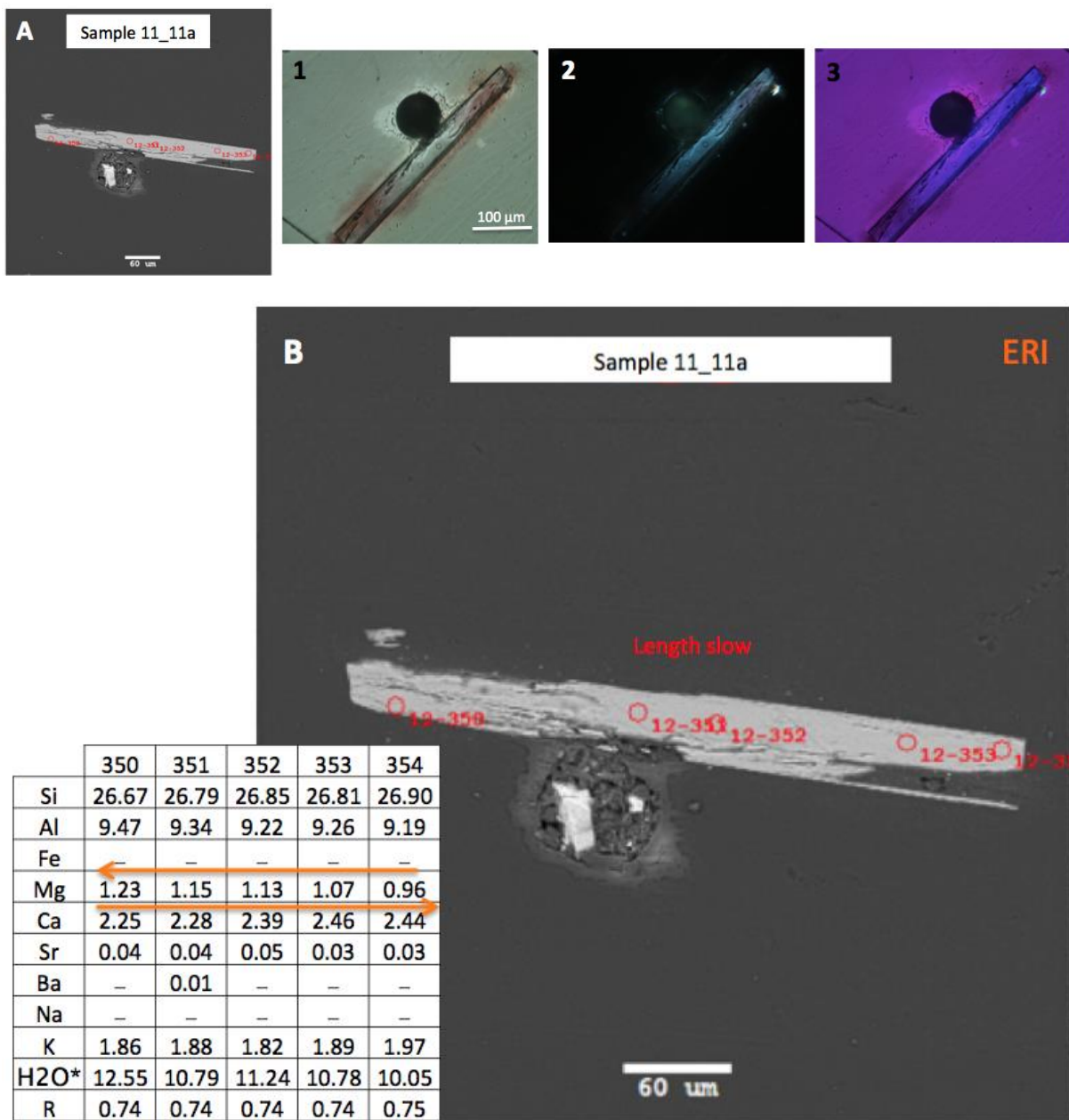
Figure 3.5



(A) scatter diagram of erionite sample number 45\_extra with Mg vs. Ca along with sign of elongation and R-value. Graphs show line of best fit along with confidence intervals in the shaded regions. (B) XPL image with accessory plate inserted of sample 45\_extra.

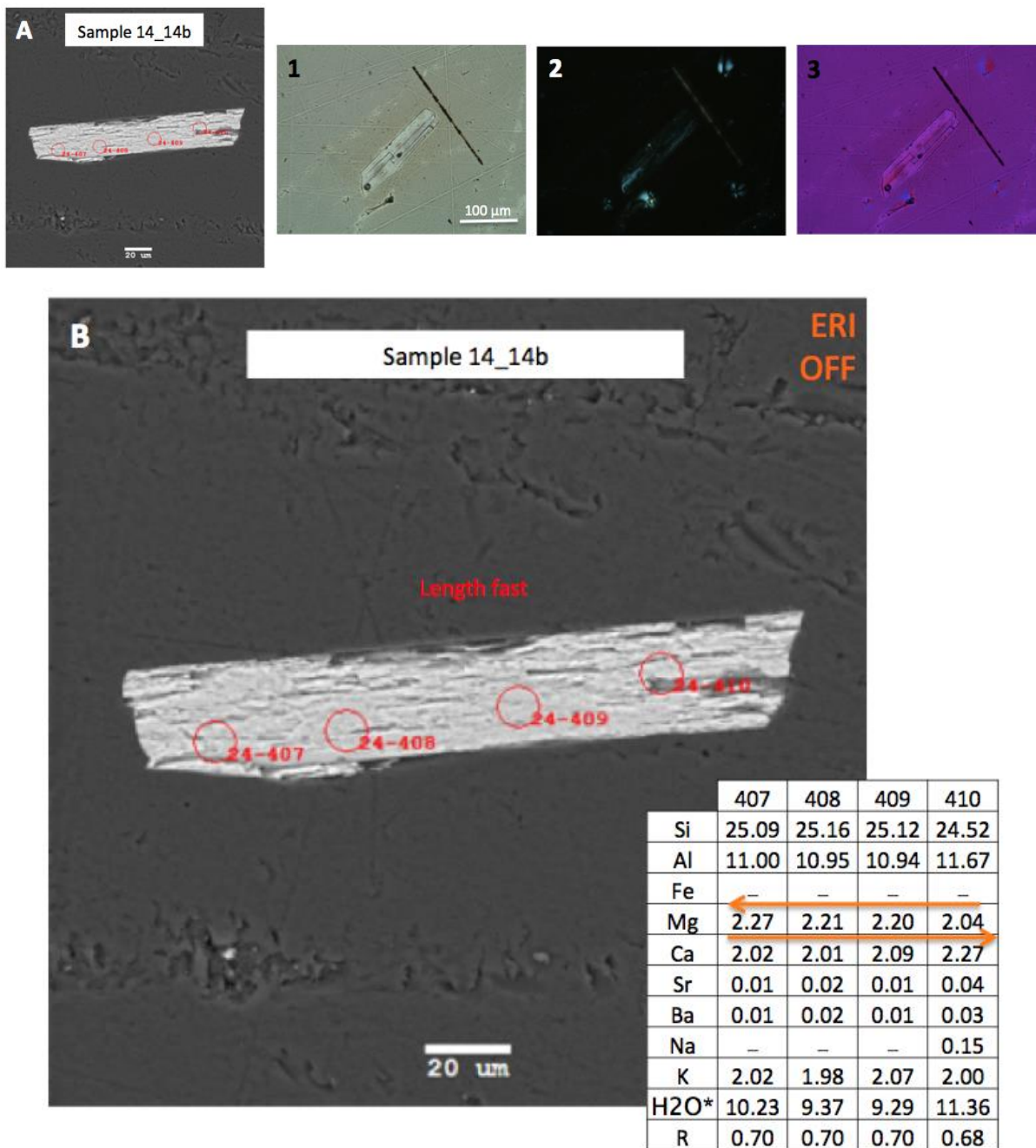


Figure 3.6



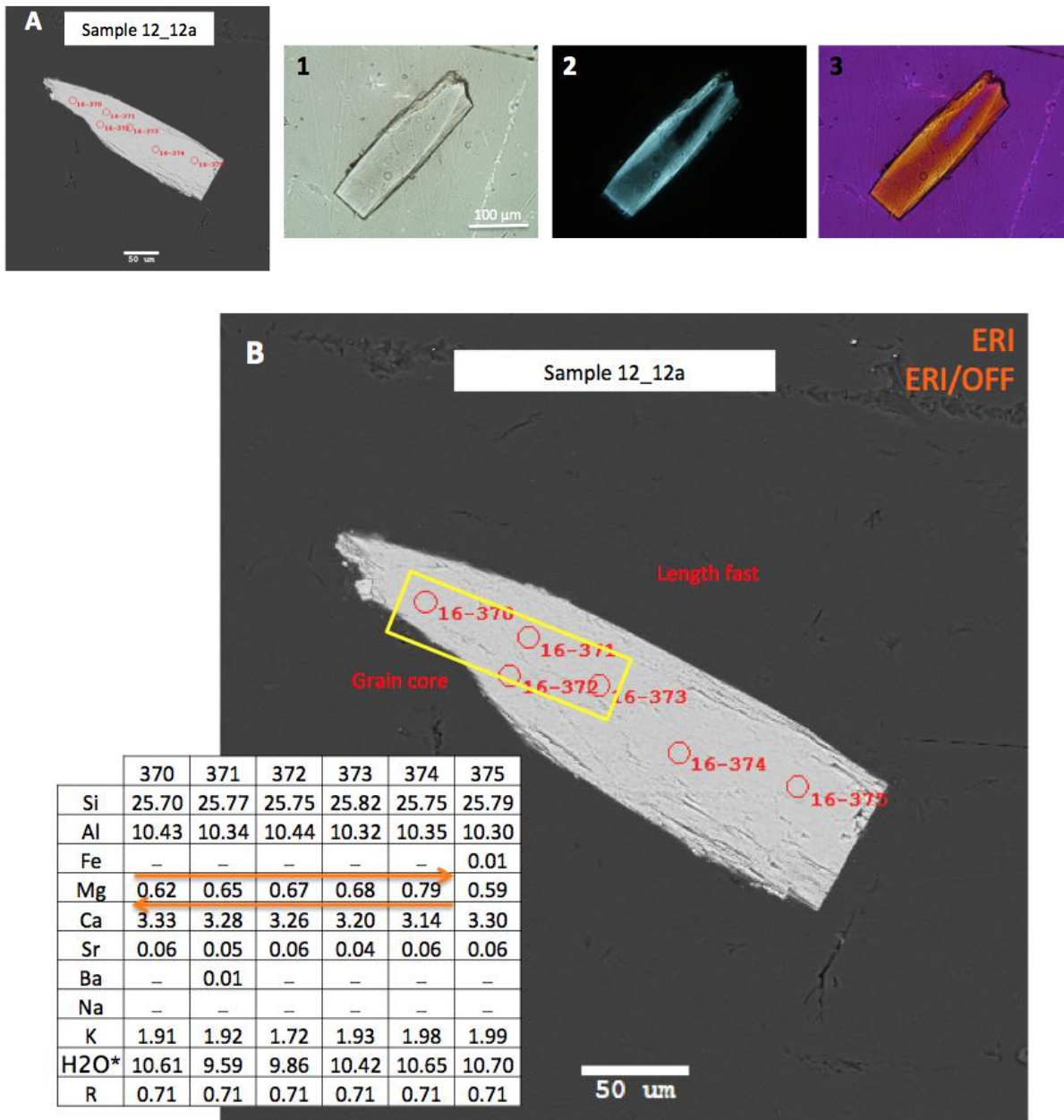
(A) shows a backscattered electron (BSE) images of a sample of erionite from Clifton, Greenlee Co, AZ, USA. A1 and B1 show PLM images, A2 and B2 are XPL images where extinction on the grain tip is visible. A3 and B3 are XPL images with the  $\lambda$  accessory plate inserted clearly showing different signs of elongation on each grain. (B) BSE image of erionite sample along with associated APFU data.

Figure 3.7



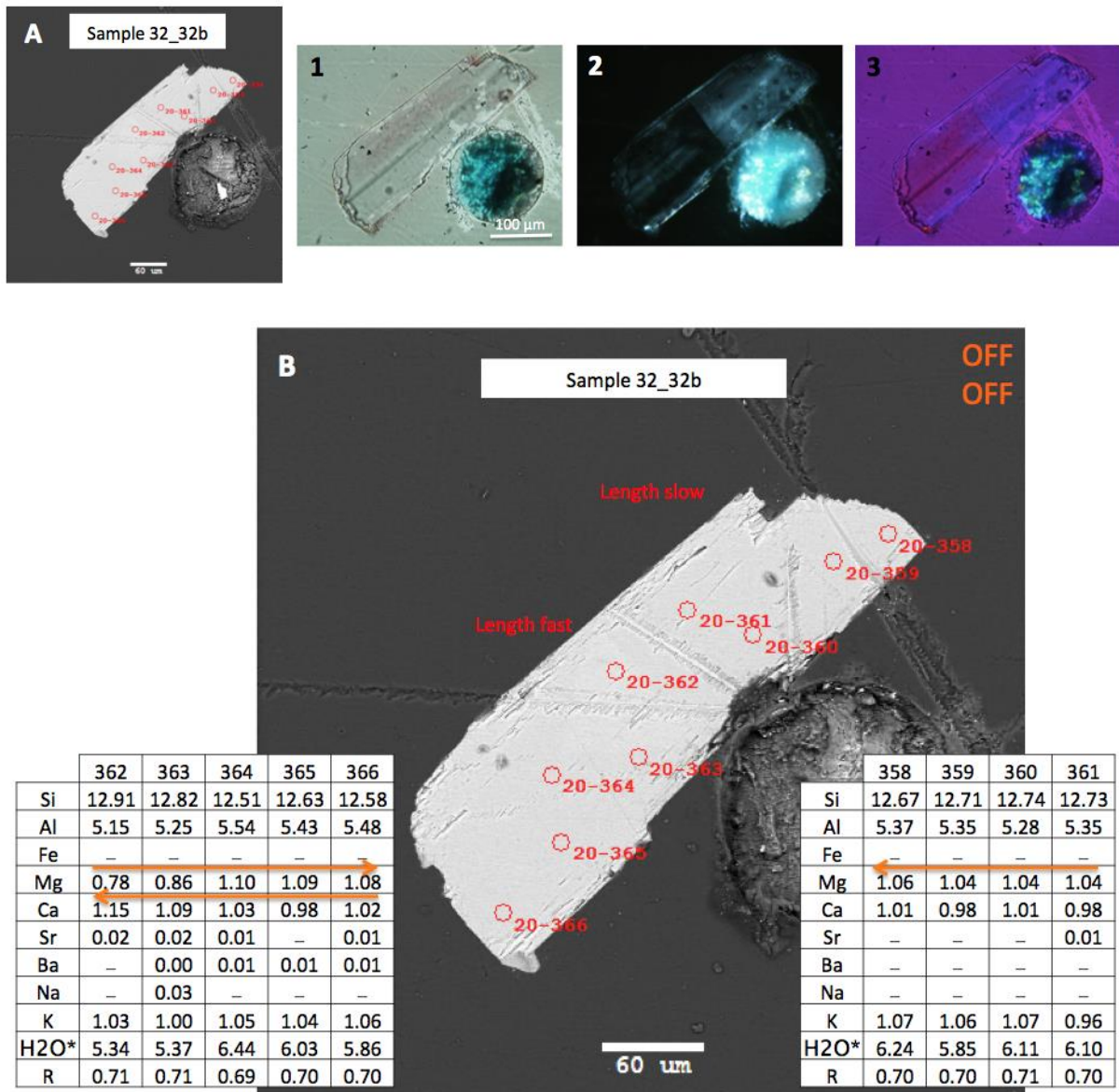
(A) shows a backscattered electron (BSE) images of a sample of erionite from Herbstein, Vogelsberg, Hesse, Germany. A1 and B1 show PLM images, A2 and B2 are XPL images where extinction on the grain tip is visible. A3 and B3 are XPL images with the  $\lambda$  accessory plate inserted clearly showing different signs of elongation on each grain. (B) BSE image of erionite sample along with associated APFU data.

Figure 3.8



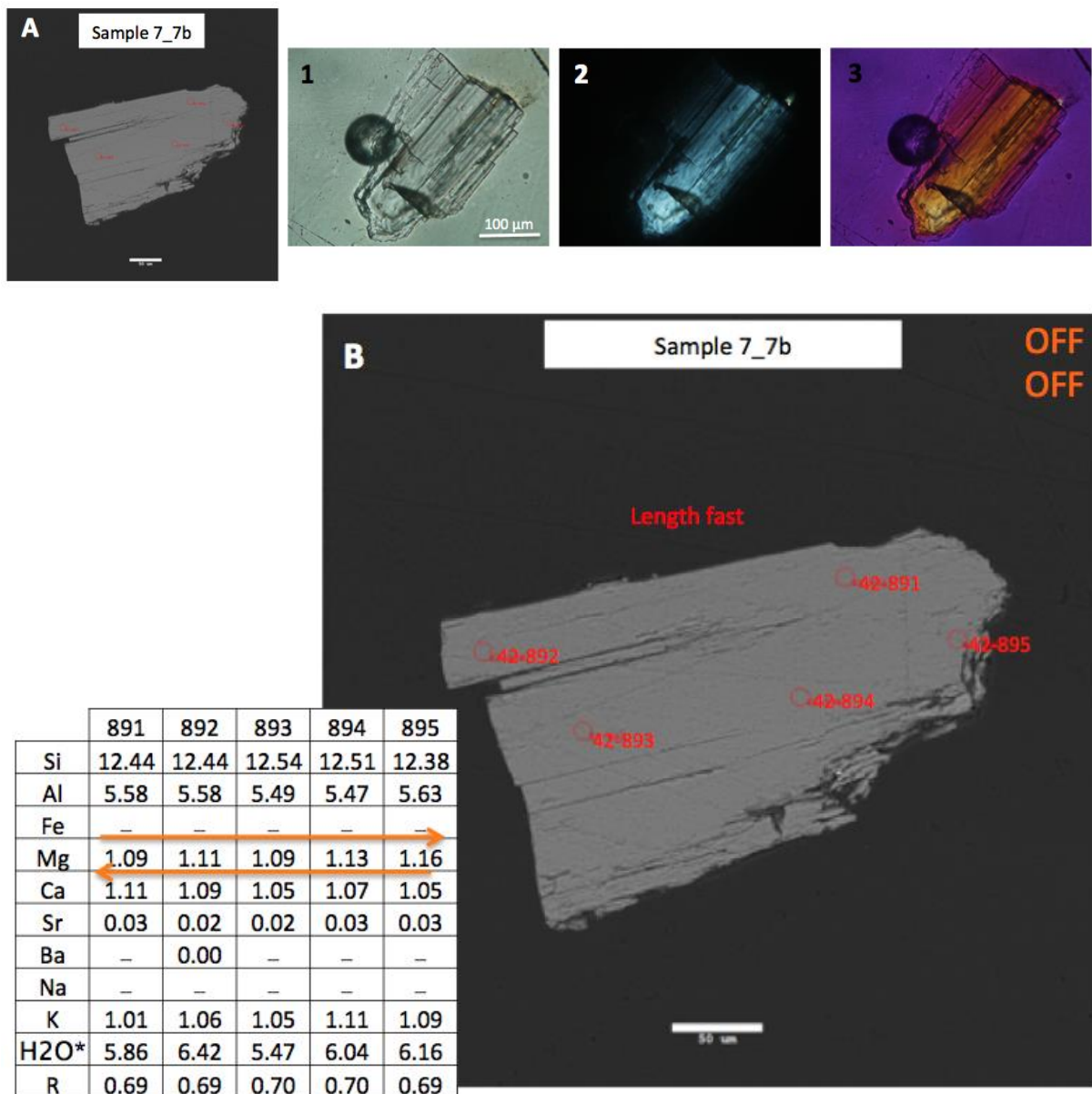
(A) shows a backscattered electron (BSE) images of a sample of erionite from Eureka Valley, Del Norte Co, California, USA. A1 and B1 show PLM images, A2 and B2 are XPL images where extinction on the grain tip is visible. A3 and B3 are XPL images with the  $\lambda$  accessory plate inserted clearly showing different signs of elongation on each grain. (B) BSE image of erionite sample along with associated APFU data.

Figure 3.9



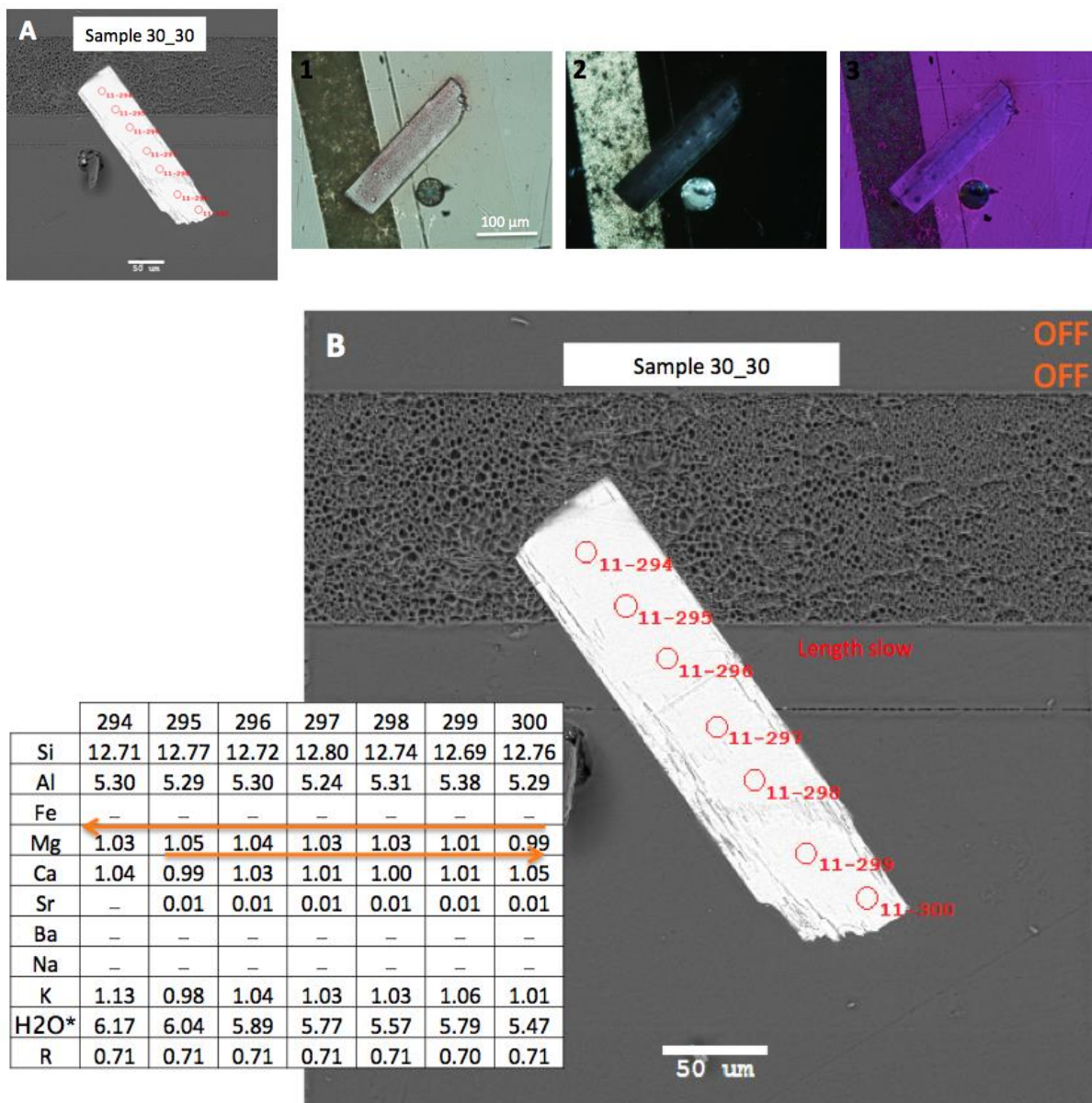
(A) shows a backscattered electron (BSE) images of a sample of offretite from Mt. Simoise Semiol, Chatelneuf, Loire, Rhone Alpes, France. A1 and B1 show PLM images, A2 and B2 are XPL images where extinction on the grain tip is visible. A3 and B3 are XPL images with the  $\lambda$  accessory plate inserted clearly showing different signs of elongation on each grain. (B) BSE image of offretite sample along with associated APFU data.

Figure 3.10



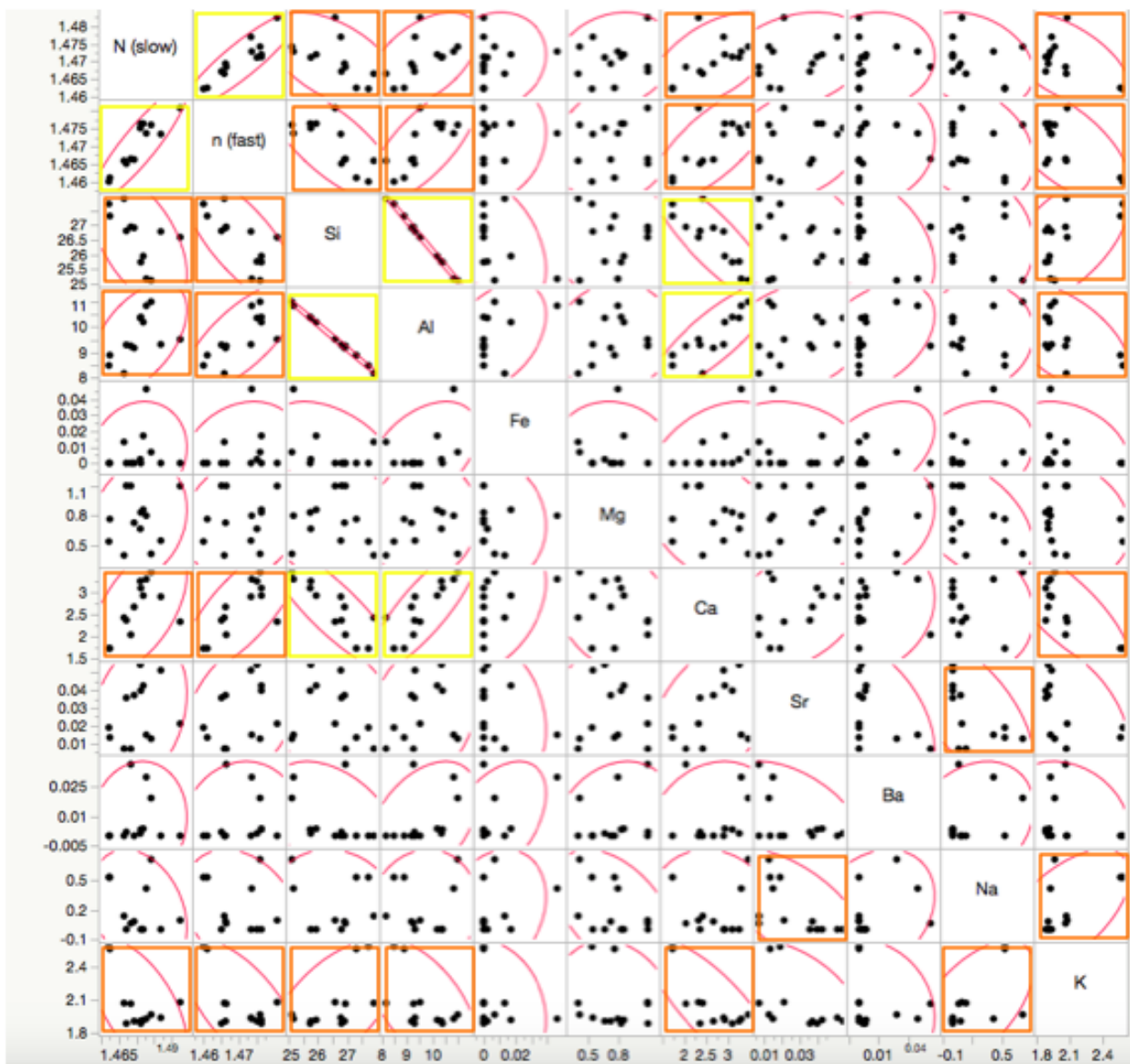
(A) shows a backscattered electron (BSE) images of a sample of offretite from Adamella, Italy. A1 and B1 show PLM images, A2 and B2 are XPL images where extinction on the grain tip is visible. A3 and B3 are XPL images with the  $\lambda$  accessory plate inserted clearly showing different signs of elongation on each grain. (B) BSE image of offretite sample along with associated APFU data.

Figure 3.11



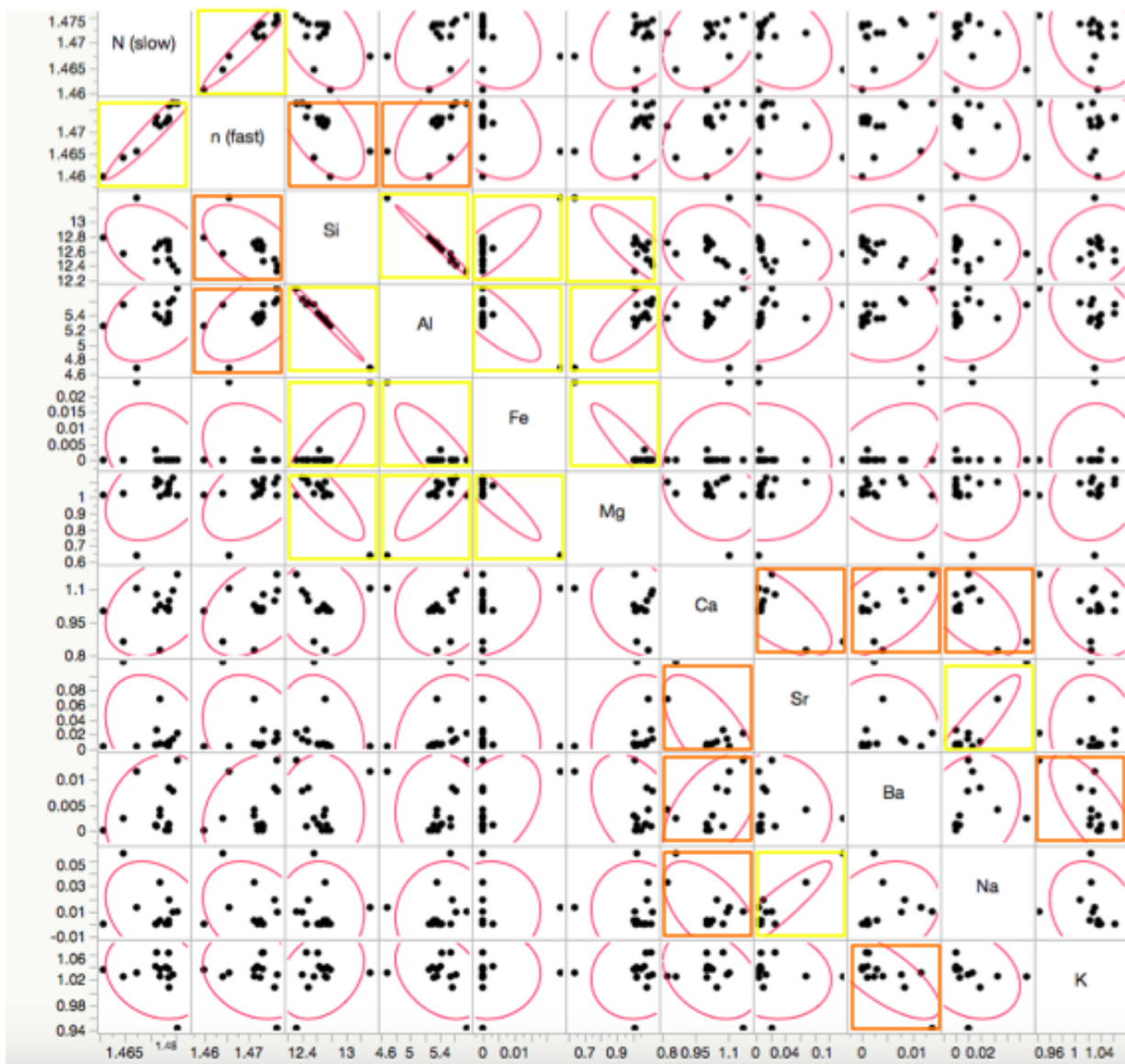
(A) shows a backscattered electron (BSE) images of a sample of offretite from Mount Semiol, Chatelneuf, Loire, Rhone Alpes, France. A1 and B1 show PLM images, A2 and B2 are XPL images where extinction on the grain tip is visible. A3 and B3 are XPL images with the  $\lambda$  accessory plate inserted clearly showing different signs of elongation on each grain. (B) BSE image of offretite sample along with associated APFU data.

Figure 3.12



Erionite correlation coefficients between APFU. Yellow boxes = strong correlation while orange boxes = moderate correlations between variables.

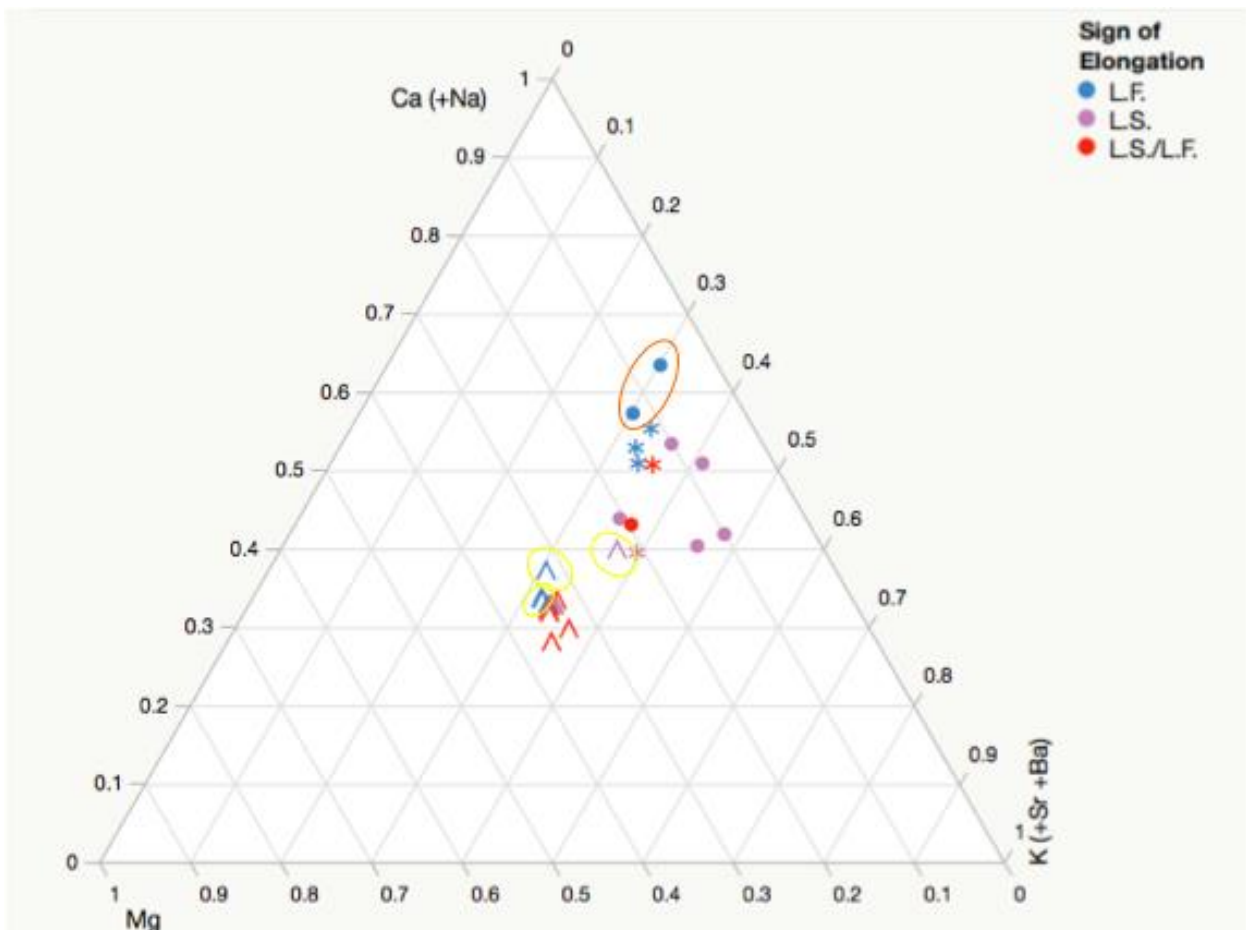
Figure 3.13



Off-tite correlation coefficients between APFU. Yellow boxes = strong correlation while orange boxes = moderate correlations between variables.

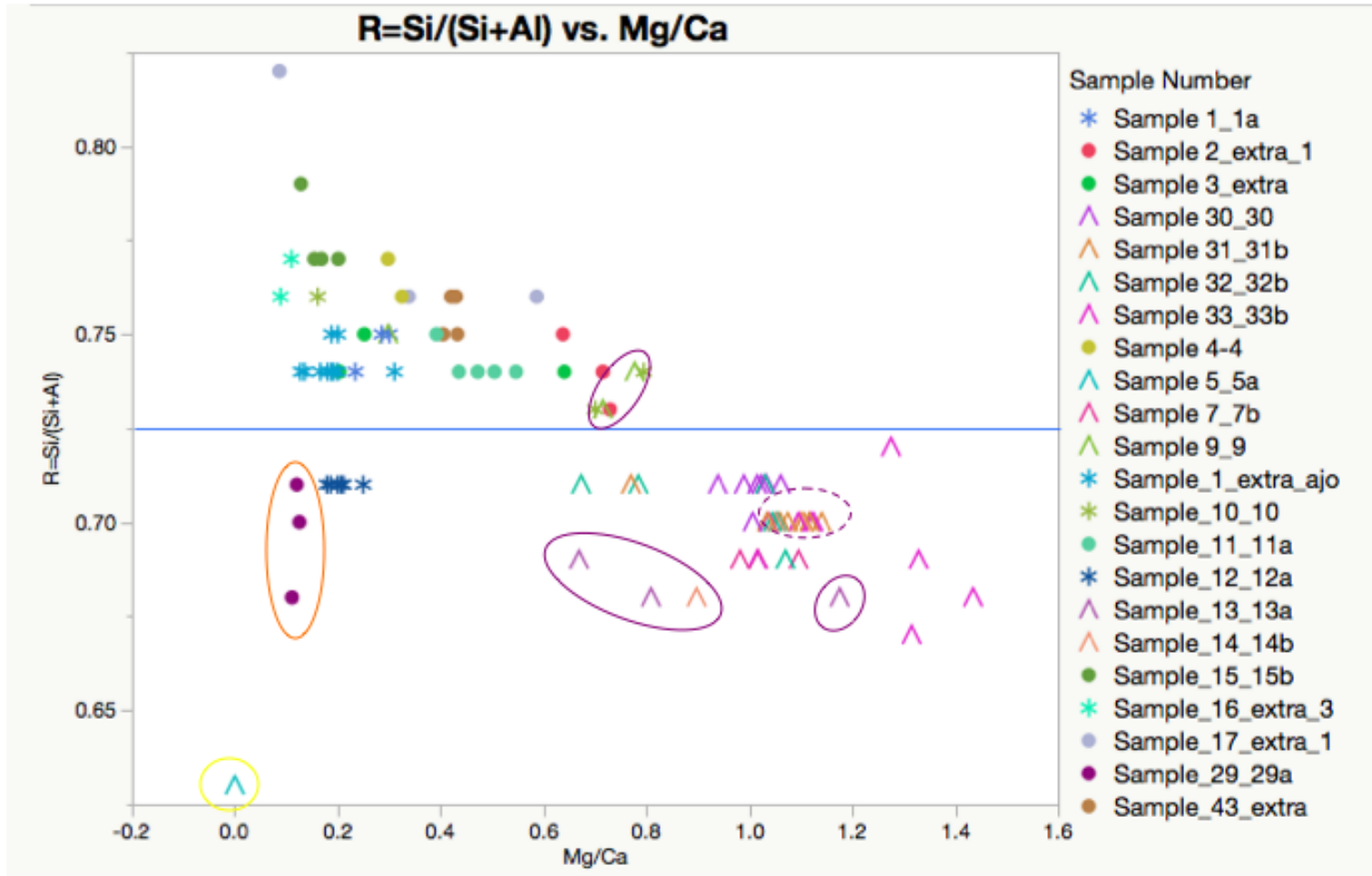


Figure 3.14



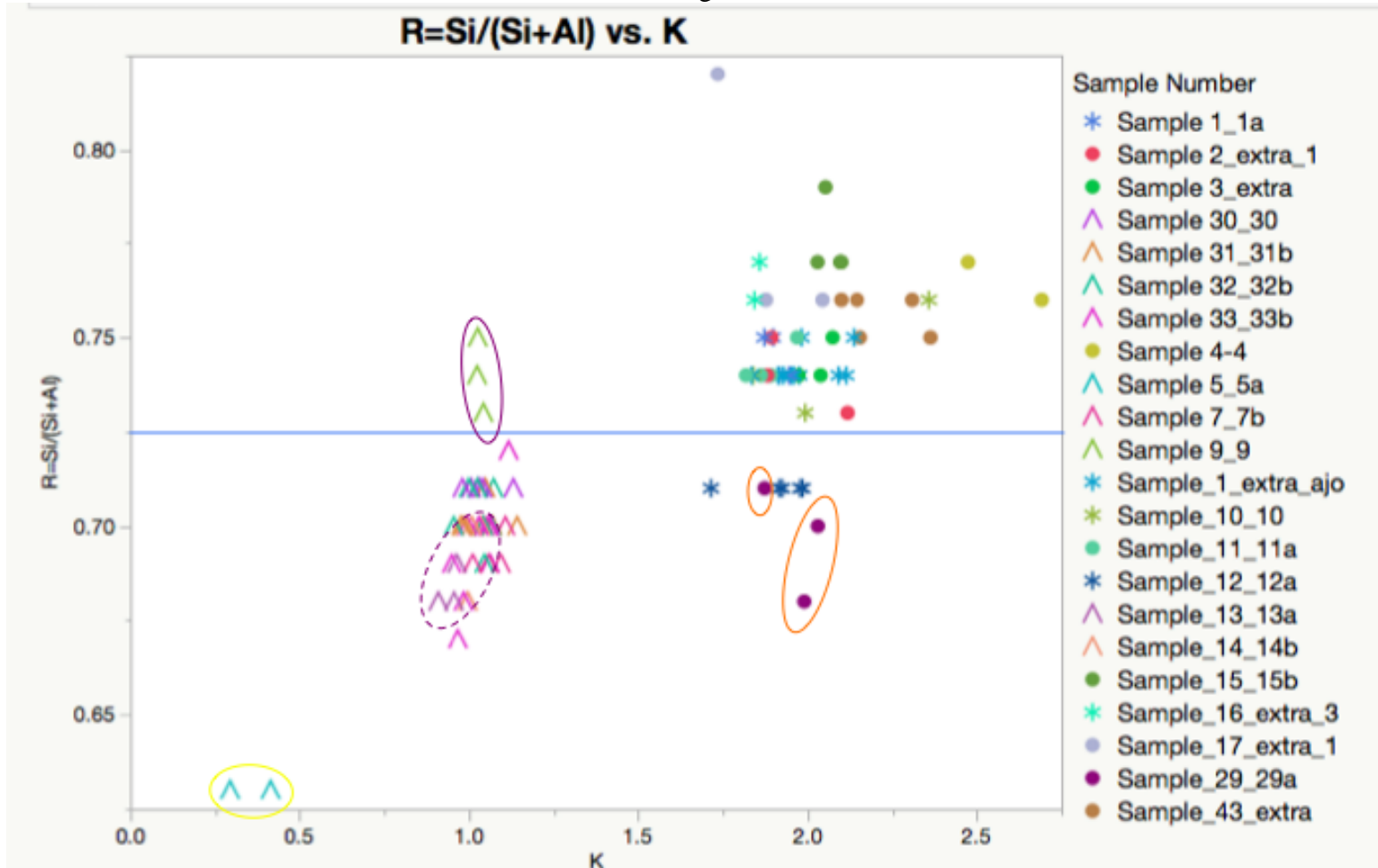
Ternary diagram of erionite (circles), offretite (arrow), and erionite/offretite (star) APFU, and sign of elongation. Yellow circle indicates mislabeled erionite samples (actually offretite) 9, 13a, 14, and 14b. Orange circle indicates mislabeled offretite (actually erionite) samples 29 and 29a.

Figure 3.15



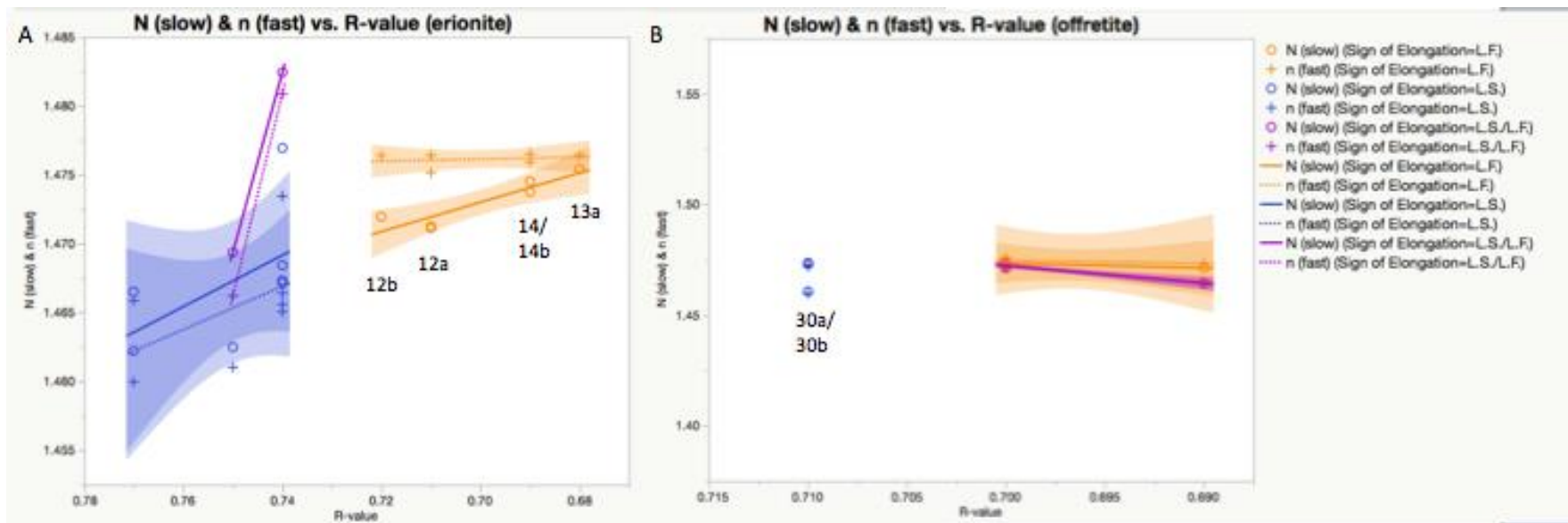
Scatter diagram of erionite (circle), offretite (arrow), and erionite/offretite (star) samples used in this study of R-value vs. Mg/Ca. Values based off of APFU calculations. Blue line marks the division between the majority of the erionite and offretite samples with respect to the R-value. Samples in the orange circle are mislabeled offretite samples (actually erionite) 29a. Yellow circle indicates offretite overgrown on levyne 5a. Purple circles are mislabeled erionite samples (actually offretite) 9, 13a and 14b.

Figure 3.16



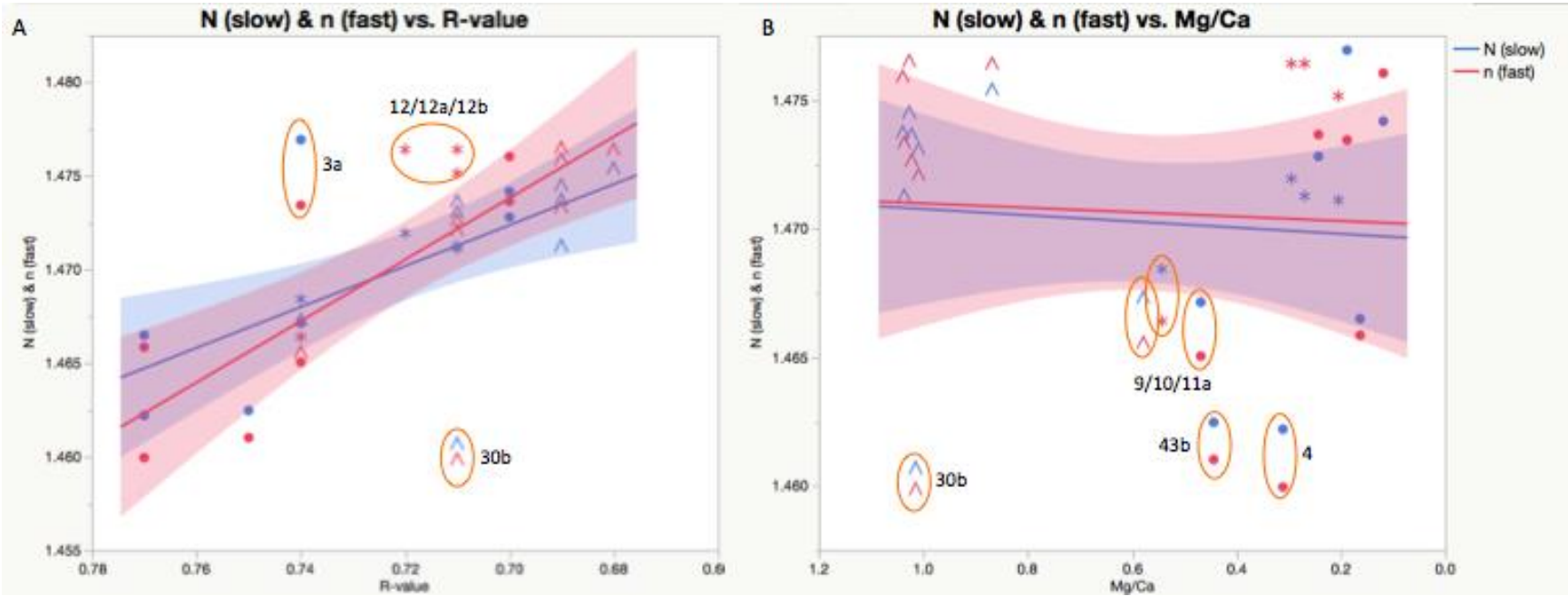
Scatter diagram of erionite (circle), offretite (arrow), and erionite/offretite (star) samples used in this study of R-value vs. K. Values based off of APFU calculations. Blue line marks the division between the majority of the erionite and offretite samples with respect to the R-value. Sample in the orange circles are mislabeled offretite samples (actually erionite) 29a. Yellow circle is offretite overgrown on levyne (5a). Purple circles are mislabeled erionites (actually offretites) 9, 13a, and 14b.

Figure 3.17



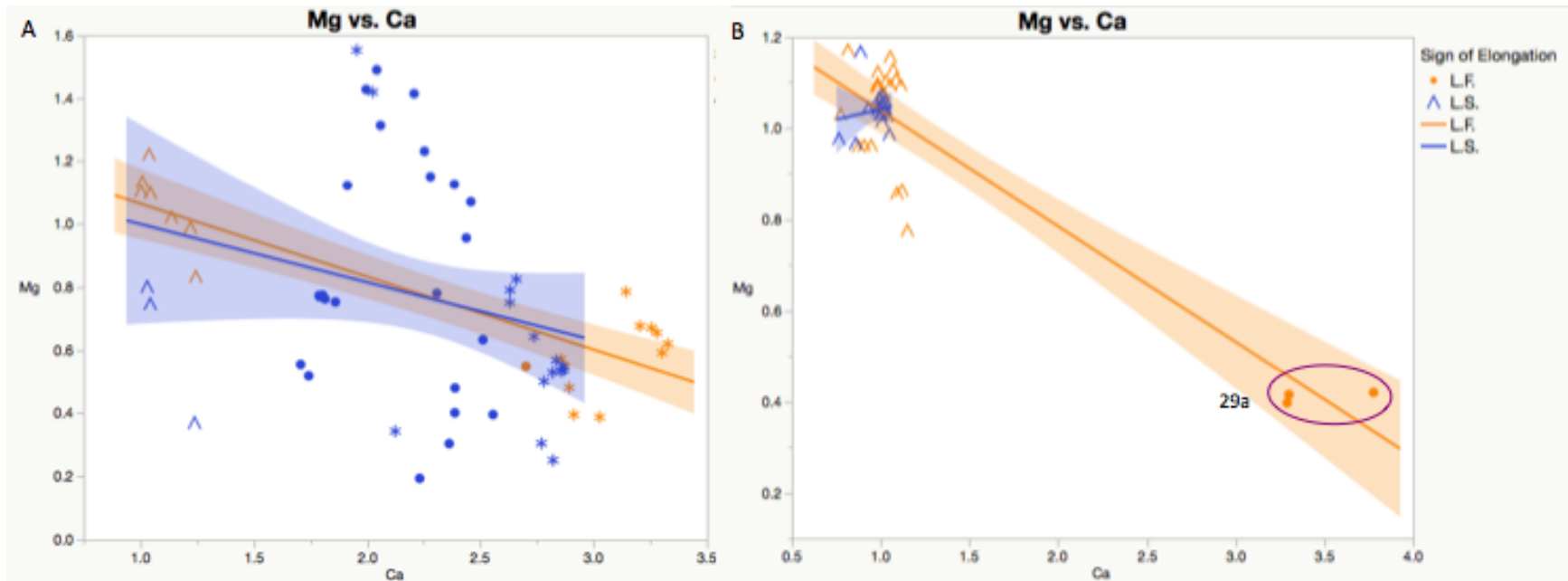
Scatter diagram of (A) erionite and (B) offretite samples used in this study showing fast (+) and slow (circle) rays vs. R-value. R-value in AFPU. Shaded regions show confidence intervals.

Figure 3.18



Scatter diagram of erionite (circle), offretite (arrow), erionite/offretite (star) samples used in this study of (A) length fast (red) and length slow (blue) vs. R-value and (B) length fast (red) and length slow (blue) vs. Mg/Ca. R-value in APFU. Lines of best fit along with confidence intervals (shaded region) can be seen. Outliers (orange circles).

Figure 3.19



(A) scatter diagram of erionite samples used in this study showing Mg vs Ca. Shaded regions show confidence intervals. (B) scatter diagram of offretite samples used in this study showing Mg vs Ca. Shaded regions show confidence intervals (orange) points and length slow (blue) points. Erionite (circles), offretite (arrow), erionite/offretite (star).

Appendix A: Figure 1



Literature refractive index values for the elongate zeolites (Deer et al, 1967; Tröger et al, 1979; Gottardi and Galli, 1985; Tschernich, 1992).

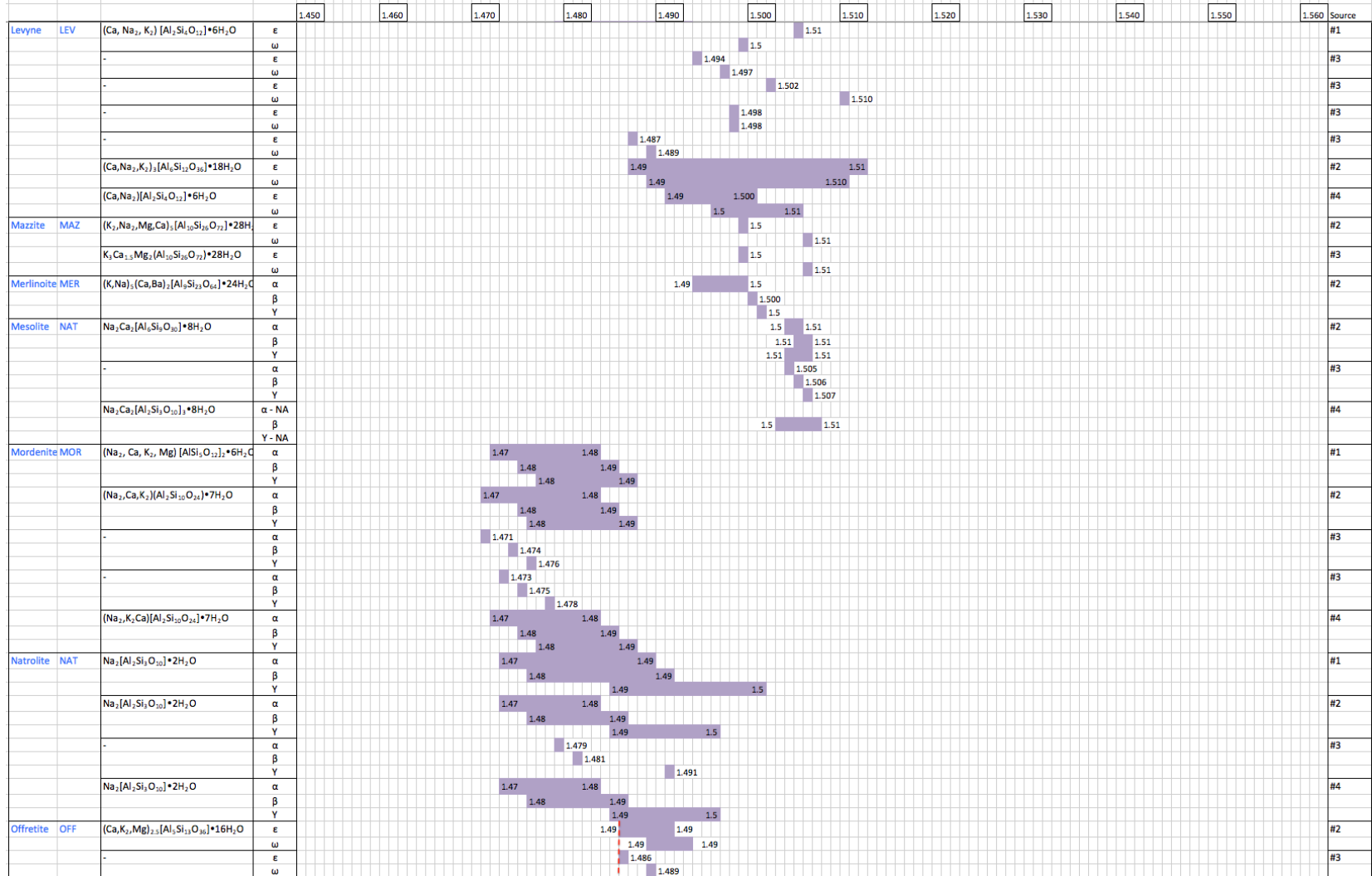
Appendix A: Figure 2



Literature refractive index values for the elongate zeolites (Deer et al, 1967; Tröger et al, 1979; Gottardi and Galli, 1985; Tschernich, 1992).

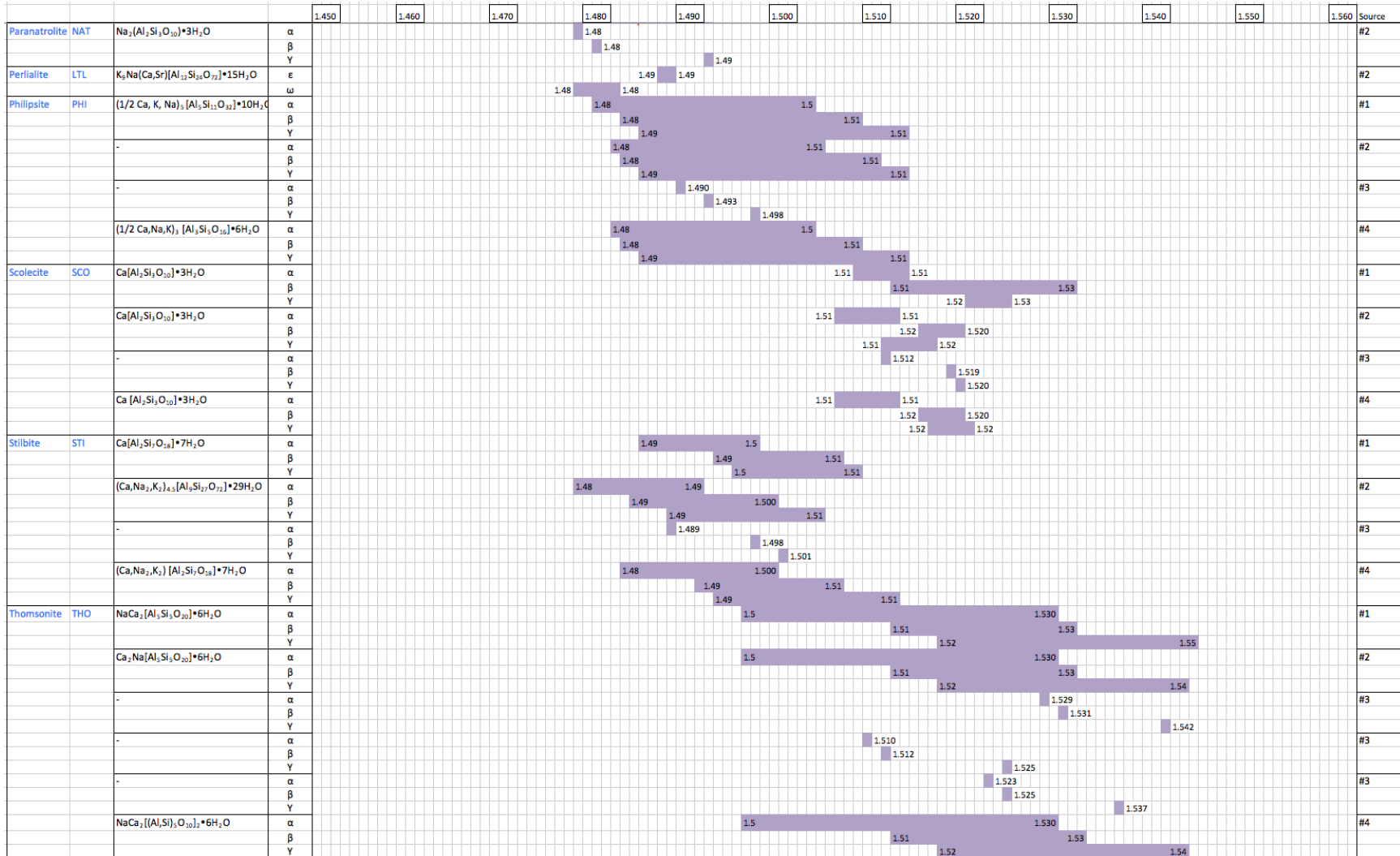


Appendix A: Figure 3



Literature refractive index values for the elongate zeolites (Deer et al, 1967; Tröger et al, 1979; Gottardi and Galli, 1985; Tschernich, 1992).

Appendix A: Figure 4



Literature refractive index values for the elongate zeolites (Deer et al, 1967; Tröger et al, 1979; Gottardi and Galli, 1985; Tschernich, 1992).

Appendix B: Figure 1

|                                | 1a        | 1_Extra       | 1_Extra_1     | 2_Extra | 2_Extra_1 | 3             | 3a            | 3_Extra       | 3_Extra_1     | 4     | 9             | 9_Extra | 9_Extra_1 |
|--------------------------------|-----------|---------------|---------------|---------|-----------|---------------|---------------|---------------|---------------|-------|---------------|---------|-----------|
| SiO <sub>2</sub>               | 57.38     | 57.52         | 58.47         | 59.17   | 58.25     | 58.93         | 58.61         | 57.45         | 59.56         | 62.33 | 58.85         | 59.77   | 58.91     |
| Al <sub>2</sub> O <sub>3</sub> | 16.60     | 17.04         | 17.32         | 17.57   | 17.28     | 17.89         | 17.29         | 16.77         | 17.65         | 16.57 | 17.55         | 17.22   | 17.26     |
| Fe <sub>2</sub> O <sub>3</sub> | -         | -             | -             | -       | -         | -             | -             | -             | -             | -     | 0.14          | 0.13    | 0.14      |
| MgO                            | 1.04      | 1.33          | 0.71          | 2.03    | 2.06      | 1.63          | 0.80          | 1.24          | 1.33          | 0.84  | 1.88          | 1.75    | 1.94      |
| CaO                            | 5.31      | 5.21          | 5.86          | 4.22    | 4.13      | 4.83          | 5.92          | 4.95          | 5.07          | 3.60  | 4.56          | 4.43    | 4.24      |
| SrO                            | 0.14      | 0.12          | 0.16          | 0.09    | 0.09      | 0.12          | 0.19          | 0.16          | 0.12          | 0.09  | 0.09          | 0.09    | -         |
| BaO                            | -         | -             | -             | -       | 0.05      | -             | -             | -             | 0.05          | -     | 0.13          | 0.13    | 0.12      |
| Na <sub>2</sub> O              | 0.09      | 0.12          | 0.07          | 0.10    | 0.13      | 0.20          | -             | 0.35          | 0.17          | 0.62  | 0.09          | 0.07    | -         |
| K <sub>2</sub> O               | 3.19      | 3.31          | 3.18          | 3.46    | 3.35      | 3.61          | 3.32          | 3.41          | 3.52          | 4.77  | 3.57          | 3.38    | 3.58      |
| H <sub>2</sub> O*              | 16.26     | 15.42         | 14.27         | 13.44   | 14.76     | 12.84         | 13.82         | 15.69         | 12.59         | 11.18 | 13.23         | 13.06   | 13.75     |
| Si                             | 26.91     | 26.73         | 26.81         | 26.75   | 26.75     | 26.59         | 26.78         | 26.81         | 26.77         | 27.72 | 26.65         | 26.93   | 26.80     |
| Al                             | 9.17      | 9.33          | 9.36          | 9.37    | 9.36      | 9.52          | 9.31          | 9.22          | 9.35          | 8.48  | 9.37          | 9.15    | 9.26      |
| Fe                             | -         | -             | -             | -       | -         | -             | -             | -             | -             | -     | 0.05          | 0.05    | 0.05      |
| Mg                             | 0.73      | 0.93          | 0.48          | 1.37    | 1.41      | 1.10          | 0.55          | 0.87          | 0.90          | 0.54  | 1.28          | 1.17    | 1.31      |
| Ca                             | 2.67      | 2.59          | 2.88          | 2.05    | 2.03      | 2.33          | 2.90          | 2.47          | 2.44          | 1.72  | 2.21          | 2.14    | 2.07      |
| Sr                             | 0.04      | -             | 0.04          | -       | 0.02      | -             | 0.05          | 0.04          | 0.03          | 0.02  | -             | 0.02    | -         |
| Ba                             | -         | -             | -             | -       | -         | -             | -             | -             | -             | -     | 0.02          | 0.02    | 0.02      |
| Na                             | 0.08      | -             | -             | -       | -         | -             | -             | 0.31          | -             | 0.53  | -             | -       | -         |
| K                              | 1.91      | 1.96          | 1.86          | 2.00    | 1.96      | 2.08          | 1.94          | 2.03          | 2.02          | 2.58  | 2.06          | 1.94    | 2.08      |
| H <sub>2</sub> O               | 13.10     | 12.23         | 11.18         | 10.34   | 11.53     | 9.90          | 10.80         | 12.53         | 9.67          | 8.90  | 10.32         | 10.02   | 10.67     |
| Points Per Grain               | 3         | 4             | 3             | 3       | 3.00      | 3.00          | 2.00          | 3.00          | 4.00          | 2.00  | 3             | 3       | 3         |
| E%                             | 3.67      | 2.52          | 7.72          | 5.36    | 4.64      | 4.61          | 4.35          | 1.36          | 5.43          | 10.45 | 0.03          | 0.06    | 0.05      |
| R-value                        | 0.746     | 0.741         | 0.741         | 0.741   | 0.741     | 0.736         | 0.742         | 0.744         | 0.741         | 0.766 | 0.740         | 0.746   | 0.743     |
| a (Å <sup>3</sup> )            | 13.31     |               |               | 12.84   |           | 13.31         |               |               |               | 13.26 | 13.39         |         |           |
| c (Å <sup>3</sup> )            | 15.15     |               |               | 14.66   |           | 15.14         |               |               |               | 15.06 | 15.22         |         |           |
| V (Å <sup>3</sup> )            | 2325      |               |               | 2091    |           | 2325          |               |               |               | 2295  | 2362          |         |           |
| Sign of Elongation             | L.S./L.F. | L.S. and L.F. | L.S. and L.F. | L.S.    | L.S.      | L.S. and L.F. | L.S. and L.F. | L.S. and L.F. | L.S. and L.F. | L.S.  | L.S. and L.F. | L.S.    | L.S.      |

Erionite samples used in this study showing average chemistry per grain. H<sub>2</sub>O\* was calculated by difference with EPMA. E% = Balance Error Calculation (Passaglia, 1970; Passaglia et al, 1998). L.S. = length slow, L.F. = length fast. Numbers in red are samples with Mg > 0.80 (Gualtieri et al, 1998; Dogan and Dogan, 2008; Dogan, 2011).

Appendix B: Figure 2

|                                | 10    | 10a   | 10_Extra_1 | 11a   | 11_Extra_2 | 12        | 12a   | 12b       | 12_Extra_1 | 13a   | 13_Extra_1 | 14    | 14b   | 14_Extra_1 | 15a   | 15b   |
|--------------------------------|-------|-------|------------|-------|------------|-----------|-------|-----------|------------|-------|------------|-------|-------|------------|-------|-------|
| SiO <sub>2</sub>               | 62.94 | 63.85 | 58.20      | 58.68 | 56.43      | 57.12     | 56.47 | 58.07     | 57.27      | 51.40 | 52.44      | 53.36 | 55.04 | 54.51      | 59.02 | 58.85 |
| Al <sub>2</sub> O <sub>3</sub> | 17.72 | 17.25 | 17.74      | 17.26 | 17.62      | 19.58     | 19.27 | 19.37     | 19.17      | 20.40 | 20.78      | 20.49 | 20.83 | 20.61      | 13.65 | 14.61 |
| Fe <sub>2</sub> O <sub>3</sub> | -     | -     | -          | -     | -          | -         | 0.04  | 0.08      | 0.06       | -     | -          | -     | -     | -          | 0.09  | 0.05  |
| MgO                            | 1.46  | 0.80  | 2.09       | 1.62  | 2.49       | 1.24      | 0.98  | 1.29      | 1.34       | 2.84  | 2.31       | 3.24  | 3.22  | 3.02       | 0.48  | 0.56  |
| CaO                            | 4.41  | 4.84  | 4.31       | 4.83  | 4.00       | 6.41      | 6.65  | 6.11      | 5.89       | 4.54  | 5.47       | 4.38  | 4.31  | 4.52       | 4.98  | 4.77  |
| SrO                            | 0.08  | 0.11  | 0.06       | 0.13  | -          | 0.15      | 0.21  | 0.16      | 0.16       | 0.16  | 0.23       | 0.10  | 0.08  | 0.13       | -     | 0.05  |
| BaO                            | 0.21  | 0.26  | 0.13       | 0.05  | -          | 0.05      | 0.04  | 0.06      | 0.04       | 0.15  | 0.18       | 0.08  | 0.09  | 0.11       | -     | -     |
| Na <sub>2</sub> O              | 0.22  | 0.09  | -          | -     | -          | -         | -     | -         | 0.06       | 0.06  | -          | 0.06  | 0.17  | 0.18       | 0.15  | 0.20  |
| K <sub>2</sub> O               | 3.82  | 4.01  | 3.39       | 3.23  | 3.32       | 3.28      | 3.27  | 3.36      | 3.38       | 3.08  | 2.89       | 3.46  | 3.48  | 3.41       | 3.68  | 3.42  |
| H <sub>2</sub> O*              | 9.27  | 8.83  | 14.08      | 14.23 | 16.08      | 12.16     | 13.12 | 11.53     | 12.72      | 17.40 | 15.70      | 14.84 | 12.90 | 13.59      | 17.99 | 17.56 |
| Si                             | 26.94 | 27.47 | 26.57      | 26.80 | 26.36      | 25.74     | 25.76 | 25.94     | 25.93      | 24.65 | 24.68      | 24.81 | 24.97 | 24.97      | 28.19 | 27.91 |
| Al                             | 9.25  | 8.75  | 9.54       | 9.29  | 9.70       | 10.40     | 10.36 | 10.20     | 10.23      | 11.54 | 11.53      | 11.24 | 11.14 | 11.13      | 7.68  | 8.16  |
| Fe                             | -     | -     | -          | -     | -          | -         | -     | -         | -          | -     | -          | -     | -     | -          | -     | -     |
| Mg                             | 1.11  | 0.51  | 1.42       | 1.11  | 1.73       | 0.83      | 0.67  | 0.86      | 0.90       | 2.03  | 1.62       | 2.25  | 2.18  | 2.06       | 0.34  | 0.40  |
| Ca                             | 2.03  | 2.23  | 2.11       | 2.36  | 2.00       | 3.09      | 3.25  | 2.92      | 2.85       | 2.34  | 2.76       | 2.19  | 2.10  | 2.22       | 2.55  | 2.42  |
| Sr                             | -     | 0.03  | -          | 0.04  | -          | 0.04      | 0.05  | 0.04      | 0.04       | 0.04  | 0.06       | 0.03  | 0.02  | 0.03       | -     | -     |
| Ba                             | 0.04  | 0.04  | 0.02       | -     | -          | -         | -     | -         | -          | 0.03  | 0.03       | 0.02  | 0.02  | 0.02       | -     | -     |
| Na                             | -     | -     | -          | -     | -          | -         | -     | -         | -          | -     | -          | -     | -     | -          | 0.14  | -     |
| K                              | 2.06  | 2.20  | 1.98       | 1.88  | 1.98       | 1.88      | 1.91  | 1.92      | 1.95       | 1.89  | 1.74       | 2.06  | 2.02  | 1.99       | 2.24  | 2.07  |
| H <sub>2</sub> O               | 7.18  | 6.51  | 10.96      | 11.08 | 12.78      | 9.42      | 10.30 | 8.84      | 9.89       | 14.36 | 12.74      | 11.97 | 10.06 | 10.71      | 14.65 | 14.17 |
| Points Per Grain               | 3     | 4     | 4          | 5     | 2          | 5         | 6     | 6         | 10         | 3     | 4          | 3     | 4     | 2          | 3     | 4     |
| E%                             | 0.09  | 0.11  | 0.05       | 4.44  | 2.72       | 5.88      | 5.21  | 6.63      | 7.06       | 7.10  | 7.81       | 1.89  | 4.33  | 3.62       | -5.58 | 4.01  |
| R-value                        | 0.744 | 0.758 | 0.736      | 0.743 | 0.731      | 0.712     | 0.713 | 0.718     | 0.717      | 0.681 | 0.682      | 0.688 | 0.691 | 0.692      | 0.786 | 0.774 |
| a (Å <sup>3</sup> )            | 13.29 |       |            |       |            |           |       |           |            |       |            |       |       |            |       |       |
| c (Å <sup>3</sup> )            | 15.12 |       |            |       |            |           |       |           |            |       |            |       |       |            |       |       |
| V (Å <sup>3</sup> )            | 2313  |       |            |       |            |           |       |           |            |       |            |       |       |            |       |       |
| Sign of Elongation             | L.S.  | L.S.  | L.S.       | L.S.  | L.S.       | L.S./L.F. | L.F.  | L.S./L.F. | L.S./L.F.  | L.F.  | NA         | L.F.  | L.F.  | L.F.       | L.S.  | L.S.  |

Erionite samples used in this study showing average chemistry per grain. H<sub>2</sub>O\* was calculated by difference with EPMA. E% = Balance Error Calculation (Passaglia, 1970; Passaglia et al, 1998). L.S. = length slow, L.F. = length fast.

Appendix B: Figure 3

|                                | 15_Extra_1 | 16_Extra_1 | 16_Extra_2 | 16_Extra_3 | 17_Extra_1 | 18_Extra_1 | 43b   | 43_Extra | 43_Extra_1 | 45_Extra  | 45_Extra_1 | 45_Extra_2 |
|--------------------------------|------------|------------|------------|------------|------------|------------|-------|----------|------------|-----------|------------|------------|
| SiO <sub>2</sub>               | 59.29      | 60.84      | 62.34      | 60.72      | 59.13      | 58.65      | 60.69 | 60.41    | 62.35      | 59.95     | 59.84      | 58.59      |
| Al <sub>2</sub> O <sub>3</sub> | 15.07      | 12.83      | 15.77      | 15.95      | 14.12      | 13.43      | 16.75 | 16.64    | 16.92      | 17.82     | 17.80      | 17.34      |
| Fe <sub>2</sub> O <sub>3</sub> | 0.04       | 0.04       | –          | –          | –          | 0.92       | BDL   | 0.05     | 0.09       | 0.05      | –          | –          |
| MgO                            | 0.68       | 0.26       | 0.34       | 0.41       | 1.00       | 1.13       | 1.14  | 1.14     | 1.18       | 0.80      | 1.18       | 1.03       |
| CaO                            | 4.68       | 5.29       | 5.56       | 5.74       | 4.22       | 3.76       | 3.58  | 3.73     | 3.86       | 5.97      | 5.42       | 5.62       |
| SrO                            | 0.06       | 0.10       | 0.16       | 0.15       | 0.10       | 0.04       | 0.05  | 0.07     | 0.11       | 0.15      | 0.14       | 0.13       |
| BaO                            | –          | –          | –          | –          | 0.23       | 0.22       | BDL   | –        | BDL        | 0.06      | –          | –          |
| Na <sub>2</sub> O              | 0.13       | 0.04       | 0.18       | 0.06       | 0.16       | 0.06       | 0.61  | 0.54     | 0.79       | 0.09      | 0.29       | 0.05       |
| K <sub>2</sub> O               | 3.05       | 2.80       | 3.07       | 3.19       | 3.11       | 3.28       | 4.46  | 3.83     | 4.18       | 3.48      | 3.48       | 3.27       |
| H <sub>2</sub> O*              | 17.10      | 17.83      | 12.56      | 13.77      | 18.06      | 18.50      | 12.67 | 13.60    | 10.49      | 11.76     | 11.99      | 14.01      |
| Si                             | 27.85      | 28.77      | 27.86      | 27.57      | 28.14      | 28.14      | 27.31 | 27.36    | 27.35      | 26.75     | 26.73      | 26.77      |
| Al                             | 8.34       | 7.14       | 8.27       | 8.53       | 7.89       | 7.60       | 8.88  | 8.89     | 8.75       | 9.37      | 9.38       | 9.34       |
| Fe                             | –          | –          | –          | –          | –          | 0.33       | –     | –        | 0.03       | –         | –          | –          |
| Mg                             | 0.48       | 0.18       | 0.23       | 0.28       | 0.70       | 0.81       | 0.77  | 0.77     | 0.77       | 0.54      | 0.79       | 0.70       |
| Ca                             | 2.36       | 2.68       | 2.66       | 2.79       | 2.15       | 1.93       | 1.73  | 1.81     | 1.82       | 2.85      | 2.59       | 2.75       |
| Sr                             | –          | 0.03       | 0.04       | 0.04       | –          | 0.01       | 0.01  | –        | 0.03       | 0.04      | –          | 0.03       |
| Ba                             | –          | –          | –          | –          | 0.04       | 0.04       | –     | –        | –          | –         | –          | –          |
| Na                             | –          | –          | 0.15       | –          | –          | 0.05       | 0.53  | 0.47     | 0.67       | –         | –          | –          |
| K                              | 1.83       | 1.69       | 1.75       | 1.85       | 1.89       | 2.01       | 2.56  | 2.21     | 2.34       | 1.98      | 1.99       | 1.91       |
| H <sub>2</sub> O               | 13.62      | 14.24      | 9.63       | 10.64      | 14.58      | 15.09      | 9.73  | 10.47    | 7.85       | 8.99      | 9.16       | 10.95      |
| Points Per Grain               | 2          | 2          | 2          | 2          | 3          | 1          | 1     | 5        | 1          | 12        | 12         | 12         |
| E%                             | 10.26      | -4.45      | 6.46       | 5.31       | 1.22       | 3.54       | 9.63  | 13.01    | 6.70       | 5.53      | 4.87       | 5.14       |
| R-value                        | 0.770      | 0.801      | 0.771      | 0.764      | 0.781      | 0.787      | 0.755 | 0.755    | 0.758      | 0.741     | 0.740      | 0.741      |
| a (Å <sup>3</sup> )            |            |            |            |            |            |            |       |          |            |           |            |            |
| c (Å <sup>3</sup> )            |            |            |            |            |            |            |       |          |            |           |            |            |
| V (Å <sup>3</sup> )            |            |            |            |            |            |            |       |          |            |           |            |            |
| Sign of Elongation             | L.S.       | L.F.       | L.S./L.F.  | L.S./L.F.  | L.S.       | L.S.       | L.S.  | L.S.     | L.S.       | L.S./L.F. | L.S./L.F.  | L.S./L.F.  |

Erionite samples used in this study showing average chemistry per grain. H<sub>2</sub>O\* was calculated by difference with EPMA. E% = Balance Error Calculation (Passaglia, 1970; Passaglia et al, 1998). L.S. = length slow, L.F. = length fast.

Appendix B: Figure 4

|                                | 5a    | 5_Extra | 5_Extra_1 | 7b    | 7_Extra | 7_Extra_1 | 29    | 29a   | 29_Extra_1 |
|--------------------------------|-------|---------|-----------|-------|---------|-----------|-------|-------|------------|
| SiO <sub>2</sub>               | 42.26 | 46.63   | 46.82     | 53.51 | 51.42   | 45.99     | 47.03 | 53.95 | 45.92      |
| Al <sub>2</sub> O <sub>3</sub> | 21.08 | 23.44   | 22.21     | 20.21 | 19.71   | 25.73     | 17.19 | 20.03 | 17.22      |
| Fe <sub>2</sub> O <sub>3</sub> | -     | -       | -         | -     | -       | -         | 0.11  | 0.06  | -          |
| MgO                            | -     | 0.03    | -         | 3.21  | 3.16    | -         | 1.00  | 0.59  | 0.47       |
| CaO                            | 9.04  | 11.08   | 10.00     | 4.31  | 4.27    | 9.40      | 5.75  | 6.91  | 6.39       |
| SrO                            | 0.08  | 0.06    | 0.05      | 0.19  | 0.19    | -         | 0.05  | 0.07  | 0.05       |
| BaO                            | -     | -       | -         | 0.04  | 0.05    | -         | 0.14  | 0.10  | 0.09       |
| Na <sub>2</sub> O              | 2.43  | 0.62    | 1.37      | -     | -       | 5.40      | 0.40  | 0.80  | 0.49       |
| K <sub>2</sub> O               | 1.04  | 0.42    | 0.78      | 3.58  | 3.40    | 0.02      | 2.82  | 3.31  | 3.09       |
| H <sub>2</sub> O*              | 24.10 | 17.74   | 18.78     | 14.94 | 17.80   | 13.47     | 25.50 | 14.23 | 26.29      |
| Si                             | 11.31 | 11.38   | 11.58     | 12.46 | 12.40   | 10.84     | 12.59 | 12.56 | 12.49      |
| Al                             | 6.65  | 6.75    | 6.48      | 5.55  | 5.60    | 7.15      | 5.42  | 5.50  | 5.52       |
| Fe                             | -     | -       | -         | -     | -       | -         | 0.02  | -     | -          |
| Mg                             | -     | -       | -         | 1.12  | 1.14    | -         | 0.40  | 0.21  | 0.19       |
| Ca                             | 2.59  | 2.90    | 2.65      | 1.08  | 1.10    | 2.37      | 1.65  | 1.73  | 1.86       |
| Sr                             | -     | -       | -         | 0.03  | 0.03    | -         | 0.01  | -     | -          |
| Ba                             | -     | -       | -         | -     | -       | -         | 0.01  | 0.01  | 0.01       |
| Na                             | 1.26  | 0.29    | 0.66      | -     | -       | 2.47      | 0.21  | 0.36  | 0.26       |
| K                              | 0.35  | 0.13    | 0.25      | 1.06  | 1.05    | -         | 0.96  | 0.98  | 1.07       |
| H <sub>2</sub> O               | 11.36 | 7.55    | 8.13      | 5.99  | 7.39    | 5.61      | 11.82 | 5.78  | 12.50      |
| Points Per Grain               | 2     | 2       | 3         | 5     | 3.00    | 5.00      | 1.00  | 3.00  | 2          |
| E%                             | -2.30 | 8.09    | 4.25      | 0.91  | 0.41    | -0.94     | 2.51  | 5.17  | 0.99       |
| R-value                        | 0.630 | 0.628   | 0.641     | 0.692 | 0.689   | 0.603     | 0.699 | 0.695 | 0.694      |
| a (Å <sup>3</sup> )            | -     | -       | -         | -     | -       | -         | -     | -     | -          |
| c (Å <sup>3</sup> )            | -     | -       | -         | -     | -       | -         | -     | -     | -          |
| V (Å <sup>3</sup> )            | -     | -       | -         | -     | -       | -         | -     | -     | -          |
| Sign of Elongation             | -     | -       | -         | L.F.  | L.F.    | L.S.      | L.F.  | L.F.  | L.F./L.S.  |

Offretite samples used in this study showing average chemistry per grain. H<sub>2</sub>O\* was calculated by difference with EPMA. E% = Balance Error Calculation (Passaglia, 1970; Passaglia et al, 1998). L.S. = length slow, L.F. = length fast.

Appendix B: Figure 5

|                                | 30    | 30a   | 30b   | 30_Extra  | 31        | 31b       | 31_Extra  | 31_Extra_1 | 32a            | 32b       | 32_Extra  | 32_Extra_1 | 33a       | 33b       | 33_Extra  |
|--------------------------------|-------|-------|-------|-----------|-----------|-----------|-----------|------------|----------------|-----------|-----------|------------|-----------|-----------|-----------|
| SiO <sub>2</sub>               | 55.16 | 56.48 | 56.96 | 56.38     | 52.84     | 52.82     | 53.88     | 54.22      | 53.04          | 54.81     | 55.80     | 55.28      | 53.79     | 52.59     | 57.18     |
| Al <sub>2</sub> O <sub>3</sub> | 19.47 | 20.00 | 19.87 | 19.79     | 19.29     | 18.99     | 19.39     | 19.91      | 19.27          | 19.61     | 20.13     | 20.04      | 19.19     | 19.63     | 20.00     |
| Fe <sub>2</sub> O <sub>3</sub> | -     | -     | -     | -         | -         | -         | -         | 0.04       | 0.04           | -         | -         | -          | -         | -         | -         |
| MgO                            | 2.98  | 3.05  | 3.04  | 3.02      | 3.04      | 2.94      | 2.99      | 3.06       | 3.02           | 2.92      | 3.04      | 3.14       | 3.10      | 2.87      | 3.12      |
| CaO                            | 4.10  | 4.15  | 4.16  | 4.16      | 3.92      | 3.94      | 4.10      | 4.10       | 3.93           | 4.14      | 4.22      | 4.12       | 3.24      | 3.37      | 3.39      |
| SrO                            | 0.06  | 0.05  | 0.07  | 0.06      | 0.07      | 0.07      | 0.07      | 0.07       | 0.07           | 0.10      | 0.09      | 0.07       | 0.50      | 0.86      | 0.63      |
| BaO                            | -     | 0.05  | -     | -         | 0.10      | -         | 0.06      | 0.06       | 0.06           | 0.07      | 0.05      | 0.05       | 0.13      | 0.08      | 0.10      |
| Na <sub>2</sub> O              | -     | 0.05  | -     | -         | -         | -         | 0.05      | 0.05       | -              | 0.06      | -         | -          | 0.11      | 0.15      | 0.10      |
| K <sub>2</sub> O               | 3.53  | 3.56  | 3.62  | 3.62      | 3.49      | 3.39      | 3.38      | 3.56       | 3.43           | 3.51      | 3.66      | 3.57       | 3.39      | 3.37      | 3.73      |
| H <sub>2</sub> O*              | 14.70 | 12.70 | 12.30 | 12.96     | 17.35     | 17.85     | 16.15     | 15.06      | 17.22          | 14.92     | 13.04     | 13.75      | 16.65     | 17.16     | 11.82     |
| Si                             | 12.74 | 12.74 | 12.79 | 12.76     | 12.62     | 12.67     | 12.67     | 12.60      | 12.64          | 12.70     | 12.66     | 12.64      | 12.72     | 12.57     | 12.80     |
| Al                             | 5.30  | 5.32  | 5.26  | 5.28      | 5.43      | 5.37      | 5.37      | 5.46       | 5.41           | 5.36      | 5.39      | 5.40       | 5.36      | 5.55      | 5.28      |
| Fe                             | -     | -     | -     | -         | -         | -         | -         | -          | -              | -         | -         | -          | -         | -         | -         |
| Mg                             | 1.02  | 1.03  | 1.02  | 1.02      | 1.08      | 1.05      | 1.05      | 1.06       | 1.07           | 1.01      | 1.03      | 1.07       | 1.10      | 1.03      | 1.04      |
| Ca                             | 1.02  | 1.00  | 1.00  | 1.01      | 1.00      | 1.01      | 1.03      | 1.02       | 1.00           | 1.03      | 1.03      | 1.01       | 0.82      | 0.86      | 0.81      |
| Sr                             | -     | -     | -     | -         | -         | -         | -         | -          | -              | -         | -         | -          | 0.07      | 0.12      | 0.08      |
| Ba                             | -     | -     | -     | -         | -         | -         | -         | -          | -              | -         | -         | -          | -         | -         | -         |
| Na                             | -     | -     | -     | -         | -         | -         | -         | -          | -              | -         | -         | -          | -         | -         | 0.04      |
| K                              | 1.04  | 1.02  | 1.04  | 1.05      | 1.06      | 1.04      | 1.01      | 1.05       | 1.04           | 1.04      | 1.06      | 1.04       | 1.03      | 1.03      | 1.06      |
| H <sub>2</sub> O               | 5.82  | 4.90  | 4.73  | 5.03      | 7.10      | 7.34      | 6.51      | 6.01       | 7.03           | 5.93      | 5.08      | 5.39       | 6.78      | 7.24      | 4.54      |
| Points Per Grain               | 7     | 8     | 5     | 7         | 7         | 7         | 9         | 9          | 5              | 9         | 8         | 9          | 3         | 9         | 4         |
| E%                             | 3.28  | 4.43  | 3.51  | 3.18      | 3.41      | 3.60      | 3.38      | 4.13       | 3.91           | 4.39      | 3.68      | 3.47       | 6.41      | 8.73      | 5.85      |
| R-value                        | 0.706 | 0.705 | 0.709 | 0.707     | 0.699     | 0.702     | 0.702     | 0.698      | 0.700          | 0.703     | 0.702     | 0.701      | 0.703     | 0.694     | 0.708     |
| a (Å <sup>3</sup> )            |       |       |       |           |           |           |           |            |                |           |           |            |           |           |           |
| c (Å <sup>3</sup> )            |       |       |       |           |           |           |           |            |                |           |           |            |           |           |           |
| V (Å <sup>3</sup> )            |       |       |       |           |           |           |           |            |                |           |           |            |           |           |           |
| Sign of Elongation             | L.S.  | L.S.  | L.S.  | L.S./L.F. | L.S./L.F. | L.S./L.F. | L.S./L.F. | L.S./L.F.  | L.F./L.S./L.F. | L.S./L.F. | L.S./L.F. | L.S./L.F.  | L.S./L.F. | L.S./L.F. | L.S./L.F. |

Offretite samples used in this study showing average chemistry per grain. H<sub>2</sub>O\* was calculated by difference with EPMA. E% = Balance Error Calculation (Passaglia, 1970; Passaglia et al, 1998). L.S. = length slow, L.F. = length fast.

Appendix B: Figure 6

|                           | <b>39</b> | <b>39a</b> | <b>39b</b> | <b>39_Extra</b> |
|---------------------------|-----------|------------|------------|-----------------|
| <b>SiO2</b>               | 45.14     | 45.33      | 42.27      | 44.00           |
| <b>Al2O3</b>              | 25.79     | 25.92      | 24.14      | 25.10           |
| <b>Fe2O3</b>              | –         | –          | –          | –               |
| <b>MgO</b>                | –         | –          | 0.01       | –               |
| <b>CaO</b>                | 13.94     | 14.17      | 12.42      | 13.01           |
| <b>SrO</b>                | 0.08      | –          | 0.05       | –               |
| <b>BaO</b>                | 0.05      | –          | –          | –               |
| <b>Na2O</b>               | 0.07      | –          | 0.07       | 0.05            |
| <b>K2O</b>                | –         | –          | –          | –               |
| <b>H2O*</b>               | 15.06     | 14.56      | 21.09      | 17.86           |
| <b>Si</b>                 | 23.94     | 23.91      | 24.05      | 24.05           |
| <b>Al</b>                 | 16.12     | 16.12      | 16.20      | 16.18           |
| <b>Fe</b>                 | –         | –          | –          | –               |
| <b>Mg</b>                 | –         | –          | –          | –               |
| <b>Ca</b>                 | 7.92      | 8.01       | 7.58       | 7.61            |
| <b>Sr</b>                 | –         | –          | –          | –               |
| <b>Ba</b>                 | –         | –          | –          | –               |
| <b>Na</b>                 | –         | –          | –          | –               |
| <b>K</b>                  | –         | –          | –          | –               |
| <b>H2O</b>                | 14.05     | 13.51      | 21.35      | 17.19           |
| <b>Points Per Grain</b>   | 7         | 6          | 4          | 7               |
| <b>R-value</b>            | 0.598     | 0.597      | 0.598      | 0.598           |
| <b>E%</b>                 | 1.48      | 0.60       | 6.56       | 6.28            |
| <b>Sign of Elongation</b> | L.F.      | L.F.       | L.F.       | L.F.            |

Scolecite samples used in this study showing average chemistry per grain. H<sub>2</sub>O\* was calculated by difference with EPMA. E% = Balance Error Calculation (Passaglia, 1970; Passaglia et al, 1998). L.S. = length slow, L.F. = length fast.



Appendix B: Figure 7

|                                | 24_24 | 24_24b | 24_Extra_1 | 24_Extra_2 | 25_Extra_1 | 25_Extra_2 | 26_26 | 26_26a | 26_26b | 26_Extra_1 | 27_27a | 27_27b | 27_Extra_1 |
|--------------------------------|-------|--------|------------|------------|------------|------------|-------|--------|--------|------------|--------|--------|------------|
| SiO <sub>2</sub>               | 44.66 | 38.59  | 39.20      | 42.48      | 44.06      | 42.76      | 47.04 | 46.70  | 46.63  | 45.85      | 46.84  | 35.65  | 46.02      |
| Al <sub>2</sub> O <sub>3</sub> | 26.34 | 23.30  | 23.37      | 24.18      | 25.47      | 18.10      | 26.39 | 26.33  | 26.15  | 25.93      | 26.70  | 22.19  | 26.39      |
| Fe <sub>2</sub> O <sub>3</sub> | -     | -      | -          | -          | -          | 0.05       | 0.06  | 0.05   | -      | -          | -      | BDL    | -          |
| MgO                            | 0.11  | 0.05   | 0.03       | 0.10       | 0.05       | 0.01       | -     | -      | -      | -          | -      | 0.02   | -          |
| CaO                            | 1.30  | 0.65   | 0.30       | 0.25       | 2.31       | 4.06       | 0.04  | 0.03   | 0.06   | 0.04       | 0.10   | 0.24   | 0.63       |
| SrO                            | 0.36  | 0.08   | 0.04       | 0.06       | -          | -          | -     | 0.04   | -      | 0.36       | 0.05   | BDL    | 0.05       |
| BaO                            | -     | BDL    | -          | -          | -          | -          | -     | -      | -      | 0.04       | -      | BDL    | 0.04       |
| Na <sub>2</sub> O              | 13.66 | 14.07  | 14.12      | 14.99      | 12.80      | 6.67       | 15.74 | 15.98  | 15.92  | 15.75      | 15.78  | 14.12  | 14.98      |
| K <sub>2</sub> O               | -     | BDL    | -          | 0.05       | 0.02       | 0.15       | 0.03  | 0.03   | -      | 0.02       | -      | 0.17   | 0.02       |
| H <sub>2</sub> O*              | 13.75 | 23.24  | 22.93      | 17.95      | 15.33      | 28.29      | 10.78 | 10.95  | 11.27  | 12.45      | 10.56  | 27.57  | 11.96      |
| Si                             | 23.70 | 23.24  | 23.44      | 23.81      | 23.79      | 26.48      | 24.12 | 24.03  | 24.07  | 23.99      | 23.98  | 22.88  | 23.92      |
| Al                             | 16.49 | 16.54  | 16.47      | 15.98      | 16.22      | 13.44      | 15.95 | 15.97  | 15.92  | 16.00      | 16.11  | 16.79  | 16.17      |
| Fe                             | -     | -      | -          | -          | -          | -          | -     | -      | -      | -          | -      | -      | -          |
| Mg                             | -     | 0.04   | 0.02       | 0.09       | -          | -          | -     | -      | -      | -          | -      | 0.02   | -          |
| Ca                             | 0.76  | 0.42   | 0.19       | 0.15       | 1.54       | 2.63       | -     | -      | -      | -          | 0.05   | 0.16   | 0.35       |
| Sr                             | -     | 0.03   | -          | -          | -          | -          | -     | -      | -      | -          | -      | -      | -          |
| Ba                             | -     | -      | -          | -          | -          | -          | -     | -      | -      | -          | -      | -      | -          |
| Na                             | 13.98 | 16.44  | 16.38      | 16.30      | 13.08      | 8.41       | 15.65 | 15.94  | 15.94  | 15.99      | 15.66  | 17.58  | 15.10      |
| K                              | -     | -      | -          | 0.03       | -          | -          | -     | -      | -      | -          | -      | 0.14   | -          |
| H <sub>2</sub> O               | 13.19 | 25.17  | 24.62      | 18.52      | 15.39      | 31.00      | 9.85  | 10.06  | 10.39  | 11.70      | 9.64   | 31.96  | 11.09      |
| Points Per Grain               | 3     | 1      | 2          | 3          | 4          | 2          | 6     | 7      | 5      | 9          | 8      | 1      | 8          |
| R-value                        | 0.590 | 0.584  | 0.587      | 0.598      | 0.595      | 0.663      | 0.602 | 0.601  | 0.602  | 0.600      | 0.598  | 0.577  | 0.597      |
| E%                             | 4.99  | -5.06  | -2.10      | -4.97      | 0.57       | -1.39      | 1.93  | 0.17   | -0.26  | -0.18      | 2.20   | -7.16  | 2.28       |
| Sign of Elongation             | L.S.  | L.S.   | L.S.       | L.S.       | L.S.       | L.S.       | L.S.  | L.S.   | L.S.   | L.S.       | L.S.   | L.S.   | L.S.       |

Natrolite samples used in this study showing average chemistry per grain. H<sub>2</sub>O\* was calculated by difference with EPMA. E% = Balance Error Calculation (Passaglia, 1970; Passaglia et al, 1998). L.S. = length slow, L.F. = length fast.

Appendix B: Figure 8

|                                | 10_Extra_1 | 21_21b         | 21_Extra_2 | 23_23b |                                | 19_Extra_1 | 19_Extra_2 |
|--------------------------------|------------|----------------|------------|--------|--------------------------------|------------|------------|
| SiO <sub>2</sub>               | 50.17      | 55.59          | 50.77      | 42.99  | SiO <sub>2</sub>               | 53.94      | 53.82      |
| Al <sub>2</sub> O <sub>3</sub> | 14.80      | 15.93          | 15.32      | 24.51  | Al <sub>2</sub> O <sub>3</sub> | 18.85      | 18.07      |
| Fe <sub>2</sub> O <sub>3</sub> | –          | –              | 0.10       | 0.22   | Fe <sub>2</sub> O <sub>3</sub> | –          | –          |
| MgO                            | 0.89       | 0.73           | 1.50       | 0.03   | MgO                            | 3.22       | 3.26       |
| CaO                            | 3.41       | 4.61           | 4.34       | 9.39   | CaO                            | 2.81       | 2.75       |
| SrO                            | 0.07       | 0.09           | 0.07       | BDL    | SrO                            | 0.10       | 0.08       |
| BaO                            | –          | 0.20           | 0.10       | BDL    | BaO                            | –          | –          |
| Na <sub>2</sub> O              | 2.00       | 0.71           | 0.59       | 5.62   | Na <sub>2</sub> O              | 0.12       | 0.10       |
| K <sub>2</sub> O               | 2.83       | 3.13           | 2.82       | 0.03   | K <sub>2</sub> O               | 4.39       | 4.35       |
| H <sub>2</sub> O*              | 25.82      | 19.00          | 24.59      | 17.23  | H <sub>2</sub> O*              | 16.58      | 17.54      |
| Si                             | 89.01      | 90.01          | 88.38      | 71.08  | Si                             | 25.55      | 25.78      |
| Al                             | 30.95      | 30.43          | 31.44      | 47.77  | Al                             | 10.53      | 10.20      |
| Fe                             | –          | –              | –          | 0.28   | Fe                             | –          | –          |
| Mg                             | 2.35       | 1.77           | 3.83       | 0.08   | Mg                             | 2.27       | 2.33       |
| Ca                             | 6.48       | 8.02           | 8.12       | 16.63  | Ca                             | 1.43       | 1.41       |
| Sr                             | 0.07       | 0.09           | 0.07       | –      | Sr                             | 0.03       | 0.02       |
| Ba                             | –          | 0.12           | –          | –      | Ba                             | –          | –          |
| Na                             | 6.89       | 2.22           | –          | 18.03  | Na                             | 0.11       | 0.10       |
| K                              | 6.39       | 6.48           | 6.24       | 0.07   | K                              | 2.66       | 2.66       |
| H <sub>2</sub> O               | 78.88      | 52.75          | 73.81      | 50.67  | H <sub>2</sub> O               | 13.49      | 14.42      |
| <b>Points Per Grain</b>        | 3          | 2              | 4          | 1      | <b>Points Per Grain</b>        | 4          | 5          |
| <b>R-value</b>                 | 0.742      | 0.747          | 0.738      | 0.598  | <b>R-value</b>                 | 0.708      | 0.716      |
| <b>E%</b>                      | –0.08      | 6.12           | –1.07      | –6.74  | <b>E%</b>                      | 3.10       | –0.69      |
| <b>Sign of Elongation</b>      | L.S.       | L.S. /<br>L.F. | L.S. /L.F. | L.F.   | <b>Sign of Elongation</b>      | L.F.       | L.F.       |

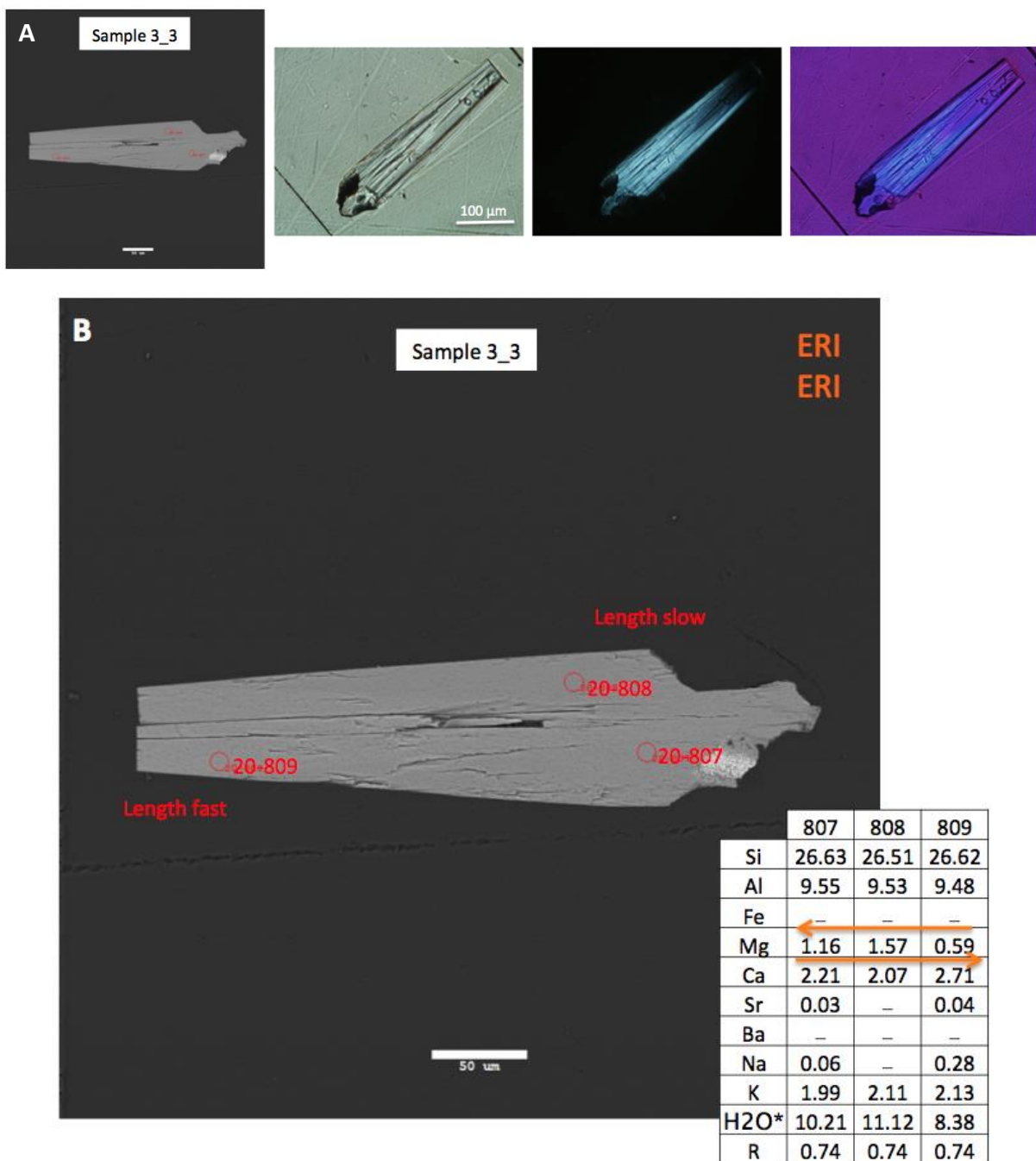
Mesolite samples (left) and Mazzite samples (right) used in this study showing average chemistry per grain. H<sub>2</sub>O\* was calculated by difference with EPMA. E% = Balance Error Calculation (Passaglia, 1970; Passaglia et al, 1998). L.S. = length slow, L.F. = length fast.

Appendix B: Figure 9

|                                | <b>42_42a</b> | <b>42_Extra</b> | <b>42_Extra_1</b> |
|--------------------------------|---------------|-----------------|-------------------|
| SiO <sub>2</sub>               | 39.38         | 38.47           | 38.90             |
| Al <sub>2</sub> O <sub>3</sub> | 30.11         | 28.14           | 29.76             |
| Fe <sub>2</sub> O <sub>3</sub> | –             | 0.04            | 0.05              |
| MgO                            | 0.01          | –               | –                 |
| CaO                            | 11.98         | 10.58           | 12.03             |
| SrO                            | –             | 0.05            | –                 |
| BaO                            | –             | –               | –                 |
| Na <sub>2</sub> O              | 4.83          | 5.07            | 4.70              |
| K <sub>2</sub> O               | –             | 0.02            | –                 |
| H <sub>2</sub> O*              | 13.69         | 17.68           | 14.58             |
| Si                             | 21.07         | 21.53           | 21.04             |
| Al                             | 18.99         | 18.57           | 18.98             |
| Fe                             | –             | –               | –                 |
| Mg                             | –             | –               | –                 |
| Ca                             | 6.87          | 6.32            | 6.98              |
| Sr                             | –             | –               | –                 |
| Ba                             | –             | –               | –                 |
| Na                             | 5.01          | 5.51            | 4.93              |
| K                              | –             | –               | –                 |
| H <sub>2</sub> O               | 13.17         | 18.06           | 14.20             |
| <b>Points Per Grain</b>        | <b>4</b>      | <b>8</b>        | <b>3</b>          |
| <b>R-value</b>                 | <b>0.526</b>  | <b>0.537</b>    | <b>0.526</b>      |
| <b>E%</b>                      | <b>1.29</b>   | <b>2.41</b>     | <b>0.53</b>       |
| <b>Sign of Elongation</b>      | <b>L.S.</b>   | <b>L.F.</b>     | <b>L.F.</b>       |

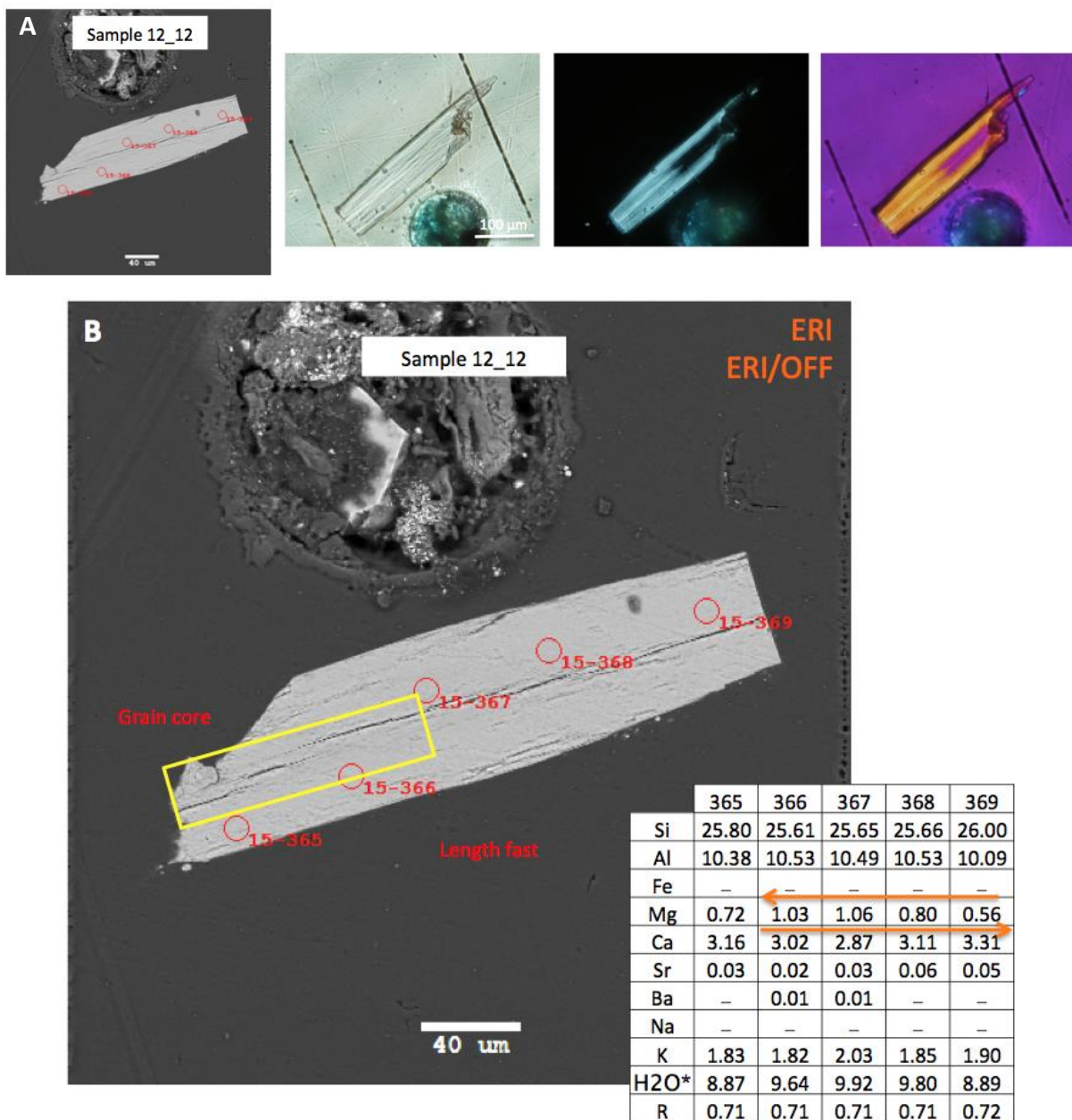
Thomsonite samples used in this study showing average chemistry per grain. H<sub>2</sub>O\* was calculated by difference with EPMA. E% = Balance Error Calculation (Passaglia, 1970; Passaglia et al, 1998). L.S. = length slow, L.F. = length fast.

Appendix C: Figure 1



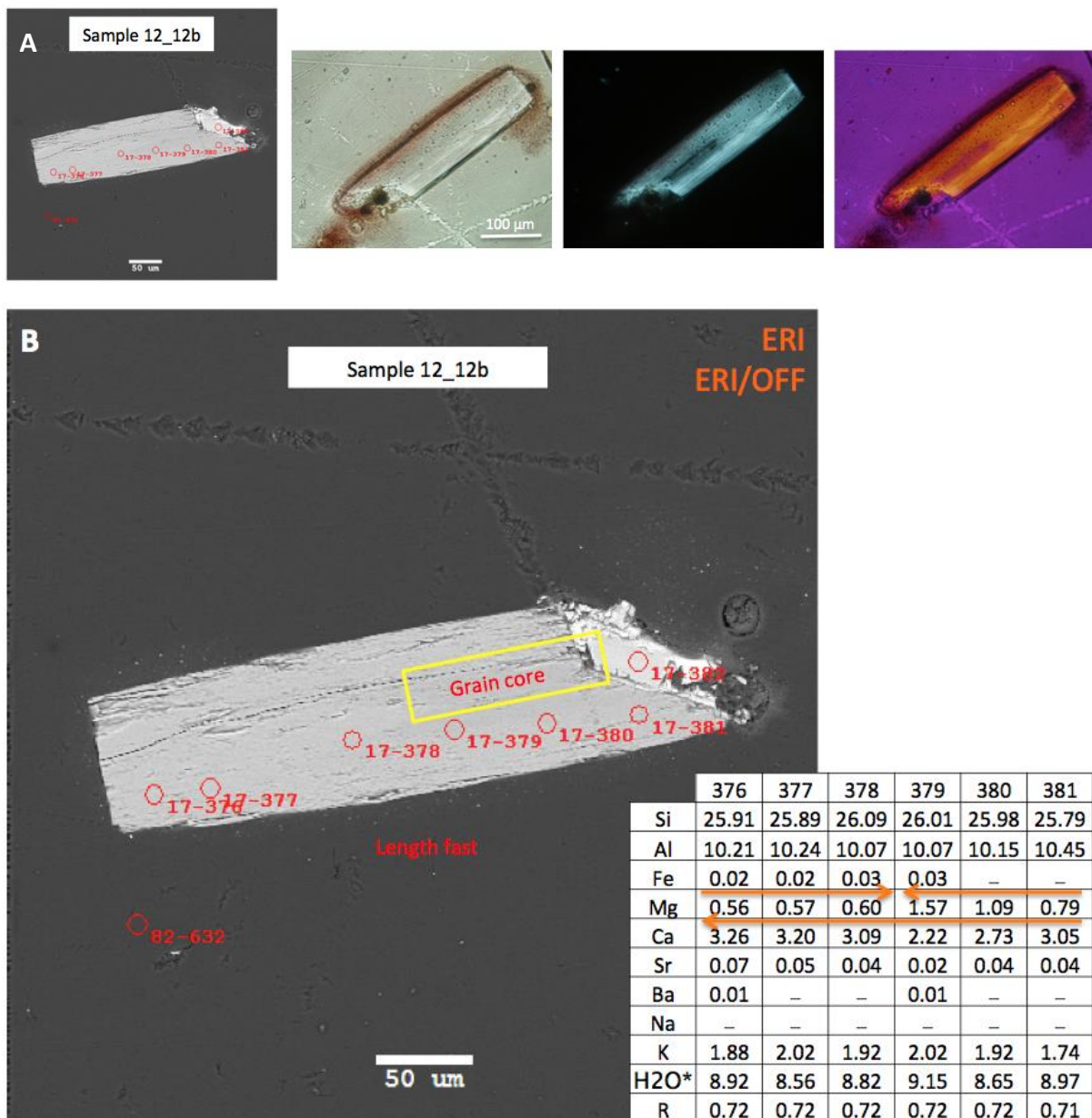
(A) BSE and PLM images of sample 3 of erionite-K from Phelps Dodge Co. Well No. 1, Little Ajo Mtns, Ajo District, Pima County, AZ, USA (B) BSE image along with associated APFU data.

## Appendix C: Figure 2



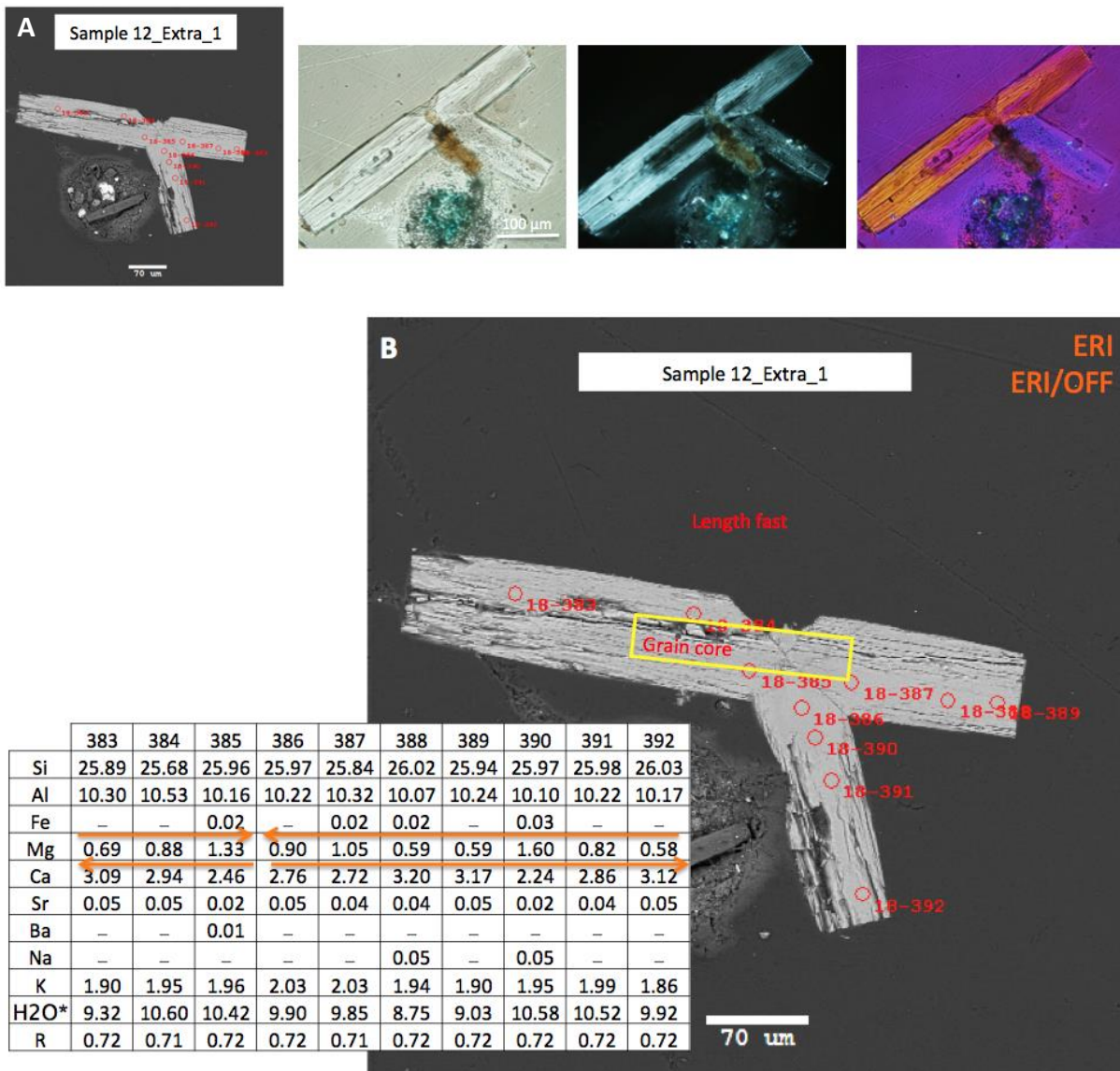
(A) BSE and PLM images of sample 3 of erionite from Eureka Valley, Del Norte Co, California, USA (B) BSE image along with associated APFU data.

## Appendix C: Figure 3



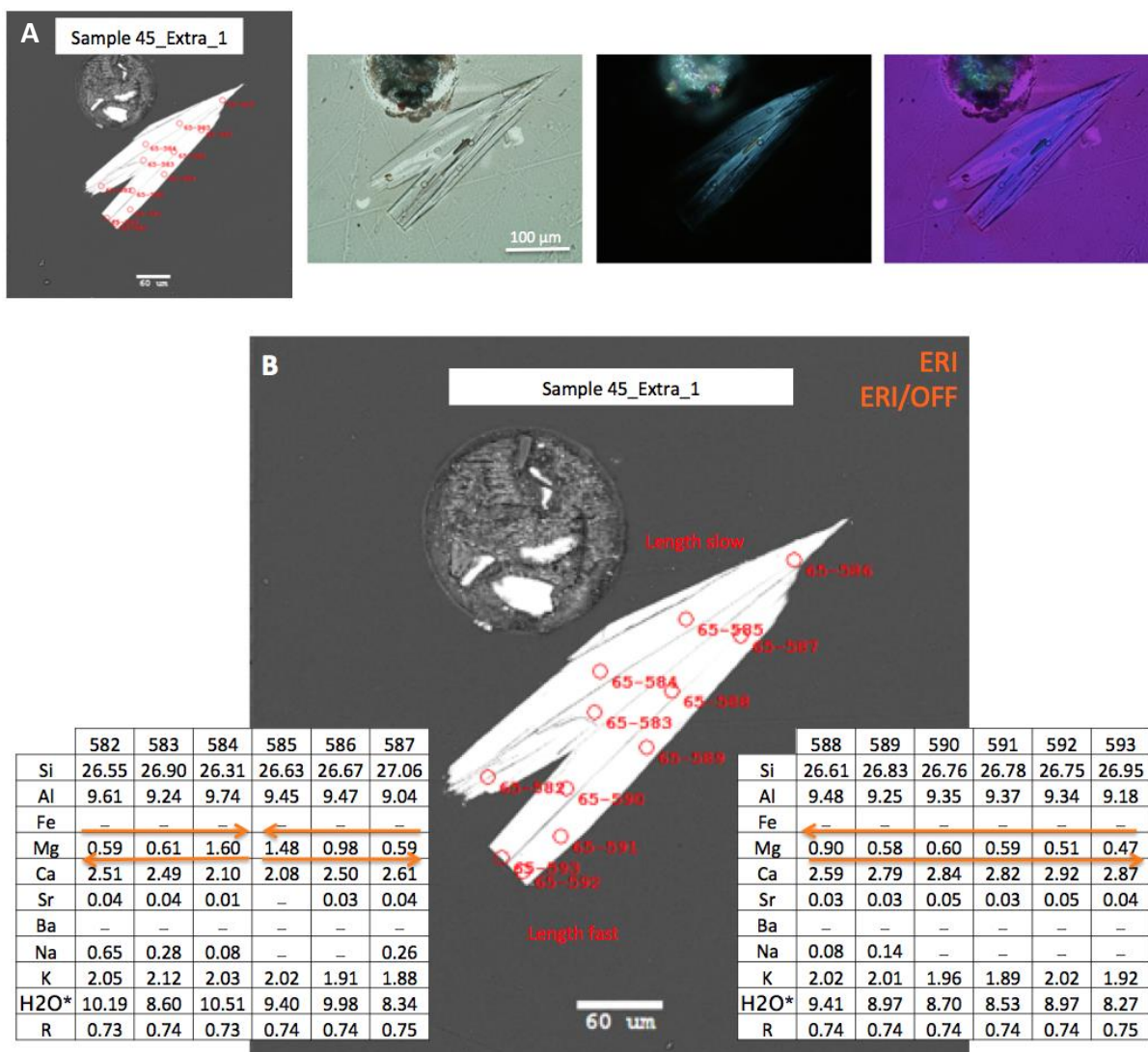
(A) BSE and PLM images of sample 3 of erionite from Eureka Valley, Del Norte Co, California, USA (B) BSE image along with associated APFU data.

Appendix C: Figure 4



(A) BSE and PLM images of sample 3 of erionite from Eureka Valley, Del Norte Co, California, USA (B) BSE image along with associated APFU data.

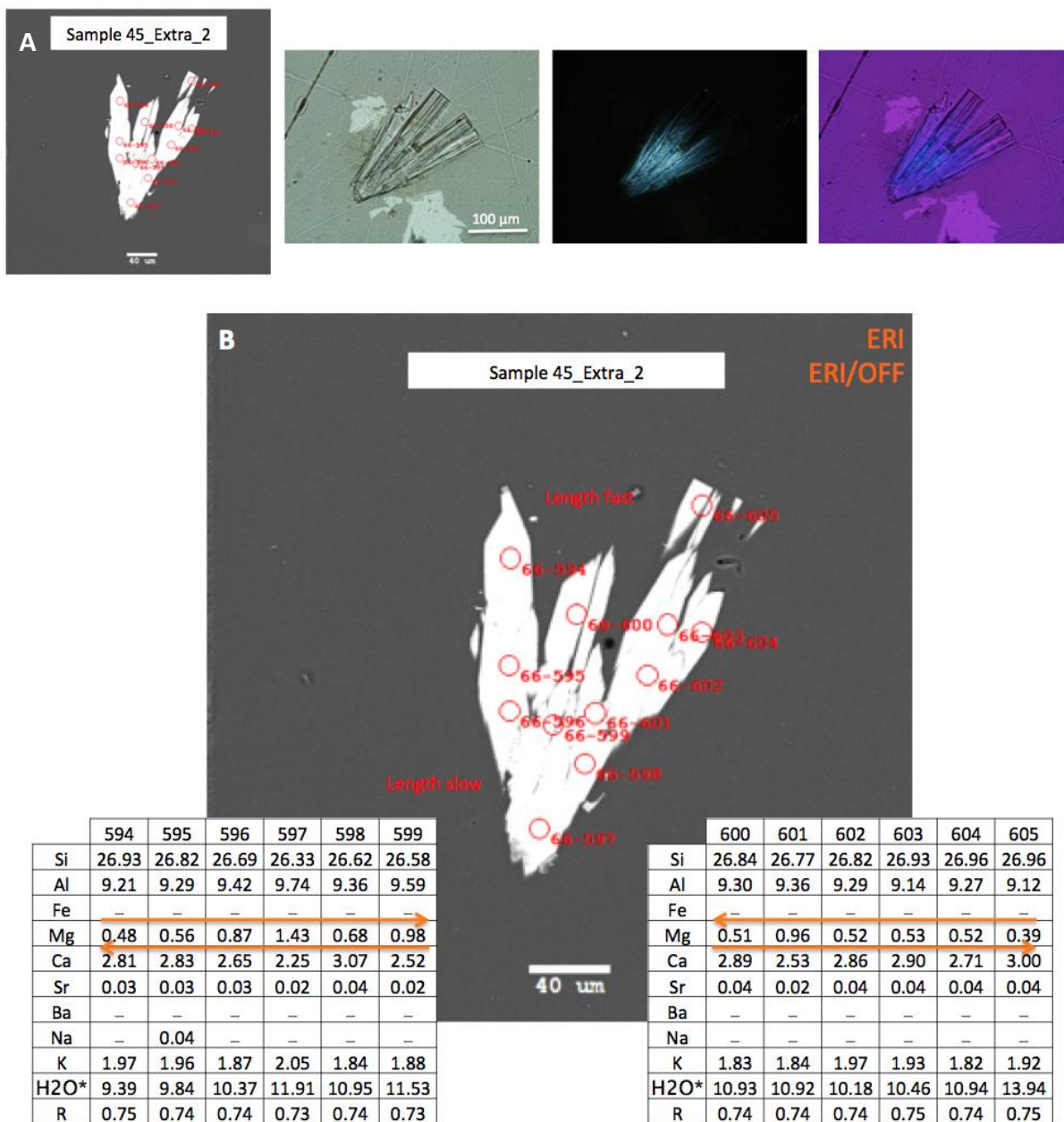
Appendix C: Figure 5



(A) BSE and PLM images of sample 3 of erionite-Ca from Phelps Dodge Co. Well No. 1, Little Ajo Mtns, Ajo District, Pima County, AZ, USA (B) BSE image along with associated APFU data.

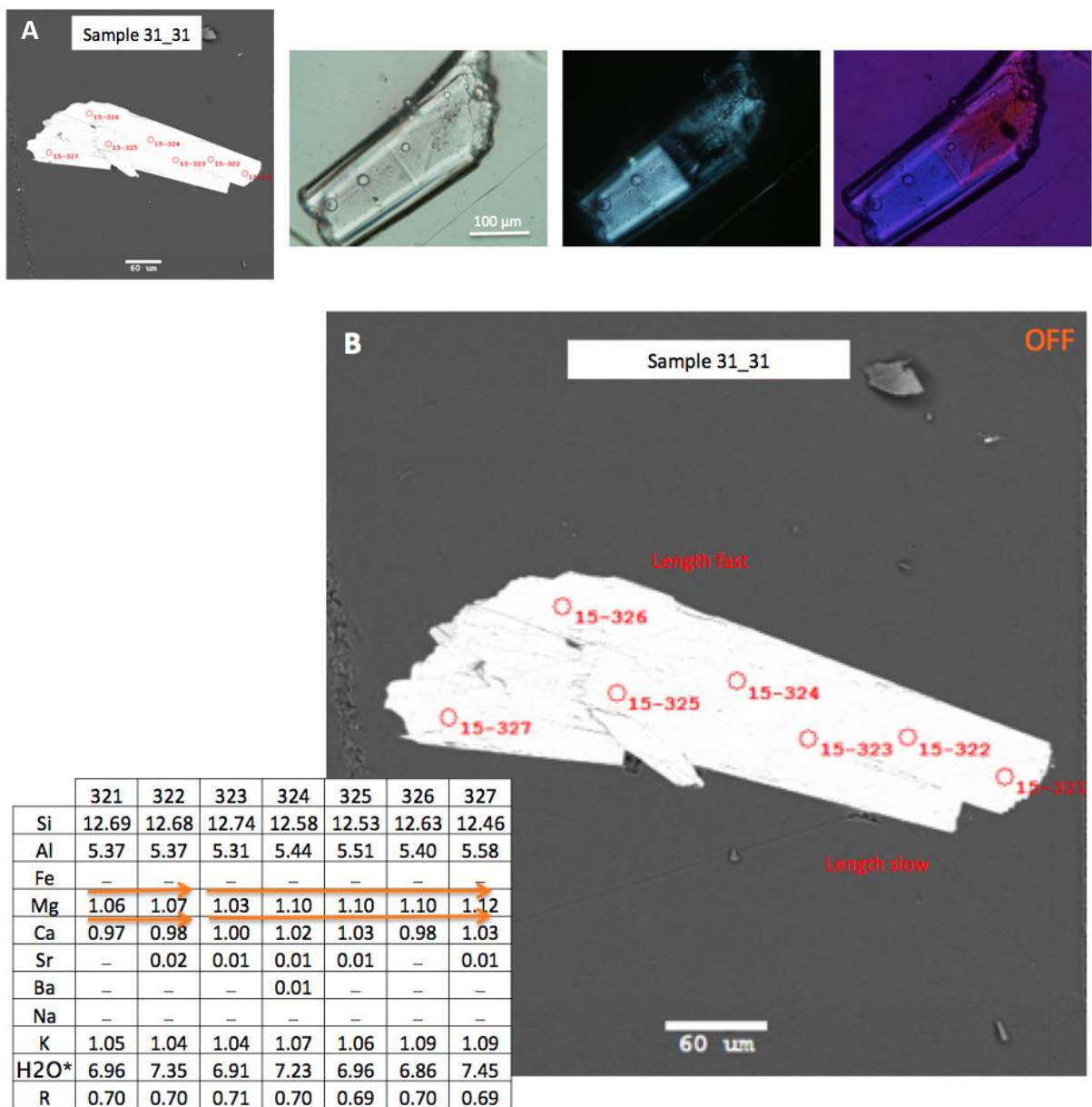


Appendix C: Figure 6



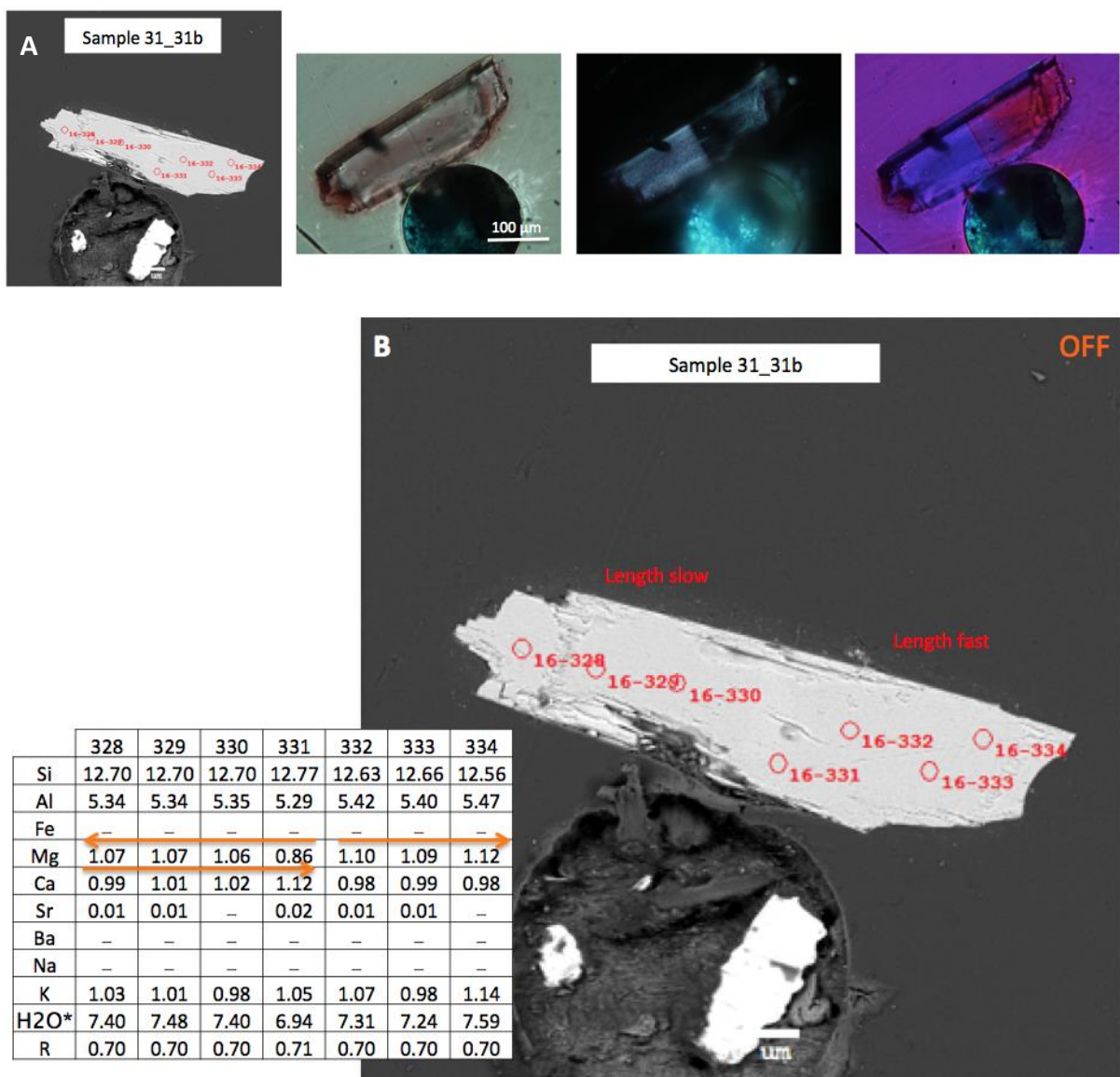
(A) BSE and PLM images of sample 3 of erionite-K from Phelps Dodge Co. Well No. 1, Little Ajo Mtns, Ajo District, Pima County, AZ, USA (B) BSE image along with associated APFU data.

## Appendix C: Figure 7



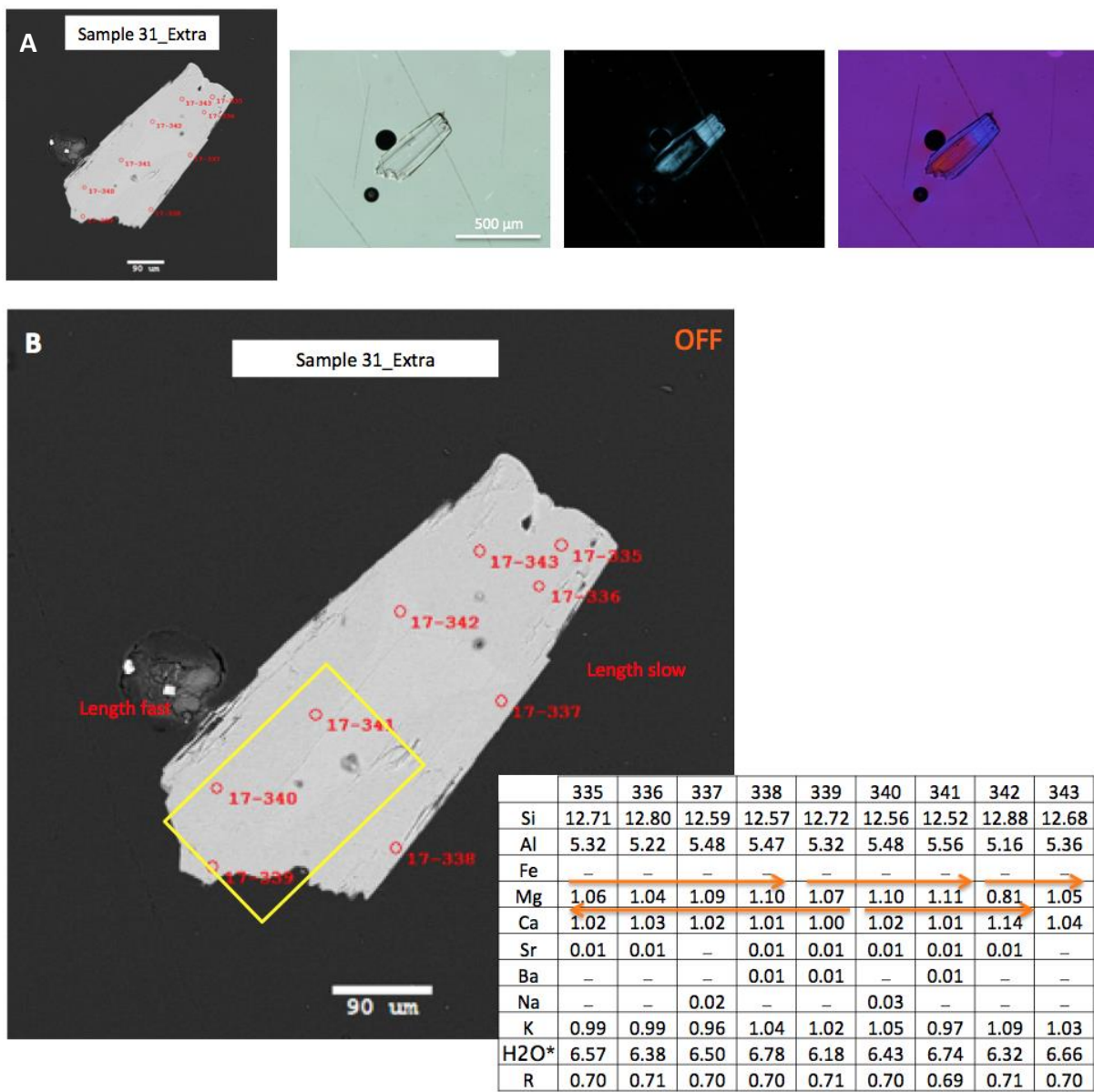
(A) BSE and PLM images of sample 3 of offretite from Mt. Simiouse, Loire, France  
 (B) BSE image along with associated APFU data.

## Appendix C: Figure 8



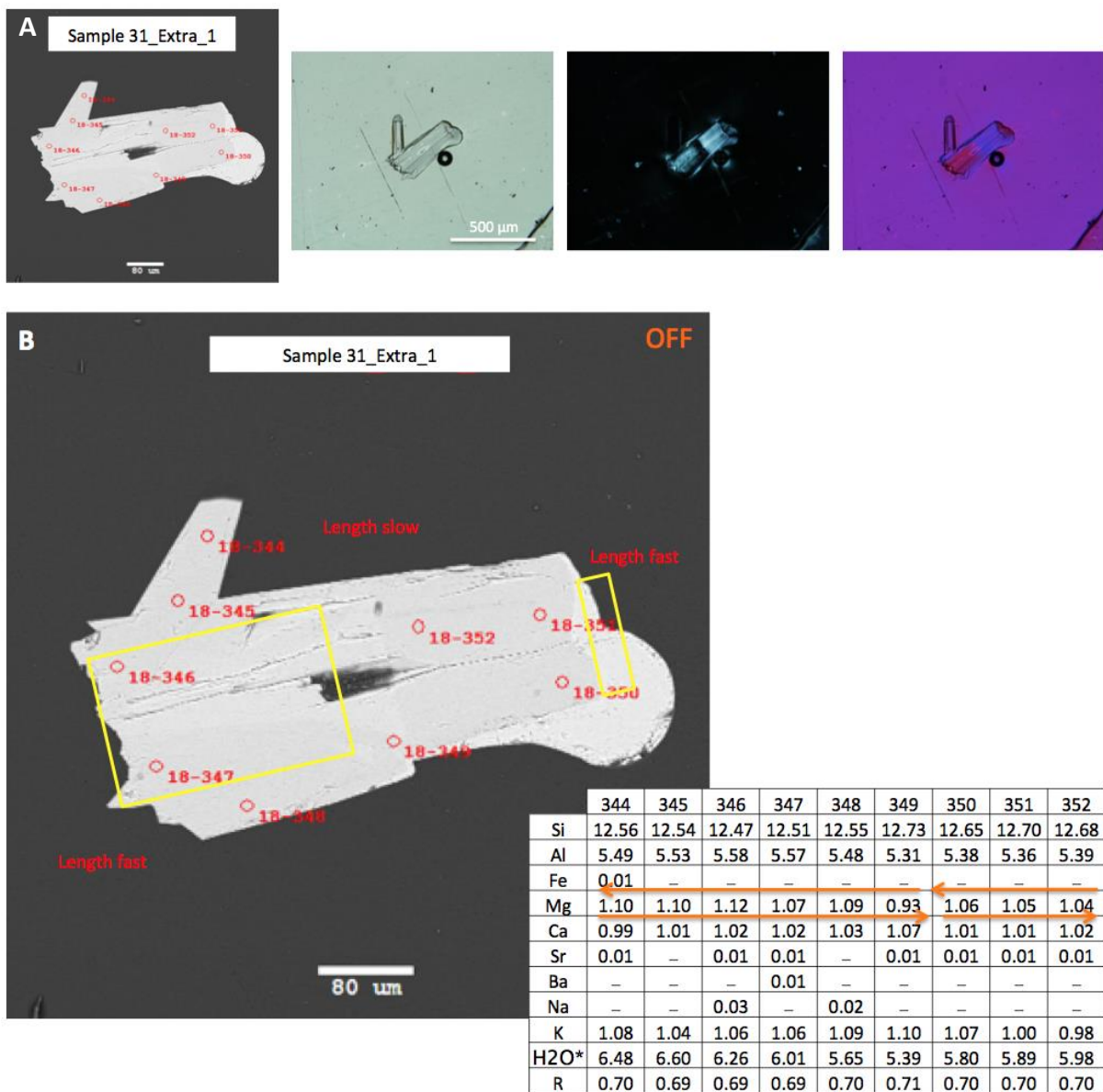
(A) BSE and PLM images of sample 3 of offretite from Mt. Simiouse, Loire, France  
 (B) BSE image along with associated APFU data.

Appendix: Figure 9



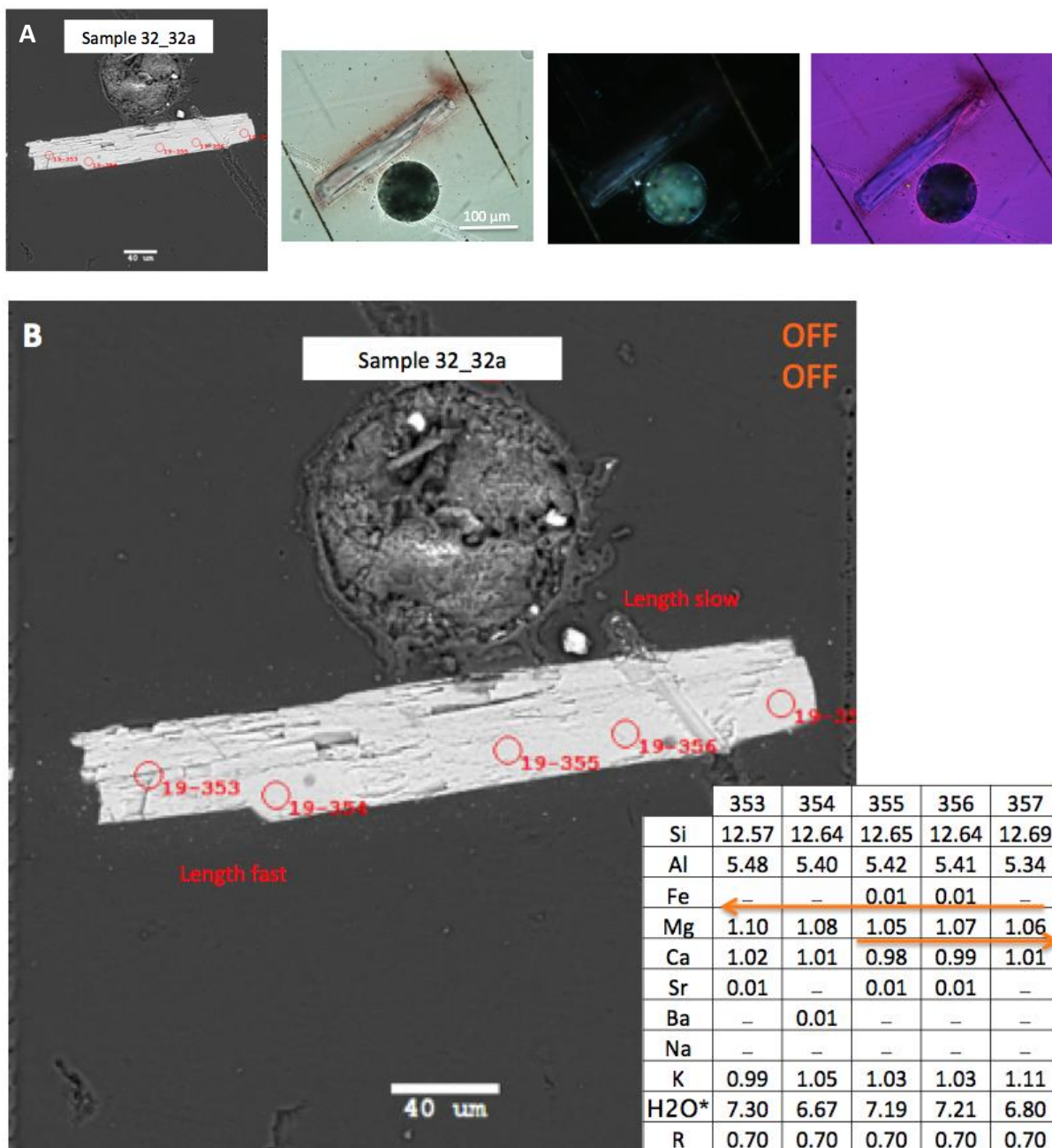
(A) BSE and PLM images of sample 3 of offretite from Mt. Simouse, Loire, France  
 (B) BSE image along with associated APFU data.

Appendix C: Figure 10



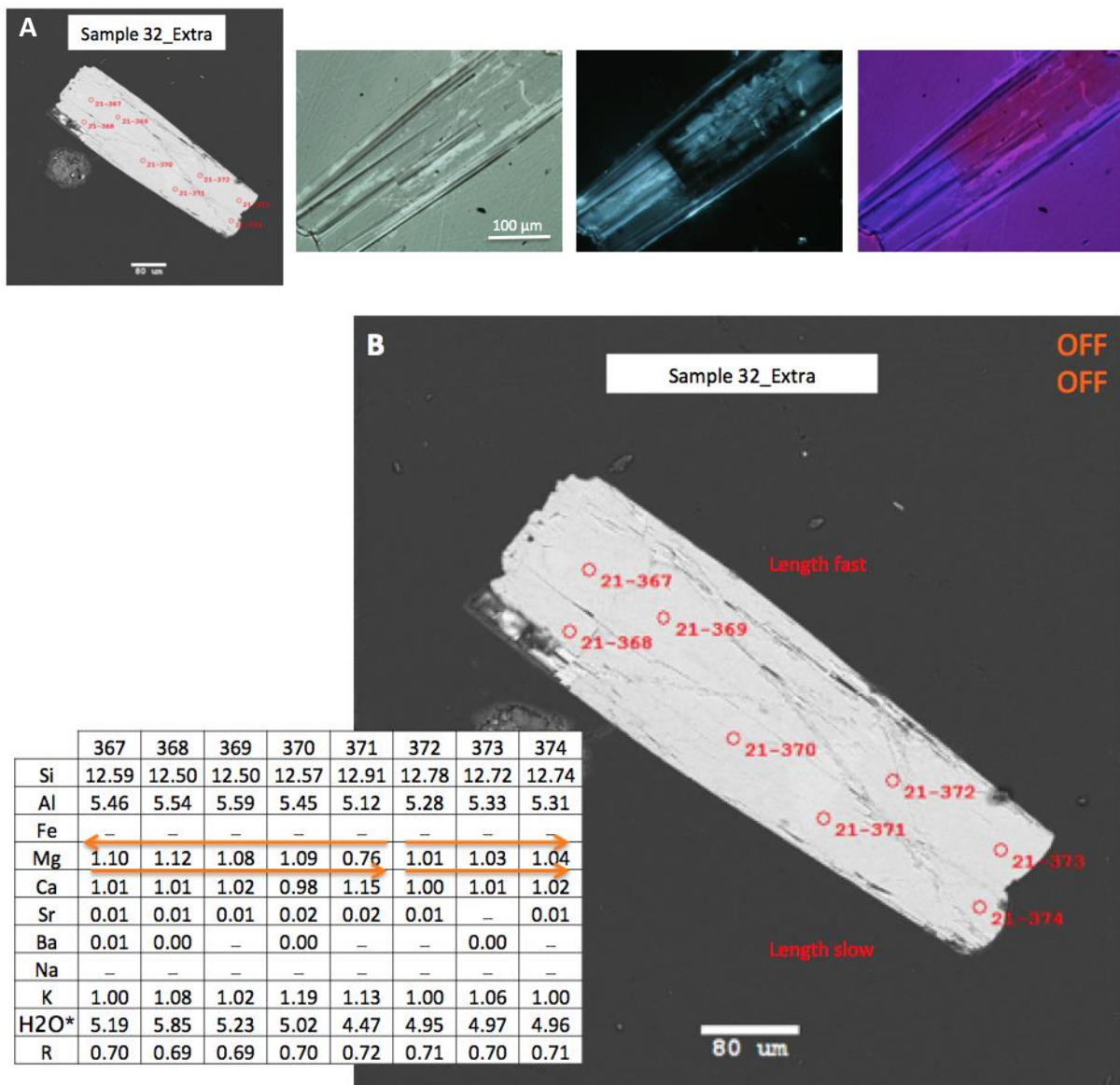
(A) BSE and PLM images of sample 3 of offretite from Mt. Simiouse, Loire, France  
 (B) BSE image along with associated APFU data.

## Appendix C: Figure 11



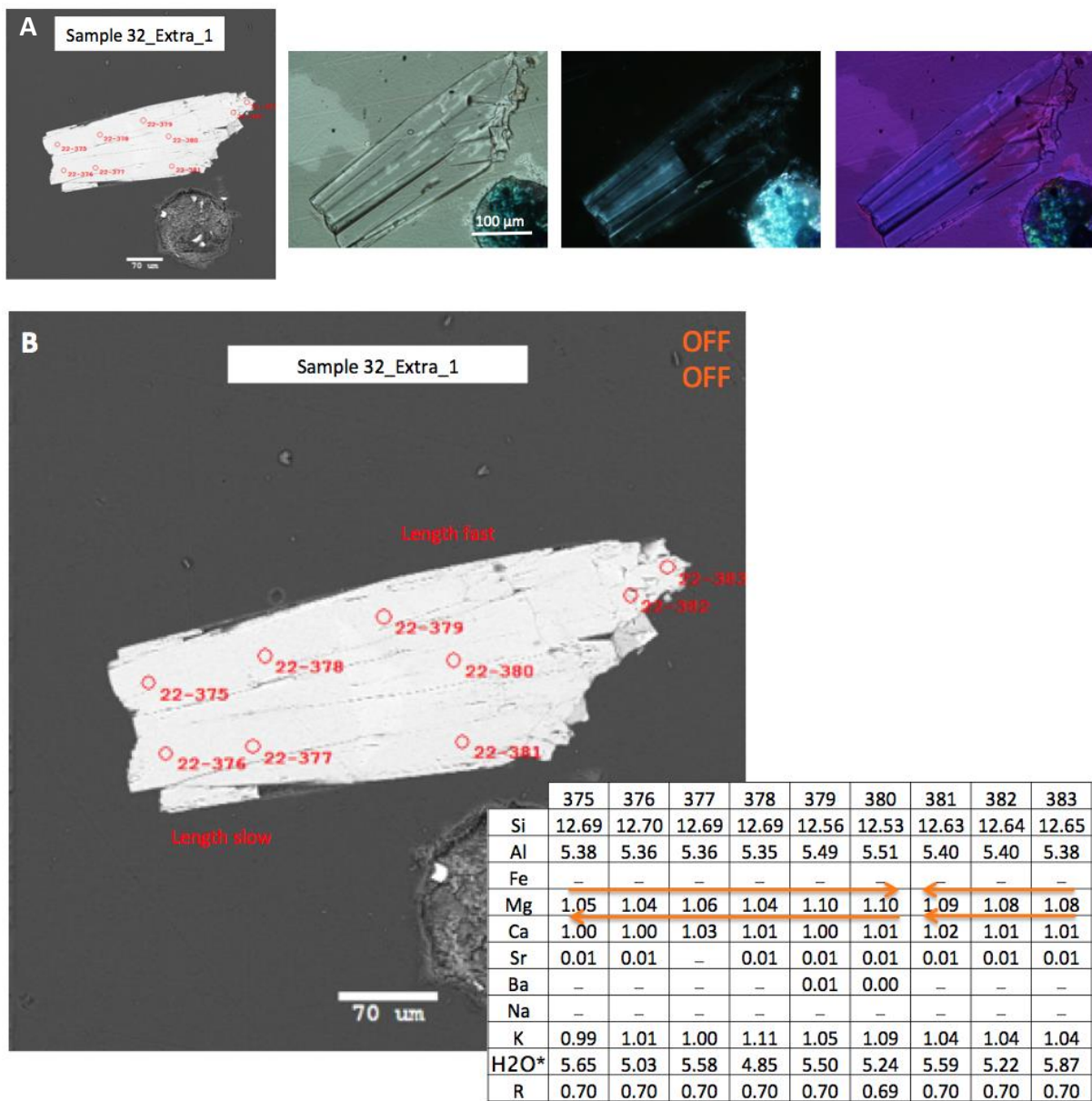
(A) BSE and PLM images of sample 3 of offretite from Mt. Simouse, Semiol, Chatelneuf, Loire, Rhone Alpes, France (B) BSE image along with associated APFU data.

## Appendix C: Figure 12



(A) BSE and PLM images of sample 3 of offretite from Mt. Simiouse, Semiol, Chatelneuf, Loire, Rhone Alpes, France (B) BSE image along with associated APFU data.

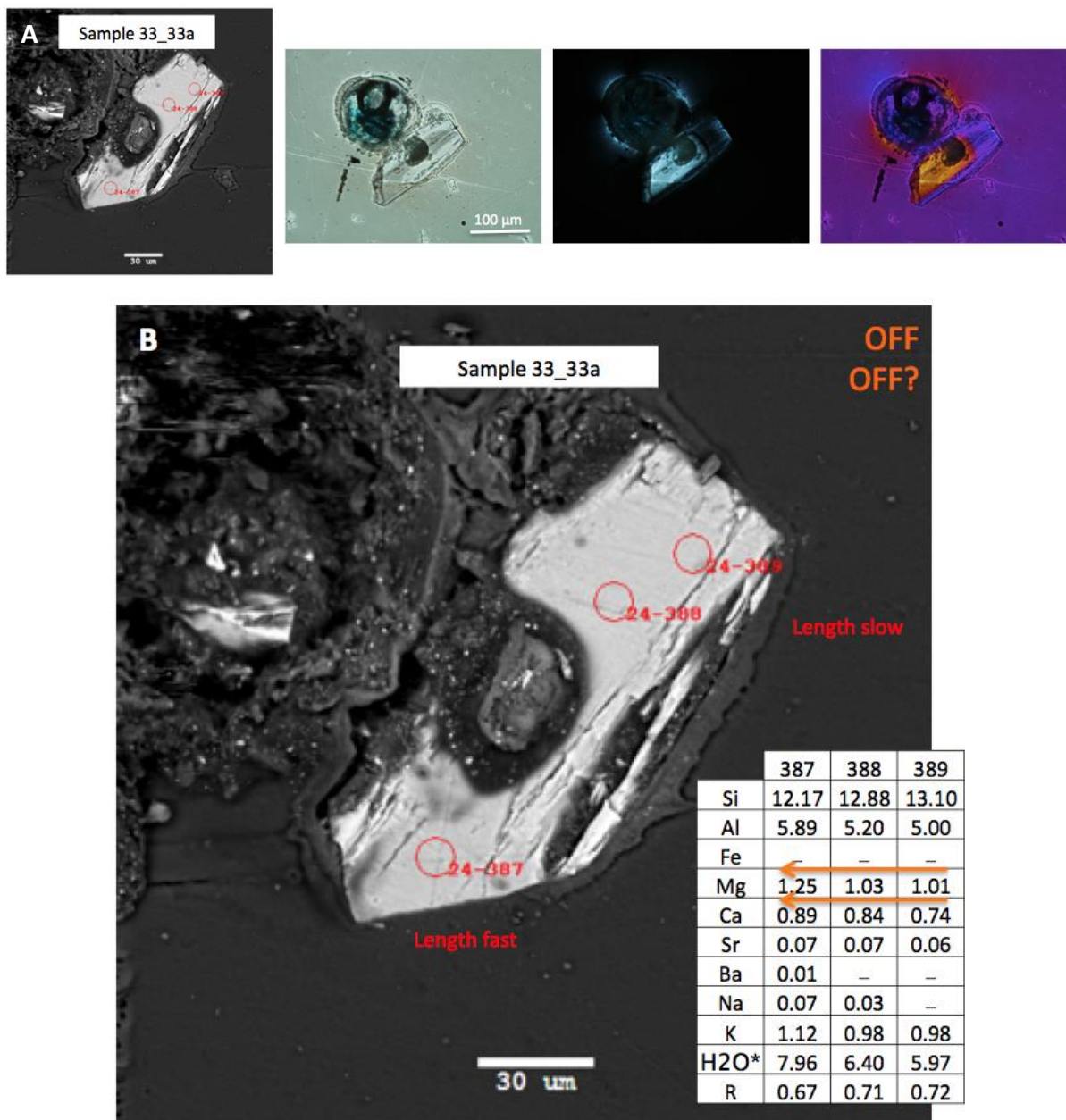
## Appendix C: Figure 13



(A) BSE and PLM images of sample 3 of offretite from Mt. Simiouse, Semiol, Chatelneuf, Loire, Rhone Alpes, France (B) BSE image along with associated APFU data.

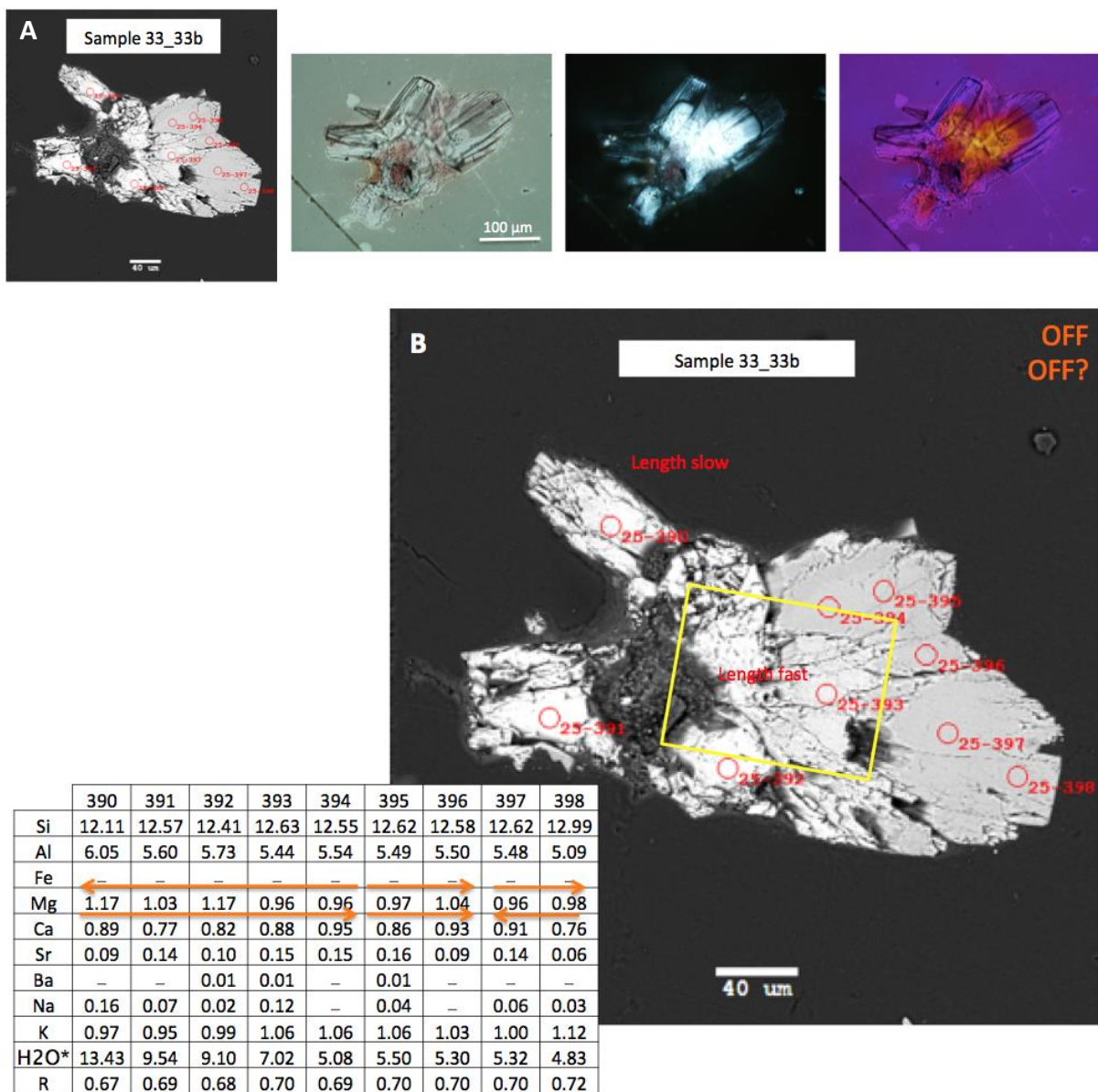


## Appendix C: Figure 14



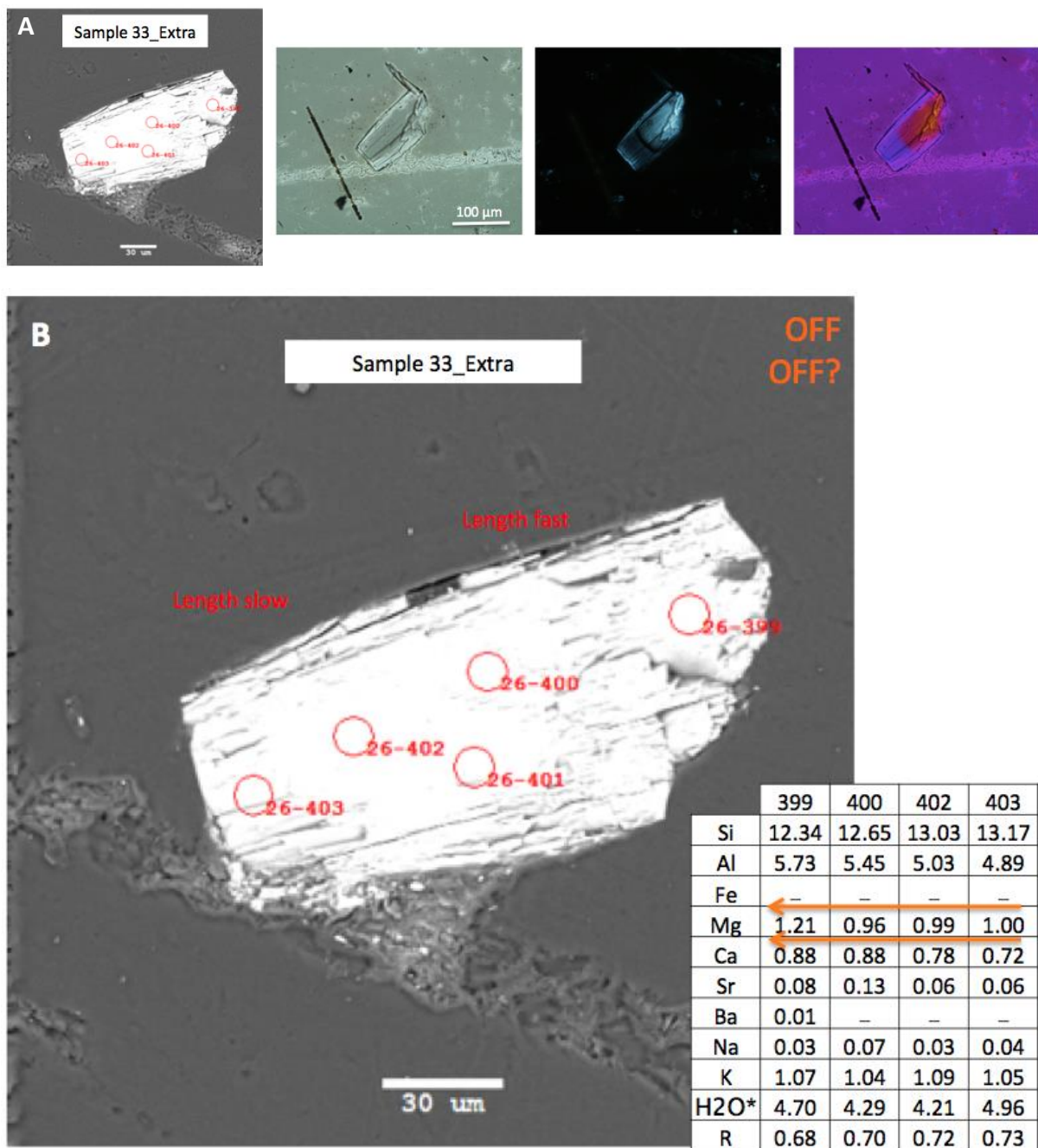
(A) BSE and PLM images of sample 3 of offretite from Sasbach, Kaiserstuhl, Germany (B) BSE image along with associated APFU data.

Appendix C: Figure 15



(A) BSE and PLM images of sample 3 of offretite from Sasbach, Kaiserstuhl, Germany (B) BSE image along with associated APFU data.

## Appendix C: Figure 16



(A) BSE and PLM images of sample 3 of offretite from Sasbach, Kaiserstuhl, Germany (B) BSE image along with associated APFU data.

## Appendix D

Re: Kristina Pourtabib The Microscope 63(4) question



Dean Golemis &lt;dgolemis@mcri.org&gt;

Wed 3/1, 10:35 AM

Pourtabib, Kristina (pour1824@vandals.uidaho.edu); Gunter, Mickey (mgunter@uidaho.edu) ✉



Reply all | ▾

Inbox

Hi Kristina,

Thanks for reaching out to to us. Permission is granted for use of the Zeolite Erionite article in your final dissertation, as requested.

Good luck with your dissertation!

Best wishes,

dean.

**Dean Golemis**

Managing Editor, Microscope Publications

McCrone Research Institute [www.mcri.org](http://www.mcri.org)

2820 S. Michigan Avenue, Chicago IL 60616-3230

Tel. (312) 842-7100 Fax (312) 842-1078

[dgolemis@mcri.org](mailto:dgolemis@mcri.org)**Subscribe to *The Microscope* journal -- new low price for first-time individual subscribers, \$38.50! >>[www.mcri.org](http://www.mcri.org)**